Simulation of foam in Enhanced Oil Recovery (EOR) and Carbon Capture and Storage (CCS) applications

Lyu, X.

DOI
10.4233/uuid:127b6a6f-c947-4624-a72c-11f6539c41d7

Publication date
2021

Document Version
Final published version

Citation (APA)
Lyu, X. (2021). *Simulation of foam in Enhanced Oil Recovery (EOR) and Carbon Capture and Storage (CCS) applications.* [Dissertation (TU Delft), Delft University of Technology].
https://doi.org/10.4233/uuid:127b6a6f-c947-4624-a72c-11f6539c41d7

Important note
To cite this publication, please use the final published version (if applicable).
Please check the document version above.

TU Delft

ISBN 978-946384261-7

Simulation of Foam in Enhanced Oil Recovery (EOR) and Carbon Capture and Storage (CCS) Applications

Xiaocong Lyu

Simulation of Foam in Enhanced Oil Recovery (EOR) and Carbon Capture and Storage (CCS) Applications

Xiaocong Lyu

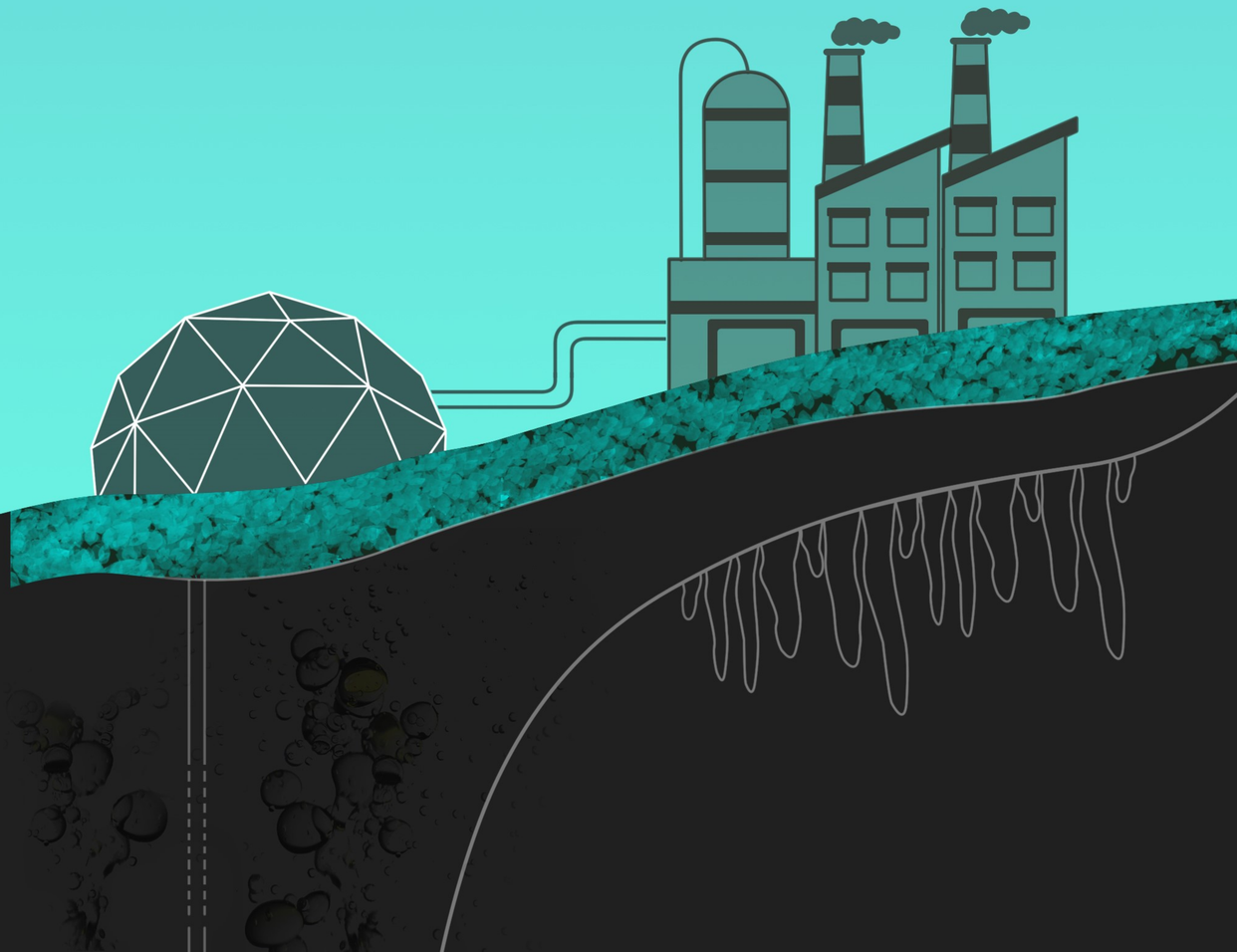

Propositions

accompanying the dissertation

SIMULATION OF FOAM IN ENHANCED OIL RECOVERY (EOR) AND CARBON CAPTURE AND STORAGE (CCS) APPLICATIONS

by

Xiaocong LYU

1. Nonlinear behavior in nature could be represented by linear approximation at an acceptable accuracy (Chapter 3).
2. Modeling is a key tool in understanding the complicated nature of foam-oil interaction hidden in porous media, especially when modeling meets experiments (Chapter 4).
3. Fractional-flow theory is one powerful tool to explain the special features occurring in numerical simulation; however, fractional-flow theory leaves out some key aspects of the displacements in reality (Chapter 4 and 5).
4. The benefits of foam injection to increase the trapping of CO_2 in porous media still remain an open question (Chapter 6).
5. "All models are wrong, but some are useful".- *George Box*
6. A PhD journey is like a foam generation process that requires some conditions for a qualitative change.
7. The chance to supervise students is a big opportunity for a PhD candidate, but it comes at a major cost of time.
8. Collaboration between industry and academia provides impetus to move a new theory forward continuously.
9. Making music is not simply translating notes and rests into tones and pauses with specific durations. Similarly, developing a new simulator is more than implementing functional requirements.
10. Stubbornness is not always a negative trait. It can also be a positive quality in a PhD candidate.

These propositions are regarded as opposable and defendable, and have been approved as such by promotors Dr. D.V. Voskov and Prof. dr. W.R. Rossen.

Stellingen

behorende bij het proefschrift

SIMULATION OF FOAM IN ENHANCED OIL RECOVERY (EOR) AND CARBON CAPTURE AND STORAGE (CCS) APPLICATIONS

door

Xiaocong LYU

1. Niet-lineair gedrag in de natuur kan worden weergegeven door een lineaire benadering met een acceptabele nauwkeurigheid (Hoofdstuk 3).
2. Modellering is een belangrijk hulpmiddel bij het begrijpen van de gecompliceerde aard van schuim-olie-interactie verborgen in poreuze media, vooral wanneer modelleren en experimenten samenkomen (Hoofdstuk 4).
3. Fractional-flow theorie is een krachtig hulpmiddel om de speciale kenmerken die optreden in numerieke simulatie te verklaren; de Fractional-flow theorie laat echter enkele belangrijke aspecten van de verplaatsingen in de werkelijkheid buiten beschouwing (hoofdstuk 4 en 5).
4. De voordelen van schuiminjectie om de opsluiting van CO_2 in poreuze media te vergroten blijft een open vraag (hoofdstuk 6).
5. "Alle modellen zijn fout, maar sommige zijn nuttig".- *George Box*
6. De zoektoch van de doctoraat is als een proces van schuimvorming dat een aantal voorwaarden vereist voor een kwalitatieve verandering.
7. De kans om studenten te begeleiden is een grote kans voor een promovendus, maar het kost veel tijd.
8. Samenwerking tussen de industrie en de academische wereld geeft een impuls om een nieuwe theorie continu vooruit te helpen.
9. Muziek maken is niet alleen het vertalen van noten en rusten in tonen en pauzes met een bepaalde duur. Op een gelijke manier is het ontwikkelen van een nieuwe simulator meer dan het implementeren van functionele eisen.
10. Koppigheid is niet altijd een negatieve eigenschap. Het kan ook een positieve kwaliteit zijn in een promovendus.

Deze stellingen worden opponeerbaar en verdedigbaar geacht en zijn als zodanig goedgekeurd door promotoren Dr. D.V. Voskov and Prof. dr. W.R. Rossen.

Simulation of Foam in Enhanced Oil Recovery (EOR) and Carbon Capture and Storage (CCS) Applications

SIMULATION OF FOAM IN ENHANCED OIL RECOVERY (EOR) AND CARBON CAPTURE AND STORAGE (CCS) APPLICATIONS

Proefschrift

ter verkrijging van de graad van doctor
aan de Technische Universiteit Delft,
op gezag van de Rector Magnificus prof. dr. ir. T.H.J.J. van der Hagen,
voorzitter van het College voor Promoties,
in het openbaar te verdedigen op
dinsdag 2 november 2021 om 15:00 o'clock

door

Xiaocong LYU

Master of Engineering in Oil and Gas Field Development Engineering,
China University of Petroleum, Beijing, China,
geboren te Shandong, China.

Dit proefschrift is goedgekeurd door de

promotor: Dr. D.V. Voskov
copromotor: Prof. dr. W.R. Rossen

Samenstelling promotiecommissie:

Rector Magnificus,	voorzitter
Dr. D.V. Voskov,	Technische Universiteit Delft
Prof. dr. W.R. Rossen,	Technische Universiteit Delft
Onafhankelijke leden:	
Prof. dr. ir. P.L.J. Zitha	Technische Universiteit Delft
Prof. dr. D.F. Bruhn	Technische Universiteit Delft
Dr. R. Farajzadeh,	Technische Universiteit Delft
Dr. S.E. Gasda,	Norwegian Research Centre (NORCE), Norway
Dr. Y. Méheust,	Université de Rennes 1, France

Keywords: foam, enhanced oil recovery, gravity segregation, carbon capture and storage, enhanced dissolution rate, numerical simulation

Printed by: GildePrint

Front & Back: Xiaocong Lyu, Xiaoying Lyu

ISBN 978-94-6384-261-7

An electronic version of this dissertation is available at
http://repository.tudelft.nl/.

Science is a wonderful thing
if one does not have to earn one's living at it.

Albert Einstein

CONTENTS

SUMMARY

Foam is an agglomeration of gas bubbles separated from each other by thin liquid films. Foam injection has been proved to be an efficient way to increase sweep efficiency in gas-injection enhanced-oil-recovery (EOR) processes or enlarge the storage space for trapping of CO_2 in aquifers. Numerical simulation, an important tool developed by combining physics, mathematics, and computer programming, provides an efficient way to understand the complex fluid flow in subsurface reservoirs with applications to the evaluation of hydrocarbon recovery, energy efficiency, performance analysis, and various optimization problems. However, simulation of foam-related displacement in reservoirs is still an expensive process for conventional simulation due to the strongly nonlinear physics. In this dissertation, a newly developed numerical simulator, called Delft Advanced Research Terra Simulator (DARTS), is introduced to investigate the complicated flow behavior in porous media with the presence of foam.

In Chapter 2, our numerical framework is introduced in details. A new approach for the molar formulation, called operator-based linearization (OBL), is implemented to simplify the construction of the Jacobian matrix and residuals. The OBL approach transforms the discretized nonlinear conservation equations into a quasi-linear form via grouping all variables defined by the physical state into state-dependent operators, which improves the simulation efficiency of the highly nonlinear physical problems. Following the idea of the OBL approach, the operator forms of the mass conservation equations, considering the presence of gravity and capillarity, are presented. An implicit-texture (IT) model with two flow regimes is used to describe the foam behavior. A consistent thermodynamic model based on a combination of the Peng-Robinson equation of state (PR EOS) for gas components with an activity model for the aqueous phase is deployed to describe the complex phase-behavior of the CO_2-brine system.

With the presence of capillary and gravity forces, the nonlinearity of the governing equations is amplified even farther, which usually leads to a higher numerical cost. In Chapter 3, the OBL approach is extended for multiphase multi-component systems with capillarity. Through the comparisons with a legacy commercial simulator using a set of benchmark tests, we demonstrate that the extended OBL scheme significantly improves the computational efficiency with the controlled accuracy of approximation and converges to the results of the conventional continuous approach with an increased resolution of parametrization. In all simulation tests, OBL resolution plays an important role in the accuracy of the OBL approach. With increasing degrees of freedom in the simulation problem, DARTS shows its advantages to speed up the modeling process.

Foam injection is a promising enhanced oil recovery (EOR) technology through significantly improving the sweep efficiency of gas injection. Simulation of foam-oil displacement in reservoirs is an expensive process for conventional simulation due to the strongly nonlinear physics. In Chapter 4, the Operator-Based Linearization (OBL) approach, combined with the representation of foam by an implicit-texture (IT) model

with two flow regimes, is extended for simulation of foam EOR process. The numerical-simulation results are validated by using three-phase fractional-flow theory for foam-oil flow. Starting with an initial guess based on the fitting of steady-state experimental data with oil, the OBL foam model is regressed to experimental observations using a gradient-optimization technique. The numerical model shows good agreement with analytical solutions at different conditions and with different foam parameters. The foam-quality scan is accurately fitted to steady-state experimental data, except in the low-quality regime. 1D and 3D simulation results clearly demonstrate two stages of foam propagation from inlet to outlet as seen in the CT coreflood experiments. The failure to fit a few important features in the experiments suggests that it may be important to explore a new model to accurately represent the dynamic behavior of foam in porous media.

In Chapter 5, the effect of heterogeneity on gravity segregation is investigated by using an implicit-texture (IT) foam model with two flow regimes. The numerical accuracy of the simulations, including water-gas co-injection and pre-generated foam injection, with the OBL approach is validated by comparing segregation length to analytical solutions. The numerical results show good agreement with analytical solutions in horizontal homogeneous reservoirs. Through fractional-flow theory, we find that the transition zone during water-gas co-injection is caused by numerical dispersion. The transition zone beneath the override zone with foam injection is not a numerical artefact, but caused by the low gas relative-mobility during the transient displacement process. Reservoir heterogeneity plays an important role in gravity segregation. In two-layer models, the thickness of the top layer plays an important role in the ultimate segregation length. A thin top layer does not affect segregation in the bottom layer, while a thicker top layer dominates the segregation length, with less influence of the bottom layer.

Finally, Chapter 6 shows a realistic phase-behavior model for simulation of CO_2 sequestration in aquifers. The CO_2 sequestration physics is complemented with a foam model which provides us with the ability to investigate the effect of foam co-injection on CO_2 trapping. The dissolution rate caused by the gravitational instabilities is enhanced further in the presence of a capillary transition zone (CTZ). Foam injection can mitigate gravity override during gas injection by reducing gas mobility. This process increases the amount of residual trapped CO_2. In addition, the presence of foam reduces the amount of flowing gas, thus reducing the risk of leakage. In the long (post-injection) time scale, the presence of foam is not affecting the trapping significantly. Increased residual trapping reduces the spread of CO_2 that in turn reduces the dissolution trapping. More complex physical models are required for an accurate evaluation of these mechanisms in realistic subsurface scenarios.

SAMENVATTING

Schuim is een agglomeratie van gasbellen, van elkaar gescheiden door een dunne vloeistoffilm. Schuim injectie is een bewezen efficiënte manier om de veeg efficiëntie van gasinjectie Verbeterde Olie Terugwinning (EOR) processen te verbeteren, of om de beschikbare ruimte voor het insluiten van CO_2 te vergroten. Numerieke simulatie, een belangrijke techniek ontwikkeld door middel van het combineren van natuurkunde, wiskunde met programmeertechnieken, biedt een efficiënte manier om complex stromingsgedrag in ondergrondse reservoirs te bestuderen. Mogelijke toepassingen van liggen in de evaluatie van koolwaterstof winning, energie-efficiëntie, prestatie analyse en uiteenlopende optimalisatieproblemen. De simulatie van schuimgerelateerde verdrijvingsprocessen in reservoirs is uitdagend voor conventionele simulatietechnieken vanwege de intensieve berekeningen die nodig zijn voor het oplossen van de sterk niet-lineaire natuurkunde. In deze dissertatie wordt een nieuw ontwikkelde simulator genaamd Darts Advanced Research Terra simulator (DARTS) gebruikt om het complexe stromingsgedrag van schuim in poreuze media te bestuderen.

In hoofdstuk 2 wordt het het numerieke kader in detail uitgewerkt. Een nieuwe benadering voor de molaire formulatie genaamd Operator-Based Linearization (OBL) is geïmplementeerd om de constructie van de Jacobian matrix en de residuals te versimpelen. De OBL benadering transformeert de gediscretizeerde niet-lineaire behoudswetten naar een quasi-lineaire vorm door middel van het groeperen van variabelen omschreven door de fysieke staat naar staat-afhankelijke operators, wat leidt tot een verbetering van de simulatie efficiëntie van het oplossen van de sterk nonlineaire vergelijkingen. The operator vorm van de wet van behoud van massa, in acht nemend het effect van zwaartekracht en capillariteit, wordt gepresenteerd. Een Impliciet-Textuur (IT) model met twee stromingsregimes wordt gebruikt om schuimgedrag te beschrijven. Een consistent thermodynamisch model gebaseerd op een combinatie van de Peng-Robinson Equation of State (PR EOS) voor gascomponenten met een activiteit model voor de waterfase is ingezet om het complexe fasegedrag van het CO_2-pekel systeem te beschrijven.

Door de aanwezigheid van capillaire druk en zwaartekrachtseffecten wordt de nonlineairiteit van het systeem verder vergroot, met een doorgaans hogere rekeneis tot gevolg. In hoofdstuk 3, de OBL methode is verder uitgebreid voor multi-fase, multi-componenten systemen met capillariteit. Door middel van ijken met een oudere commerciële simulator met een aantal tests wordt gedemonstreerd dat de uitgebreide OBL notatie de computationele efficientie met de gecontroleerde nauwkeurigheid van benadering sterk verbeterd, en tevens convergeert naar de resultaten van de conventionele continue methode met een verhoogde parametrizatieresolutie. In alle geteste simulaties is de OBL resolutie van belang voor de nauwkeurigheid van de resultaten van de methode. Met een toenemende mate van graad van vrijheid in de simulatieproblematiek komt DARTS tot zijn recht met het versnellen van het simulatieproces.

Schuiminjectie is een veelbelovende EOR technologie die de potentie heeft de veeg

efficiëntie van gasinjectie significant te verbeteren. Simulatie van schuim-olie verdrijving in reservoirs is een computationeel zwaar probleem voor conventionele simulatie door de sterk nonlineaire natuurkunde. In hoofdstuk 4 wordt de OBL methode uitgebreid voor de simulatie van schuim-EOR processen en gecombineerd met de IT schuimrepresentatie met twee stromingsregimes. De numerieke resultaten zijn gevalideerd met de drie-fase fractional-flow theorie voor schuim-olie stroming. Beginnend met een eerste schatting gebaseerd op een fit met steady-state experimentele data met olie wordt het OBL-schuim model geregresseerd naar experimentele observaties door middel van een gradient-optimisatie techniek. Het numerieke model toont goede overeenstemming met de analytische oplossing onder verschillende omstandigheden en met verschillende schuimparameters. De schuim-kwaliteitsscan is accuraat gepast aan de stabiele toestand experimentele data, met uitzondering van het lage kwaliteitsregime. 1D en 3D simulatieresultaten tonen duidelijk twee stages van schuimpropagatie van ingang tot uitgang zoals in de CT kernstroming experimenten. Het onvermogen enkele belangrijke kenmerken te passen aan de experimenten suggereert dat het belangrijk is verder onderzoek te doen naar een nieuw model om het dynamische gedrag van schuim in poreuze media te beschrijven.

In hoofdstuk 5 wordt het effect van heterogeniteit op zwaartekrachtscheiding onderzocht met het gebruik van een IT schuimmodel met twee stromingsregimes. De numerieke accuraatheid van de OBL simulaties, waaronder water-gas co-injectie en pregegenereerde schuiminjectie, wordt gevalideerd door segregatielengte te vergelijken met de analytische oplossing. De numerieke resultaten tonen goede overeenstemming met de analytische oplossing in horizontale homogene reservoirs. Met het gebruik van die fractional-flow theorie wordt aangetoond dat de transitiezone tijdens water-gas co-injectie wordt veroorzaakt door numerieke dispersie. De transitiezone onder de overschrijvende zone met schuiminjectie is geen numeriek artefact, maar wordt veroorzaakt door de lage relatieve mobiliteit van gas tijdens de transiente verdrijving. Reservoir heterogeniteit speelt een belangrijke rol in zwaartekrachtsscheiding. In twee-lagen modellen speelt de dikte van de bovenste laag een belangrijke rol in de uiteindelijke segregatielengte. Een dunne bovenlaag heeft geen effect op de segregatie in de onderste laag, terwijl een dikke bovenlaag de segregatielengte domineert met minder invloed op de onderlaag.

Tot slot laat hoofdstuk 6 een realistisch fase-gedragsmodel voor de simulatie van CO_2 sequestratie in watervoerende lagen zien. De CO_2 sequestratie natuurkunde wordt gecomplementeerd met een schuimmodel, wat het mogelijk maakt het effect van schuim co-injectie op CO_2 insluiting te onderzoeken. De snelheid van oplossing veroorzaakt door gravitationele instabiliteit word verder vergroot door de aanwezigheid van een capillaire transitiezone (CTZ). Schuiminjectie kan zwaartekracht bovenstroom tijdens gas injectie voorkomen door de mobiliteit van het gas te verminderen. Dit proces vergroot de hoeveelheid residueel opgesloten CO_2. Daarnaast vermindert de aanwezigheid van schuim de hoeveelheid stromend gas en dus de kans op lekken. Op lange tijdschaal (na-injectie) heeft de aanwezigheid van schuim geen significant effect op het insluiten van CO_2. Vergrootte hoeveelheid residueel opgesloten CO_2 verminderd de verspreiding van CO_2 met een verminderde opsluiting door oplossing tot gevolg. Complexe fysieke modellen zijn nodig om deze mechanismen in realistische ondergrondscenario's accuraat te kunnen evalueren.

PREFACE

Dear reader,

This dissertation is the product of the research work conducted in Delft Advanced Research Terra Simulator (DARTS) group in the Delft University of Technology between October 2017 and October 2021, under the supervision of my promotors, Dr. Denis Voskov and prof. William R. Rossen. I studied in the Reservoir Engineering section, part of the Department of Geoscience & Engineering within the Faculty of Civil Engineering & Geosciences. The objective of this research was designed to develop an efficient and accurate simulator to capture the highly nonlinear flow behavior with the presence of foam in porous media. The Operator-based linearization (OBL) approach is applied to provide an approximate representation of the exact physics with controlled error. The scientific motivations of this research are carefully highlighted in Chapter 1.

In this book, most of the chapters were already published in journal articles or in conference papers through these years. In Chapter 2 where I described the methodology of this research, I was endeavoring to avoid the slightly inconsistent notations and repetitions; however, these small mistakes may still be present. I hope that all readers can enjoy reading this book.

My doctoral study is a long story filled with unforgettable experiences. When I sat in my office in October 2017, I was so proud of having two best supervisors in the world, **Bill**, one famous expert in foam physics, and **Denis**, who made a great achievement in simulations. Meanwhile, I was also stressed because I do not want to disappoint them due to my poor background. Luckily, they always encouraged and guided me to tackle the difficulties in my research, even though I made some mistakes. After one year, I started to develop our simulator DARTS and carried out my research step by step.

Foam is one of the complicated systems in petroleum engineering, but also quite interesting. Foam injection, as one important enhanced-oil-recovery (EOR) technique, has been investigated for many years. However, we still do not figure out all the physics in foam EOR processes, such as the interactions between foam and oil and the effect of heterogeneity. This research covers these topics and illustrates the underlying mechanisms clearly. After discussing with my supervisors, we do think that foam can be implemented in carbon dioxide (CO_2) sequestration considering the foam's ability to mitigate gravity segregation. We investigated this topic based on some assumptions and it deserves further study in the future.

The mode of PhD study is a learning curve that is very flat in the beginning and at one point where abrupt changes occur. In the first two years, the main activities were reading papers, presenting in conferences, and writing code. Afterwards, I grew up quickly and made contributions to the development of DARTS. In addition, I started to supervise students during their thesis projects and prepare practical sessions for master courses. It was a tough process, but these experiences are a big fortune for future research and academic activities.

PhD life is a combination of hard work and recreational activities including basketball games with friends, parties with colleagues, and trips around the world. Such a wonderful journey in Delft! By looking back I really enjoy this challenging but fantastic journey, full of sacred academic achievements and fun activities. Finally, I hope that this work can give you some inspiration in your research.

Xiaocong Lyu
Delft, June 2021

LIST OF FIGURES

LIST OF TABLES

1

INTRODUCTION

Global climate change is one universal issue mainly caused by the emissions of greenhouse gas (GHG). Carbon dioxide (CO_2) emissions are the principal driver of global warming. The burning of fossil fuels, such as coal, oil and gas, for energy and power, is the primary source of GHG emissions. According to *Our World in Data*, the global annual CO_2 emissions in 2019 is over 35 billion tonnes due to the burning of fossil fuels for energy and cement production (Fig. 1.1(a)) [1]. On the other hand, the demand for fossil fuels is still quite high, according to the forecast data from *World Energy Outlook (2018)*, accounting for 74.1% by 2040 (52.6% of oil and natural gas and 21.5% of coal) (Fig. 1.1(b)) [2]. Therefore, the balance between continuously increasing energy demand and the climate impact of fossil fuels is one challenge in the following decades.

To meet the challenge of global climate change, a renewable energy revolution has begun, but it may take long time to abandon fossil fuels, such as oil and gas, completely. In the context of energy transition process, fossil-fuel production is also required to be in a more efficient and environmentally friendly manner [3]. Carbon capture, utilization and storage (CCUS) is one effective and important technology to reduce the GHG emissions. CCUS technologies capture CO_2 from fossil-fuel combustion or industrial facilities, and then transport this CO_2 via ships or pipelines. The captured CO_2 is either used as a resource to generate valuable products or is stored permanently in deep underground geological formations. CO_2 can also be injected into oil reservoirs to improve oil recovery, and in this process, the dissolved or carbonated CO_2 is captured in the porous media. There have been some CO_2 storage projects related to enhanced oil recovery (EOR) around the world since the 1970s (Table 1.1) which the storage capacity is above 0.4 Mt/year according to the data from *International Energy Agency* [2]. These target geological formations, such as depleted oil and gas reservoirs, providing potential storage capacity for large-scale long-term CO_2 sequestration.

CO_2-EOR/CCUS is a long-term process involving many physical phenomena in porous media, such as multiphase flow, interactions between phases, and chemical reactions. In these processes, due to reservoir heterogeneity, gravity override, and viscous instability, gas injection typically suffers from poor sweep efficiency, leading to a lower oil recovery

1

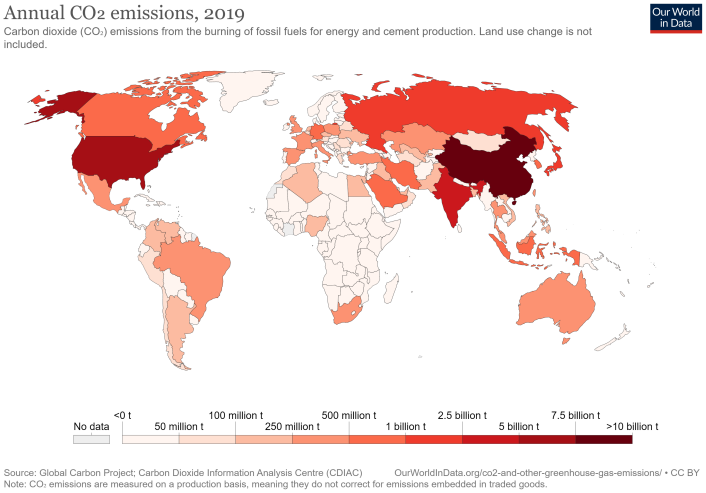

(a)

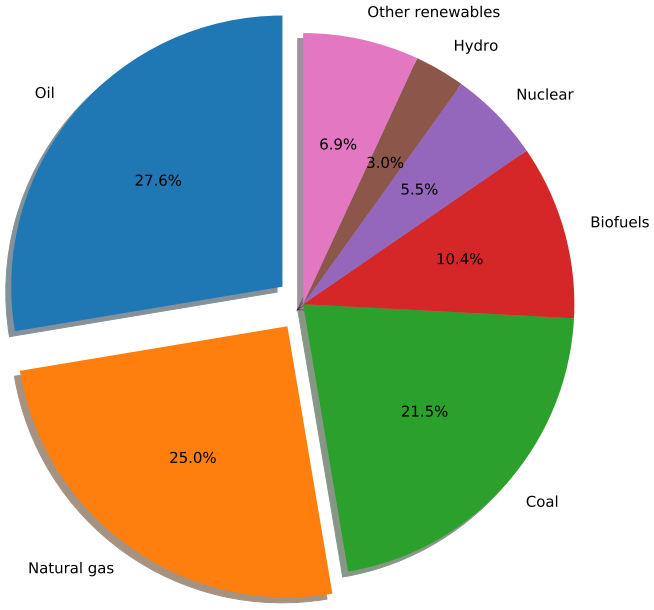

(b)

Figure 1.1: (a) Annual carbon dioxide (CO_2) emissions from burning of fossil fuels for energy and cement production; data from *Our World in Data (2019)*. (b) World primary energy consumption (2040 forecast); data *World Energy Outlook (2018)* by the *International Energy Agency*.

or less storage (Fig. 1.2). Foam, an agglomeration of gas bubbles separated from each

Table 1.1: CCUS projects around the world according to the data from *International Energy Agency* [2]

Country	Project	Operation date	Source of CO_2	CO_2 capture capacity (Mt/year)	Primary storage type
United States (US)	Terrell natural gas plants (formerly Val Verde)	1972	Natural gas processing	0.5	EOR
US	Enid fertiliser	1982	Fertiliser production	0.7	EOR
US	Shute Creek gas processing facility	1986	Natural gas processing	7.0	EOR
Norway	Sleipner CO_2 storage project	1996	Natural gas processing	1.0	Dedicated
US/Canada	Great Plains Synfuels (Weyburn/Midale)	2000	Synthetic natural gas	3.0	EOR
Norway	Snohvit CO_2 storage project	2008	Natural gas processing	0.7	Dedicated
US	Century plant	2010	Natural gas processing	8.4	EOR
US	Air Products steam methane reformer	2013	Hydrogen production	1.0	EOR
US	Lost Cabin Gas Plant	2013	Natural gas processing	0.9	EOR
US	Coffeyville Gasification	2013	Fertiliser production	1.0	EOR
Brazil	Petrobras Santos Basin pre-salt oilfield CCS	2013	Natural gas processing	3.0	EOR
Canada	Boundary Dam CCS	2014	Power generation (coal)	1.0	EOR
Saudi Arabia	Uthmaniyah CO_2-EOR demonstration	2015	Natural gas processing	0.8	EOR
Canada	Quest	2015	Hydrogen production	1.0	Dedicated
United Arab Emirates	Abu Dhabi CCS	2016	Iron and steel production	0.8	EOR
US	Petra Nova	2017	Power generation (coal)	1.4	EOR
US	Illinois Industrial	2017	Ethanol production	1.0	Dedicated
China	Jilin oilfield CO_2-EOR	2018	Natural gas processing	0.6	EOR
Australia	Gorgon Carbon Dioxide Injection	2019	Natural gas processing	3.4-4.0	Dedicated
Canada	Alberta Carbon Trunk Line (ACTL) with Agrium CO_2 stream	2020	Fertiliser production	0.3-0.6	EOR
Canada	ACTL with North West Sturgeon Refinery CO_2 stream	2020	Hydrogen production	1.2-1.4	EOR

*Here only projects where CO_2 capture capacity is higher than 0.4 Mt/year is included in the table.

other by thin liquid films, can overcome these problems and thereby improve the sweep efficiency in gas-injection EOR processes [4–6] or enlarge the capacity for trapping of CO_2 [7–9].

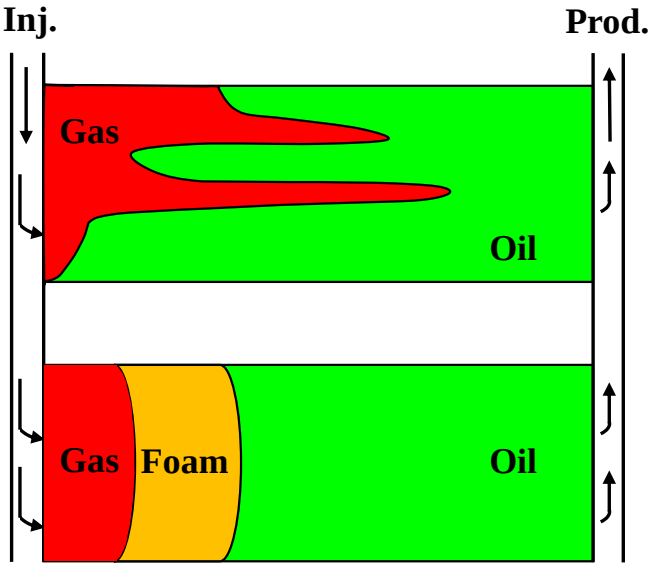

Figure 1.2: Field applications of foam for EOR [10].

Foams in porous media can be generated through various mechanisms [5, 11]. In porous media, lamellae (liquid films separating bubbles) can be generated in three different ways: lamella leave-behind, lamella division or snap-off. When foam is present, gas mobility is significantly reduced [5, 11, 12], leading to a more viscous gas that could give better macroscopic sweep efficiency, and consequently, recovery. The order of mag-

nitude of mobility reduction varies in a large range, depending on foam strength [13, 14]. In some laboratory or simulation studies, it has been proved that foam is stronger and reduces gas mobility more in the high-permeability zones, diverting flow to the low-permeability zone, thereby increasing the final sweep efficiency in heterogeneous reservoirs [15–17].

Numerical simulation, a tool developed by combining physics, mathematics, and computer programming, is an efficient way to understand complex fluid flow in subsurface reservoirs with applications to the evaluation of hydrocarbon recovery, energy efficiency, performance analysis, and various optimization problems [18–20]. It involves solving the partial differential equations (PDEs) governing coupled multiphase flow and transport in porous media with highly nonlinear physics [21, 22].

All coupled equations need to be discretized in space and time to solve the nonlinear system numerically. In reservoir simulation, the finite-volume-method (FVM) discretization scheme has been widely used to discretize the mass-conservation equations in space [21, 23]. Considering the stability of the solution, a fully-implicit (backward-Euler) time discretization is more attractive to avoid restricted simulation time-steps [24, 25]. In this approach, the elliptic flow and highly nonlinear hyperbolic transport problems cannot be decoupled (i.e., need to be solved simultaneously) [26, 27]. This solution strategy introduces nonlinearity into the system of equations, which needs to be resolved by a nonlinear solver.

A Newton-based method is usually applied to linearize the coupled system of nonlinear equations, where an assembly of the Jacobian matrix and the residual vector is required. This is a tough task in general-purpose reservoir simulation because both values and corresponding derivatives of different properties in the governing equations need to be evaluated and assembled at every nonlinear iteration [28]. The complexity of implementation also depends on the types of nonlinear unknowns and strategies which are used to perform nonlinear update [29]. For example, in compositional simulation, the natural formulation performs better for immiscible displacement, whereas the molar formulation shows a better behavior for a miscible gas flooding [30]. Strongly heterogeneous geological properties of the reservoir, such as porosity or permeability, can also increase the computational cost [31].

An Automatic Differentiation Expression Template Library (ADETL) was developed to improve the robustness and flexibility of the linearization process [32]. The Automatic Differentiation General Purpose Research Simulator (ADGPRS), developed based on ADETL, provides a flexible research platform for the implementation of advanced reservoir simulation technologies [e.g. 33, 34]. The nonlinear convergence for simulation problems involved complex physical phenomena such as gravity, capillarity, and chemical reactions still remains a challenging problem. Recently, several advanced nonlinear strategies were developed to successfully address these complex problems [35, 36]. However, most of the advanced nonlinear solvers for general-purpose simulation mentioned above have been developed for natural formulation [37] with explicit correction of saturation. An advanced simulation strategy for the molar formulation is still required to improve the convergence of the nonlinear solutions, especially in the presence of complex physical phenomena.

A new approach for the molar formulation, called operator-based linearization (OBL),

proposed by Voskov [38], follows the ideas originated in Zaydullin *et al.* [39]. This approach presents a new way to linearize the governing equations compared to the conventional linearization approach, that can combine computational performance, flexibility, and robustness. The OBL approach transforms the discretized nonlinear conservation equations into a quasi-linear form via grouping all variables defined by the physical state into state-dependent operators, which improves the simulation efficiency of the highly nonlinear physical problems. These state-dependent operators, relying on current local physical properties (e.g. relative permeability, viscosity, density), are approximated by discrete representation on a uniform or nonuniform mesh in parameter space [40, 41]. A multi-linear interpolation is used to achieve the continuous representation of state-dependent operators, which provides an approximate representation of the exact physics of the physical problem with controlled error. This new approach also provides an opportunity to control the nonlinearity in the physics by changing the resolution of the parameter space [42].

The Delft Advanced Research Terra Simulator (DARTS), which is capable of modeling complex flow and transport related to various energy applications [40, 43, 44], is a new numerical framework developed at TU Delft. The OBL approach is deployed to resolve the highly nonlinear problems caused by those special physical phenomena. The main advantage of this approach is a simplified construction of the Jacobian matrix and residuals, since the complex physics-based calculations (i.e., mainly related to the flux in the governing equations) are translated into generic multi-linear interpolation based on supporting points which are used to store the values of state-dependent operators [42]. Meanwhile, the implementation of fully-implicit simulation code is significantly simplified with the OBL methodology. The discretized PDEs and property evaluations are completely separated from each other. That simplifies the efficient, architecture-oriented implementation of advanced numerical approaches exploiting coarse-grained and fine-grained parallelism on CPU and GPU respectively [45]. It is combined with high flexibility of the simulation code: direct implementation of all properties in Python has minimal impact on simulation performance. To maintain high efficiency for large heterogeneous problems, the linear system is solved using flexible Generalized Minimal Residual Method (GMRES) [46, 47] with the constrained pressure residual (CPR) preconditioner [48]. The Algebraic Multigrid (AMG) method is employed to obtain an approximate solution for the decoupled pressure system in the first preconditioner stage. In the second stage, the classical incomplete Lower-Upper factorization (ILU(0)) preconditioner is applied to the FIM system.

1.1. THESIS OBJECTIVES

DARTS is the powerful tool for general-purpose reservoir simulation due to the implementation of the OBL approach. The capability of DARTS to simulate the complex physical problems related to energy-transition processes is one important aspect to be tested. In addition, the accuracy and efficiency of DARTS to handle these problems are worth investigating. The research objectives addressed in this work are:

- Extend the OBL approach for multiphase multi-component systems in the presence of capillarity within the DARTS framework and test the efficiency against a

legacy simulator.

- Investigate the interaction between foam strength and oil saturation through combining three-phase fractional-flow theory and numerical simulation, and test the capability of the OBL foam model to regress to CT coreflood experimental data.
- Study the effect of heterogeneity on gravity segregation during CO_2 foam injection and analyze the effect of numerical dispersion on gravity segregation-length-prediction.
- Extend the OBL foam model to CO_2 sequestration processes and investigate the effect of foam on the trapping of CO_2 in conditions relevant to typical aqueous aquifers.

1.2. THESIS OUTLINE

This thesis comprises seven chapters based on four journal articles published or submitted, in addition to introductory Chapter 1 and conclusive Chapter 7. Chapter 2 describes the numerical models, including the conservation equations used for general-purpose reservoir simulation and their operator forms within the OBL framework. The physical models, such as foam model and the thermodynamic model, are also introduced in this chapter briefly. These physical effects can be represented by modifying the corresponding operators.

In Chapter 3, the OBL approach is extended for multiphase multi-component systems with capillarity. Through a comparison with a legacy commercial simulator using a set of benchmark tests, we demonstrate that the extended OBL scheme significantly improves the computational efficiency with the controlled accuracy of approximation and converges to the results of the conventional continuous approach with an increased resolution of parametrization. The content in this chapter was published in *SPE Journal* [49].

Following the benchmark tests, we study the capacity of DARTS for simulation of a foam EOR process in Chapter 4, which was published in *SPE Journal* [50]. The numerical-simulation results are validated by using three-phase fractional-flow theory for foam-oil flow. Starting with an initial guess based on the fitting of steady-state experimental data with oil, the OBL foam model is regressed to experimental observations using a gradient-optimization technique. 1D and 3D simulation results clearly demonstrate two stages of foam propagation from inlet to outlet as seen in the CT coreflood experiments.

Then, to assess CO_2 foam transport in enhanced oil recovery (EOR) and for CO_2 storage processes in heterogeneous reservoirs, an accurate prediction of foam behaviour is essential. Chapter 5 presents simulation results on using an implicit-texture (IT) foam model with two flow regimes to investigate the effect of heterogeneity on gravity segregation. The numerical accuracy of the simulation with the OBL approach, including water-gas co-injection and injection of pre-generated foam, is validated by comparing segregation length to analytical solutions. By constructing several hypothetical reservoir models containing two communicating layers with different permeabilities and thickness ratios, we examine foam's effect on gravity segregation in heterogeneous reservoirs. The content in this chapter was presented in the *EAGE-IOR2021* Conference [51].

Chapter 6 presents a consistent thermodynamic model based on a combination of the Peng-Robinson equation of state (PR EOS) for gas components with an activity model for the aqueous phase. This model can accurately describe the complex phase-behavior of the CO_2-brine system. The phase-behavior module is combined with the representation of foam by an implicit-texture (IT) model. This combination can accurately capture the complicated dynamics of miscible CO_2 foam at various stages of the sequestration process. The content in this chapter was published in *International Journal of Greenhouse Gas Control* [9].

Finally, Chapter 7 concludes the work and defines perspectives of further research.

2

METHODOLOGY

Summary

The governing equations used to characterize the compositional system in DARTS are described. Following the idea of the OBL approach, the operator forms of the mass conservation equations are presented. Due to the implementation of a phase-potential-upwinding (PPU) strategy, with the presence of gravity and capillarity, the treatment of gravity and capillarity operators is presented. The nonlinearity of capillary operator is analyzed as well. An implicit-texture (IT) model with two flow regimes is used to describe the foam behavior. A consistent thermodynamic model based on a combination of the Peng-Robinson equation of state (PR EOS) for gas components with an activity model for the aqueous phase is illustrated to describe the complex phase-behavior of the CO_2-brine system.

2.1. INTRODUCTION

The Operator-based Linearization (OBL) framework is implemented in DARTS for general purpose reservoir simulations. This approach presents a new way to linearize the governing equations compared with the conventional linearization approach, further improving the simulation performance of complex physical problems. The OBL approach transforms the discretized nonlinear conservation equations into a quasi-linear form by grouping all variables defined by the physical state into state-dependent operators, which improves the simulation efficiency of the highly nonlinear physical problems. These state-dependent operators, relying on current local physical properties (e.g. relative permeability, viscosity, density), are approximated by discrete representation on a uniform or nonuniform mesh in the parameter space [40, 41, 49]. A multi-linear interpolation is used to achieve the continuous representation of state-dependent operators, which provides an approximate representation of the exact physics of the physical problem with controlled error. This new approach also provides an opportunity to control the nonlinearity in physics by changing the resolution of the parameter space [42]. Through several benchmark studies, the computational performance, flexibility, and robustness of DARTS have been demonstrated [42–44, 49].

In practical applications, the resolution of the parameter space is one key factor that affects the accuracy of the OBL approach. To choose a proper resolution, a sensitivity study is required. A coarser parameterization space, corresponding to a smaller OBL resolution, can provide satisfying results, with higher efficiency compared with some academic or legacy simulators in our tests [42–44]. The proper implementation of the OBL approach can speed up Jacobian assembly by a factor of 14x, and even faster on GPU architecture [45], which saves computational costs significantly. In order to improve the accuracy, a higher OBL resolution can be always applied, considering the efficiency of the new linearization scheme.

To introduce the capability of CO_2-foam-related simulations into DARTS, we first need to modify the conservation equations based on the physical models. Considering the capability and complexity of the population-balance (PB) model, an implicit-texture (IT) model is implemented to modify the gas relative permeability (i.e., changing operators) in the presence of foam. For an accurate description of CO_2 phase behavior in an aquifer, a recently developed thermodynamic model based on a combination of a cubic Equation of State (EOS) with an activity model is implemented [52]. This model combines a classic fugacity formulation for the supercritical gas phase and an activity model combined with Henry's law constants for the aqueous brine. This implementation makes the thermodynamic model more accurate than conventional cubic EOS.

Considering different physical problems, an important task is to express the corresponding operators, then to construct the interpolators, which are responsible for the linear interpolation of operators. The operator values and corresponding derivatives in the parameter space are pre-calculated in the form of tables or evaluated adaptively during the simulation based on physical problems. In this chapter, we briefly introduce our numerical framework and the physical models involved in this research.

2.2. CONSERVATION EQUATIONS

Mass transfer in a porous medium involves a multi-phase multi-component flow system, which requires several equations to represent the flow dynamics. In this section, we present the governing equations related to this research. The detailed temporal and spatial discretization and linearization procedures are described.

2.2.1. GOVERNING EQUATIONS

For the investigated domain with volume Ω, bounded by surface Γ, the mass conservation can be expressed as

$$\frac{d}{dt}\int_{\Omega} M^c d\Omega + \int_{\Gamma} \boldsymbol{F}^c \cdot \boldsymbol{n} d\Gamma = \int_{\Omega} Q^c d\Omega. \tag{2.1}$$

Here, M^c denotes the accumulation term for the c^{th} component ($c = 1, \ldots, n_c$, indexing for the mass components, e.g., water, CO_2); $\boldsymbol{F}_c$ refers to the flux term of the c^{th} component; $\boldsymbol{n}$ refers to the unit normal pointing outward to the domain boundary; Q_c denotes the source/sink term of the c^{th} component.

The mass accumulation term collects each component distribution over n_p fluid phases in a summation form,

$$M^c = \phi \sum_{j=1}^{n_p} x_{cj} \rho_j s_j, \quad c = 1, \ldots, n_c, \tag{2.2}$$

where ϕ is the porosity, s_j is the phase saturation, ρ_j is the phase's molar density [mol/m^3] and x_{cj} is the molar fraction of c component in j phase.

The rock is assumed compressible and represented by the change of porosity through:

$$\phi = \phi_0 \big(1 + c_r (p - p_{\text{ref}})\big), \tag{2.3}$$

where ϕ_0 is the initial porosity, c_r is the rock compressibility [1/bar] at the reference pressure p_{ref} [bars].

The mass flux of each component, including convection and diffusion, is expressed by the summation over n_p fluid phases,

$$\boldsymbol{F}^c = \sum_{j=1}^{n_p} (x_{cj} \rho_j \boldsymbol{u_j} + s_j \rho_j \mathbf{J}_{cj}), \quad c = 1, \ldots, n_c. \tag{2.4}$$

Here the velocity $\boldsymbol{u_j}$ follows the extension of Darcy's law to multiphase flow,

$$\boldsymbol{u_j} = -\frac{k_{rj}}{\mu_j} \mathbf{K} (\boldsymbol{\nabla} p_j - \gamma_j \boldsymbol{\nabla} D), \tag{2.5}$$

where $\mathbf{K}$ is the permeability tensor [mD], k_{rj} is the relative permeability of phase j, μ_j is the viscosity of phase j [mPa$\cdot$s], p_j is the pressure of phase j [bars], $\gamma_j = \rho_j g$ is the specific weight [N/m^3] and D is the depth vector [m]. The term $\mathbf{J}_{cj}$ is the diffusion flux of component c in phase j, which is described by Fick's law as

$$\mathbf{J}_{cj} = -\phi D_{cj} \boldsymbol{\nabla} x_{cj}, \tag{2.6}$$

where D_{cj} is the diffusion coefficient [m^2/day].

The required constraints for saturation and capillary pressure are expressed as,

$$\sum_{j=1}^{n_p} s_j = 1, \tag{2.7}$$

$$p_c = p_n - p_w, \tag{2.8}$$

where p_c is the capillary pressure [bars] and p_n and p_w are pressures of the non-wetting and wetting phases respectively. Capillary pressure is a function of saturation, often expressed as $p_c(s_j)$. The capillary-pressure-saturation relationship, also called the capillary-pressure curve, can be measured in the laboratories. In this research, the hysteresis in the relative-permeability and capillary-pressure curves is neglected, so k_{rj} and p_c depend only on saturation.

The nonlinear equations are discretized with the finite-volume method using the two-point flux approximation on general unstructured mesh in space and with the backward Euler approximation in time. For the i^{th} reservoir block, the governing equation in discretized residual form reads:

$$R_i^c = V_i\Big(M_i^c(\omega_i) - M_i^c(\omega_i^n)\Big) - \Delta t\Big(\sum_l A_l F_l^c(\omega) + V_i Q_i^c(\omega)\Big) = 0, \quad c = 1,\ldots,n_c+1. \tag{2.9}$$

Here V_i is the volume of the i^{th} grid block, ω_i refers to state variables at the current time step, ω_i^n refers to state variables at the previous time step, A_l is the contact area between neighboring grids, and Q_i^k is the source or sink term of the k^{th} component.

2.2.2. OPERATOR FORM OF GOVERNING EQUATIONS

DARTS provides capabilities for forward and inverse simulations. The OBL approach is implemented in DARTS to improve the efficiency of simulations with highly nonlinear problems. This new linearization approach was proposed recently for general-purpose reservoir simulation and intends to significantly improve the simulation performance [38, 53]. A finite-volume method (for spatial discretization) and fully implicit method (for temporal discretization) is employed in DARTS, combining with two-point flux approximation on unstructured grids. In addition, the OBL approach is implemented to discretize the physics in parameter space.

In general-purpose compositional simulations, pressure and component overall molar fraction are taken as the unified state variables in a given control volume. Upstream weighting of the physical state is used to determine the flux-related fluid properties determined at the interface l. The discretized mass conservation equation for component c in operator form for gird (here we omit i) reads:

$$V\phi_0[\alpha_c(\omega)-\alpha_c(\omega_n)] - \Delta t \sum_{l\in L(i)} \sum_{j=1}^{n_p} [\Gamma^l \beta_{cj}^l(\omega^u)\Delta\psi_j^l + \Gamma_d^l \gamma_j^l(\omega)\Delta\chi_{cj}^l] + \Delta t V \delta_c(\omega) = 0, \tag{2.10}$$

where V is the control volume, ω_n is the physical state of block i at the previous timestep, ω is the physical state of block i at the new timestep, ω^u is the physical state of the upstream block, Γ^l and Γ_d^l are the fluid and diffusive transmissibilities and $L(i)$ is a set of interfaces for gridblock i.

Here we have defined the following state-dependent operators,

$$\alpha_c(\omega) = \Big(1 + c_r(p - p_{ref})\Big) \sum_{j=1}^{n_p} x_{cj}\rho_j s_j,\ c = 1,\dots,n_c, \tag{2.11}$$

$$\beta_{cj}(\omega) = x_{cj}\rho_j k_{rj}/\mu_j,\ c = 1,\dots,n_c,\ j = 1,\dots,n_p, \tag{2.12}$$

$$\gamma_j(\omega) = \Big(1 + c_r(p - p_{ref})\Big) s_j,\ j = 1,\dots,n_p, \tag{2.13}$$

$$\delta_c(\omega) = \sum_{j=1}^{n_p} v_{cj} r_j(\omega),\ c = 1,\dots,n_c, \tag{2.14}$$

$$\chi_{cj}(\omega) = \rho_j D_{cj} x_{cj},\ c = 1,\dots,n_c,\ j = 1,\dots,n_p. \tag{2.15}$$

The phase-potential-upwinding (PPU) strategy [42] is applied in DARTS to compute the numerical flux. The potential difference of phase j with gravity and capillarity on the interface l can be written as:

$$\Delta\psi_j^l = p_l - p_j^c(\omega_l) - (p_r - p_j^c(\omega_r)) - \frac{\rho_j(\omega_l) + \rho_j(\omega_r)}{2} g(z_r - z_l), \tag{2.16}$$

where p_j^c is the capillary pressure and and l and r are the indexes of two control volumes adjacent to the interface.

In this research, gravity and capillary-pressure terms are treated as two stand-alone operators that depend only on the physical state. For the gravity operator, we followed the idea proposed in Khait and Voskov [42], where n_p mass-density operators (ρ_j) are introduced for each phase. In addition, n_p capillary-pressure operators are introduced to this system. For an n_p-phase system, only n_p-1 capillary pressures are needed for the calculation of phase pressure. Here, the capillary-pressure operator of the reference phase is defined as zero to keep the whole system coordinated. A straightforward implementation of PPU within the OBL approach implies an increase in the number of flux operators from n_c to $n_c n_p$, because each phase should be treated separately. Hence, the convection-related operators for isothermal problem with n_c components and n_p phases are expressed as:

$$\beta_{cj}(\omega) = \begin{cases} x_{cj,l}\rho_{j,l}k_{rj,l}/\mu_{j,l} & \text{if } \psi_{j,lr} > 0 \\ x_{cj,r}\rho_{j,r}k_{rj,r}/\mu_{j,r} & \text{otherwise} \end{cases}, \tag{2.17}$$

$$\delta_j(\omega) = \rho_j g, \tag{2.18}$$

$$\xi_j(\omega) = p_{c,j}, \tag{2.19}$$

where δ_j and ξ_j are gravity and capillarity operators, respectively, only dependent of the physical state.

2.2.3. INTERPOLATION OF OPERATORS

The combination of different physical properties into a single nonlinear operator allows us to simplify the complicated nonlinear physics and implementation of the generic linearization approach. Instead of performing complex evaluations of properties and their derivatives with respect to nonlinear unknowns during the simulation, we can parameterize operators in the physical space at the pre-processing stage or adaptively with a

limited number of supporting points.[42]. The parameter space depends on the physical problem. For strongly nonlinear functions (e.g., capillary pressure), it is necessary to select a reasonable OBL resolution to characterize the physical space. A coarse OBL resolution may cause a larger deviation in the solutions [38].

The governing equations are written in the form of state-dependent operators by following the OBL approach. The state-dependent operators can be parameterized (Fig. 2.1) with respect to nonlinear unknowns in multi-dimension tables under different resolutions. The values and derivatives of the operators in the parameter space can be interpolated and evaluated based on supporting points (Fig. 2.2). For the adaptive parameterization technique [42], the supporting points are calculated 'on the fly' and stored for later re-usage, which can save time for parameterization in high-dimension parameter space (i.e. in multi-component compositional simulations). At the same time, the Jacobian assembly becomes flexible with the OBL approach, even for very complex physical problems.

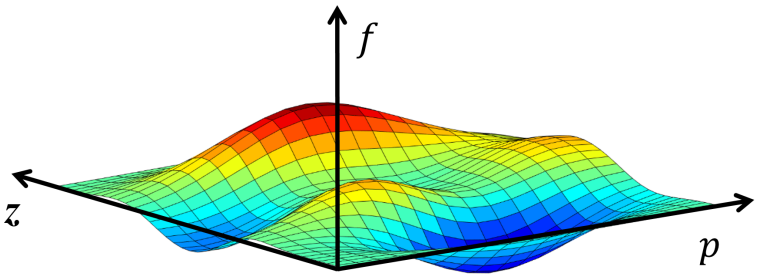

Figure 2.1: Parameterization of the operators in 2D (pressure & composition) space with a predefined OBL resolution [40]. Here, the size of the quadrilateral represents the resolution for an operator interpolation.

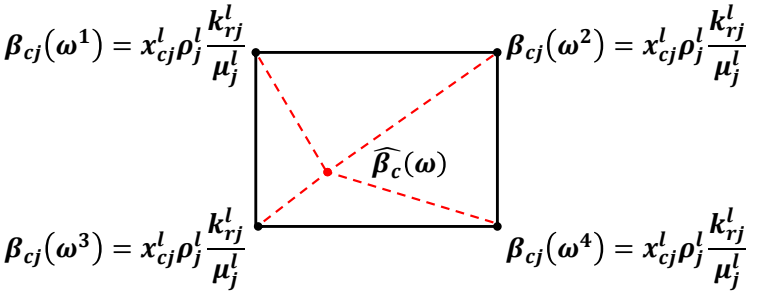

Figure 2.2: Schematic of interpolation process for β operators. ω_1 through ω_4 are four supporting points, and ω is the current physical state of a given control volume at a given timestep in the simulation. All right-hand terms are dependent only on ω_i.

2.2.4. WELL TREATMENT

A connection-based multi-segment well is used to simulate the flow in the wellbore [54]. The communication between well blocks and reservoir blocks is treated in the same way as between reservoir blocks. In addition, the top well block is connected with a ghost control volume, which is selected as a placeholder for the well control equations. The bottom-hole pressure (BHP), volumetric and mass rate controls are available in DARTS to model various well conditions.

As for the BHP well control, the injector and/or producer operate under fixed bottom hole pressure. A pressure constraint is defined at the ghost well block:

$$p - p^{target} = 0. \tag{2.20}$$

The volumetric rate control in DARTS is implemented through the volumetric rate operator $\zeta_p^{vol}(\omega)$:

$$\Gamma^l \zeta_j^{vol}(\omega)\Delta p - Q^{target} = 0, \tag{2.21}$$

where

$$\zeta_j^{vol} = \frac{\hat{s}_j(\omega)\sum_c \beta_{cj}(\omega)}{\hat{\rho}_t(\omega)}. \tag{2.22}$$

Here Q^{target} is the target volumetric flow rate at separator conditions [m^3/day], $\beta_{cj}(\omega)$ is the mass flux operator as shown in Eq. 2.12, $\hat{s}_j$ and $\hat{\rho}_t(\omega)$ are the saturation and total fluid density respectively at separator conditions.

Similarly, the mass rate control can be defined as:

$$Q_j^{mass} - Q^{target} = 0, \tag{2.23}$$

$$Q_j^{mass} = \Gamma^l \frac{\rho_p(\omega)s_p(\omega)\sum_c \beta_{cj}(\omega)}{\rho_t(\omega)}\Delta p = \Gamma^l \zeta_p^{mass}(\omega)\Delta p, \tag{2.24}$$

where Q_p^{mass} is the calculated mass rate [kg/day], $\zeta_p^{mass}(\omega)$ is the mass rate operator.

2.3. NONLINEAR CAPILLARITY OPERATOR

Gravity operators include mass density for each phase and are monotonically dependent on pressure. The derivatives of gravity operators with respect to the unknowns do not change significantly and are related to fluid compressibility. However, the relationships between capillary pressure and saturation (composition) are more complicated and highly nonlinear.

To examine the nonlinearity of this operator, we show an example of water-oil system with Corey-type capillary-pressure curve:

$$p_c(\omega) = p_d\left(\frac{S_w(\omega) - S_{wc}}{1 - S_{wc} - S_{or}}\right)^{-1/\lambda}, \tag{2.25}$$

$$\frac{\partial p_c}{\partial \omega} = \frac{\partial p_c}{\partial S_w}\frac{\partial S_w}{\partial \omega}, \tag{2.26}$$

where p_d is the capillary entry pressure, which we take as 0.2 bar. S_{wc} and S_{or} are the connate water saturation (0.12) and residual oil saturation (0.16), respectively. Both Eq. 2.25 and Eq. 2.26, are highly nonlinear equations.

Capillary pressure depends mainly on saturation in a two-phase system if hysteresis effects are not present. Typically, a capillary-pressure table, giving the relationship between saturation and capillary pressure, should be provided to interpolate the p_c value based on the saturation. In the course of the simulation, the derivative of capillary pressure with respect to the physical unknowns needs to be assembled in the Jacobian. Here we investigate the behavior of the capillary-pressure operator with the processed table.

As shown in Fig. 2.3(a), instead of plotting capillary pressure (p_c) vs. water saturation (S_w), we plot the relationship between p_c and water molar fraction (z_w), since our primary unknown variables are pressure and the overall molar fraction of each component in the grid block. With the increasing water overall molar fraction, capillary pressure decreases (behavior similar to p_c vs. S_w). The relationship between p_c and z_w is not a straight line between the two supporting points. This happens due to the different phase densities, since the relation between component overall molar fraction and saturation relies on phase densities as well. The shape of the capillary-pressure curve is represented by straight line segments with different lengths, and a finer table gives a smoother curve. A similar difference between derivatives can be found in Fig. 2.3(b). The derivatives of capillary pressure with respect to water molar fraction (z_w) exhibit discontinuities in both cases. In turn, the large discontinuities may cause numerical issues: for instance, in the Newton convergence, especially in capillary-dominated flow. With a finer resolution in the table, this issue can be moderated, thus improving the numerical performance.

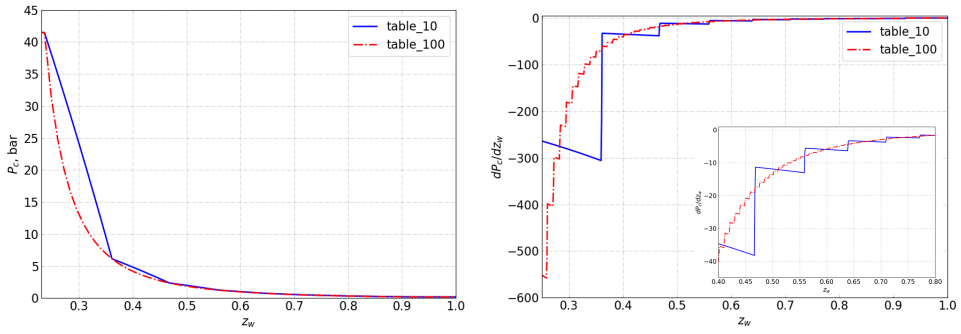

(a) (b)

Figure 2.3: Capillary pressure (a) and its derivative (b) with respect to composition. Table 10 and Table 100 represent 10 and 100 supporting points in the given table, respectively. The subfigure zooms inset in (b) locally for a better visualization.

To avoid numerical issues, one either can provide a table containing more points to interpolate p_c or fit p_c to the analytical curve to evaluate corresponding values and derivatives. In DARTS, both approaches are applied. First, an analytical capillary pressure model is defined. Then, by increasing the OBL resolution (e.g., n=100, means a p_c table with 100 supporting points for a capillary state-dependent operator), we improve the accuracy of the simulation.

2.4. IMPLICIT-TEXTURE FOAM MODEL

Currently, two fundamental approaches are used to represent the effect of foam on gas mobility: population-balance (PB) models and local-equilibrium (LE) implicit-texture (IT) models. The PB models introduce a separate variable, lamella density, which describes the number of lamellae or liquid films between bubbles, in one unit volume of the gas phase. A new balance equation for lamellae density is coupled with mass-conservation equations for each phase present in the porous medium [5, 11, 12, 55, 56]. The local lamella density is obtained through solving an additional partial differential equation at each location and timestep. A LE IT model assumes foam generation and destruction reaches a local steady-state instantaneously [13, 57–61]. In the IT model used in this project, a mobility-reduction factor (MRF), used to rescale gas mobility with foam, is introduced to implicitly represent the effect of gas bubbles. This MRF is a function of water saturation, oil saturation, surfactant concentration, capillary number, and salinity. These two types of models introduce nonlinear properties, especially when the oil is taken into account, which could increase the computational cost significantly. Moreover, foam behavior is complex, responding in an abrupt, nonlinear way to the variations of some properties, which may cause fluxes to fluctuate in time and space in simulations [62]. Population-balance models are essential for representing the entrance regions of the core or formation where foam is created, the dynamics of foam propagation at the leading edge of the foam bank, and cases where foam generation is in doubt [11]. They are much more complex than IT models, however, and must contend with the orders-of-magnitude differences in time scales of foam dynamics and the displacement [12]. Therefore we use an IT model in this project.

In these processes, foams exhibit two steady-state flow regimes based on foam quality f_g (injected gas volume fraction): the high-quality and the low-quality regime, as illustrated in Fig. 2.4(a) [63, 64]. In the high-quality regime, pressure gradient is dependent only on water superficial velocity, while it is a function of gas superficial velocity in the low-quality regime. These two regimes are essential to our understanding of foam, especially in the presence of oil.

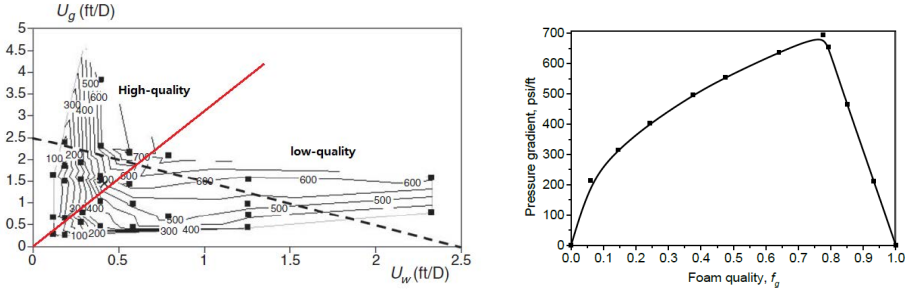

(a) Foam contour (b) Single foam-quality scan

Figure 2.4: Steady-state foam-flow regimes in porous media (data from Alverez *et al.* [64]). (a) The relationship between pressure gradient (psi/ft) and superficial velocities (ft/D) of water (U_w) and gas (U_g) at steady-state. The dotted line represents a selected scan at fixed total superficial velocity. (b) The single foam-quality scan illustrates the relationship between pressure gradient and foam quality for a fixed total superficial velocity.

The widely used IT foam model proposed in CMG-STARS [13, 65] involves two algorithms, the 'dry-out' and 'wet-foam' algorithms, to illustrate the oil effect on foam strength. In 'wet-foam' model, the oil only affect the low-quality regime, while the 'dry-out' model captures the effect of oil only in the high-quality regime. In this project, the 'wet-foam' algorithm is applied to investigate the effects of water saturation (S_w), shearing-thinning, and oil saturation (S_o) on foam stability. As shown in Eqs. 2.27 and 2.28, gas mobility is modified in the presence of foam by scaling foam-free gas relative permeability:

$$k_{rg}^{f} = k_{rg} \times FM, \tag{2.27}$$

$$FM = \frac{1}{1 + fmmob \times F_1 \times F_2 \times F_3 \times F_4 \times F_5 \times F_6}. \tag{2.28}$$

Here k_{rg}^{f} and k_{rg} are gas relative permeability in the presence and absence of foam, respectively; $fmmob$ is the maximum-attainable gas-mobility reduction (reference value); and F_1 through F_6 are functions which are used to account for the effects of different physical factors on gas mobility reduction (e.g., water saturation, surfactant concentration, capillary number, oil saturation, and salinity).

The water-saturation effect on foam stability, F_6 in the wet-foam model, is defined as

$$F_6 = 0.5 + \frac{arctan\left[epdry(S_w - fmdry)\right]}{\pi}, \tag{2.29}$$

where $fmdry$ and $epdry$ are model parameters, representing the limiting water saturation where foam collapses and the abruptness of foam collapse, respectively.

The oil effect on foam strength, F_2 in the wet-foam representation, is defined as follows:

$$F_2 = \begin{cases} 0 & fmoil \le S_o \le 1 - S_{wc} - S_{gr} \\ \left(\frac{fmoil - S_o}{fmoil - floil}\right)^{epoil} & floil \le S_o \le fmoil \\ 1 & S_{or} \le S_o \le floil \end{cases}, \tag{2.30}$$

where $fmoil$ is the upper-limiting oil saturation above which foam is destroyed completely; while $floil$ is the lower-limiting oil saturation below which oil has no impact on foam. If oil saturation is between these two values, oil destabilizes foam in a nonlinear way.

The shear-thinning function, F_3 in the wet-foam model, is defined as:

$$F_3 = \left(\frac{fmcap}{N_{ca}}\right)^{epcap}, \tag{2.31}$$

where $fmcap$ represents a reference capillary number. In STARS, F_3 is limited to values less than or equal to 1. Here we remove that restriction. $epcap$ is the exponent representing the importance of shear-thinning effects. With a larger value, foam shows stronger shear-thinning effect. The capillary number, N_{ca}, is given by

$$N_{ca} = \frac{k\nabla p}{\sigma_{wg}}, \tag{2.32}$$

where k is the absolute permeability, ∇p is the pressure gradient, and σ_{wg} is the water/gas surface tension, respectively.

In Eq. 2.27, foams change only the gas relative permeability. We schematically illustrate an example of gas-component operators parameterized at N = 100 (the supporting points in parameter space) for a binary compositional system, as shown in Fig. 2.5, to show how the OBL approach reduces the nonlinearity. Here, α_g and β_g correspond to the accumulation and flux terms of the gas component in the mass-conservation equation; p and z_w are pressure and overall molar composition of one component, i.e., primary unknown variables. A multi-component (n) isothermal system results in a set of supporting points in n-dimensional space. They are highly nonlinear in pressure-composition parameter space, especially given the sharp change of gas flux in the presence of foam. The sharp change in the flux term can make the nonlinear solver struggle to find the solution, but the OBL approach can smooth the sharp changes with sufficient accuracy, as shown in the following chapters. Meanwhile, this approach provides an opportunity to control the nonlinearity in physics by altering the operator space: that is, with a higher OBL resolution, the discretized physics is much closer to the real physics.

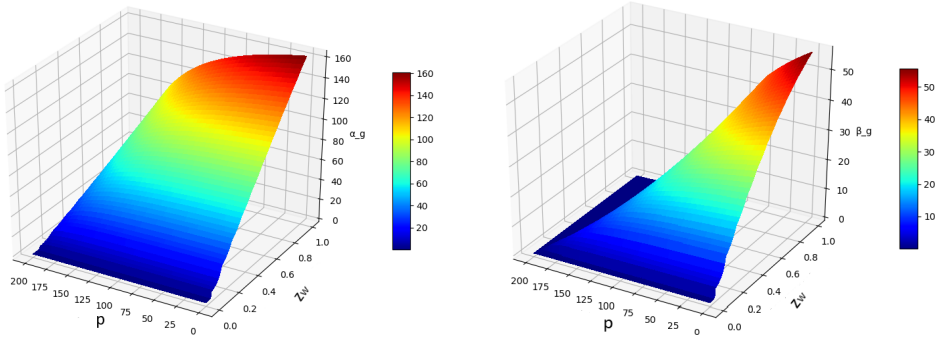

(a) Accumulation operator

(b) Flux operator

Figure 2.5: Accumulation (Eq. 2.11) and flux operators (Eq. 2.12) of the gas component in compositional system (immiscible) parameterized at N = 100. p and z_w are pressure and overall molar composition of the water component, i.e., primary unknown variables.

2.5. THERMODYNAMIC MODEL

The thermodynamic model describes the thermodynamic equilibrium between a non-aqueous phase (i.e., a multi-component mixture which can be in gas, supercritical or condensed conditions) and an aqueous phase (i.e., liquid which includes dissolved hydrocarbon and gases). Due to the instantaneous-local-equilibrium assumption, phase-behaviour calculations are decoupled from flow and transport. In a multi-phase system, an exact thermodynamic equilibrium is required at every nonlinear iteration in the mo-

lar formulation:

$$z_c - \sum_{j=1}^{n_p} \upsilon_j x_{cj} = 0, \tag{2.33}$$

$$f_c^g(p, T, \boldsymbol{x_g}) - f_c^w(p, T, \boldsymbol{x_w}) = 0, \tag{2.34}$$

$$\sum_{c=1}^{n_c} (x_{c1} - x_{cj}) = 0, \tag{2.35}$$

$$\sum_{j=1}^{n_p} \upsilon_j - 1 = 0. \tag{2.36}$$

Here $z_c = \sum_j x_{cj}\rho_j s_j \,/\, \sum_j \rho_j s_j$ is the overall composition and $f_{cj}(p, T, \boldsymbol{x_j})$ is the fugacity of component c in phase j. υ_j is the phase mole fraction. The set of thermodynamic relations described by Eq. 2.33 to Eq. 2.36 must be solved simultaneously for the conditions of pressure, temperature and composition in each grid block in the nonlinear loop.

In this work, a fugacity-activity model is used to solve for thermodynamic equilibrium based on the idea originally proposed by Kritchevsky and Iliinskaya [66]. In this approach, the fugacity of the gas phase is expressed in terms of the fugacity coefficient ($f_c^g = p\psi_c y_c$) and that of the aqueous phase in terms of activity ($f_c^w = h_c \kappa_c x_c$). In thermodynamic equilibrium ($f_c^g = f_c^w$), the phase-equilibrium constant of each component K_c can be obtained as follows:

$$K_c = \frac{y_c}{x_c} = \frac{h_c \kappa_c}{p\psi_c}, \tag{2.37}$$

where p is the total pressure in the system, ψ_c the fugacity coefficient of the gas phase, h_c Henry's constant, κ_c the activity coefficient, x_c and y_c the molar fraction of each component in aqueous phase and gas phase, respectively. Eq. 2.37 is used to calculate K values for different gas components.

The equilibrium constant for the water component is calculated with a separate relation proposed by Spycher *et al.* [67]:

$$K_{H_2O} = \frac{y_{H_2O}}{x_{H_2O}} = \frac{K^0_{H_2O}}{\Phi_{H_2O} p} exp\left[\frac{(p-1)V_{H_2O}}{RT}\right] \tag{2.38}$$

where $K^0_{H_2O}$ is the equilibrium constant of H_2O at the reference pressure of 1 bar, T is the temperature in Kelvins, V_{H_2O} the molar volume of H_2O. A more detailed description can be found in Spycher *et al.* [67].

Phase calculations are performed on all phases and phase partitioning is calculated using negative flash as described by Iranshahr *et al.* [68], with successive-substitution iteration. In order to initiate the negative-flash procedure, composition-independent ideal K-values provide an initial guess of phase fractions. Then, based on the output of the first iteration (phase fractions and composition of each phase), fugacity coefficients are updated to obtain new K-values. Once the thermodynamic system is solved, the thermophysical properties associated with the mass-conservation equations, such as phase density and phase viscosity, can be determined. The accuracy of this thermodynamic model vs. experimental results has been validated in Morshuis [69].

3

DARTS Validation for Multiphase Flow with Buoyancy and Capillarity

Summary

Numerical simulation of coupled multiphase multi-component flow and transport in porous media is a crucial tool for understanding and forecasting of complex industrial applications related to the subsurface. The discretized governing equations are highly nonlinear and usually need to be solved with Newton's method which corresponds to high computational cost and complexity. With the presence of capillary and gravity forces, the nonlinearity of the problem is amplified even farther, which usually leads to an even higher numerical cost. The Operator Based Linearization (OBL) approach effectively improves the performance of complex physical modeling. The applicability of the OBL approach was demonstrated for various energy subsurface application with multiphase flow of mass and heat in the presence of buoyancy and diffusive forces. In this chapter, the OBL approach is extended for multiphase multi-component systems with capillarity. Through the comparisons with a legacy commercial simulator using a set of benchmark tests, we demonstrate that the extended OBL scheme significantly improves the computational efficiency with the controlled accuracy of approximation and converges to the results of the conventional continuous approach with an increased parametrization resolution.

The material presented in this chapter has been published in SPE Journal 2021, 1-18 [49].

3.1. INTRODUCTION

The nonlinear convergence for simulation problems involving complex physical phenomena, such as gravity, capillarity, and chemical reactions, still remains a challenging problem. Recently, several advanced nonlinear formulations were developed to successfully address these complex problems [35, 36]. However, most of the advanced nonlinear solvers for general-purpose simulation have been developed for natural formulation [37] with explicit correction of saturation. An advanced simulation strategy for the molar formulation is still required to improve the convergence of the nonlinear solutions, especially in the presence of complex physics. The proposed OBL approach for the molar formulation provides a unique tool for an efficient representation of the complex nonlinear physics of the simulation problem.

DARTS, which is constructed based on the OBL framework, is capable of modeling complex flow and transport related to various energy applications [40, 43, 44]. The main advantage of this approach is a simplified construction of the Jacobian matrix and residuals, since the complex physics-based calculations (i.e., mainly related to the flux in the governing equations) are translated into generic multi-linear interpolation based on supporting points which are used to store the values of state-dependent operators [42]. Meanwhile, the implementation of fully-implicit simulation code is significantly simplified with the OBL methodology. The discretized PDEs and property evaluations are completely separated from each other. That simplifies the efficient, architecture-oriented implementation of advanced numerical approaches exploiting coarse-grained and fine-grained parallelism on central processing unit (CPU) and graphics processing unit (GPU) respectively [45]. It is combined with high flexibility of the simulation code: direct implementation of all properties in Python has minimal impact on simulation performance. DARTS is used to implement and test the proposed nonlinear formulation for multiphase multi-component flow in the presence of gravity and capillarity. The OBL approach is deployed to resolve the highly nonlinear problems.

In this chapter, we compare the numerical results between DARTS and a legacy reservoir simulator which uses the conventional linearization approach. A one-dimensional black-oil segregation model validates our approach. Then, five benchmark cases are selected to test the accuracy and efficiency of our new simulator: extended 1st SPE Comparative Study [70], 9th SPE Comparative Study [71], 10th SPE Comparative Study (dead-oil) [72], a UNISIM-I model [73], and 10th SPE Comparative Study (compositional). The corresponding introduction of each case is briefly described at the beginning of each comparison, which is followed by the performance of both simulators. To make the results comparable, the convergence parameters (such as maximum iterations, tolerances for both linear and nonlinear solvers) and timestep selection are made similar for both simulators, while the other parameters are kept as default. Due to the absence of detailed information about the CPU time of Jacobian assembly in the legacy simulator output, we only compare the resulting time and corresponding computational characteristics.

3.2. ONE-DIMENSIONAL HOMOGENEOUS VERTICAL RESERVOIR

Here, we build a conceptual vertical one-dimensional reservoir of 1000 m depth under buoyancy- and capillarity-driven flow with black-oil physics. Porosity and permeability

are set as constants 0.2 and 100 mD, respectively. Finite-volume discretization on a standard Cartesian grid with block size $\Delta x = 10$ m, $\Delta y = 10$ m and $\Delta z = 10$ m is applied to discretize the domain. Only gas can dissolve in the oil phase in the conventional black-oil formulation, and most of the properties described here are based on a table correlation. Initially, the top five grid cells are filled with water (higher density), whereas the bottom five cells are filled with oil (lower density). All phases are compressible. The reservoir is initialized with linearly increasing pressure (the pressure of first cell $P_0 = 260$ bar, and the increment is 10 bar/cell), and the bubble point pressure P_b is set to 270 bar. All simulations are run for 10000 days until the system reaches an equilibrium state. Stone I relative permeability and the Brooks-Corey capillary model are used to interpolate the fluid properties.

Fig. 3.1 and Fig. 3.2 show the dynamic distribution of fluids in the absence and presence of capillarity. It can be seen that without capillarity, the heavier water phase, initially placed on the top, exchanges positions with the oil phase by the end of the simulation time (Fig. 3.1). However, in the presence of capillarity, water and oil cannot segregate completely; instead, there is a transition zone forming above the bottom water-saturated cells (Fig. 3.2). In this segregation process, with decreasing water saturation, the corresponding capillary pressure between oil and water phase increases. Once the gravity force cannot overcome the capillary force, the water phase is then locked there as a remaining phase. Compared to gravity segregation without the capillary force, capillary pressure causes a lower oil saturation in the upper cells, while a higher oil saturation in the lower cells, i.e., the capillary pressure hinders the oil phase moving upwards. In both cases, a small amount of gas is released from the oil phase and accumulates on the top cell, leading to a lower oil saturation there.

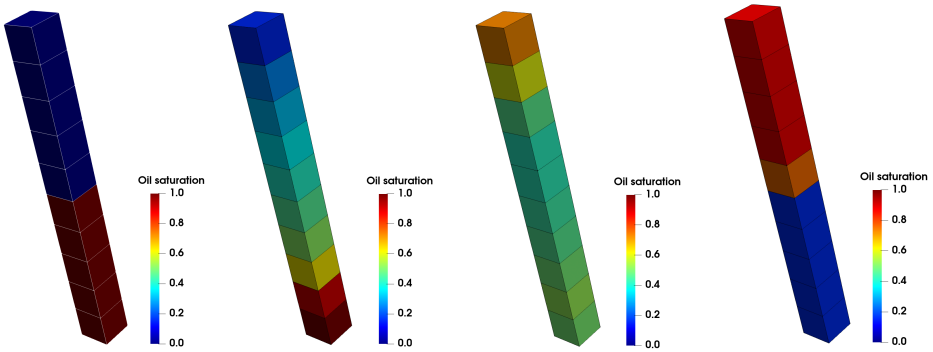

Figure 3.1: Black-oil gravity segregation: (a) Initial condition; (b) 500 days; (c) 1000 days; (d) 10000 days.

Table 3.1 presents the simulation results obtained using different OBL resolutions. The number of points in the first column represents the OBL resolution in the parameter space. The second column indicates the total number of nonlinear iterations by the end of the simulation. The third, fourth, and fifth columns correspond to the maximum differences in pressure, water saturation, and oil saturation solutions, respectively, com-

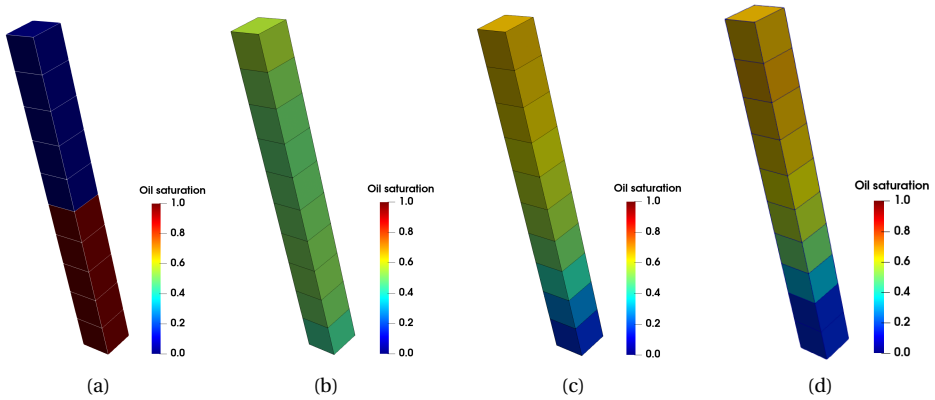

Figure 3.2: Black-oil gravity segregation with capillarity: (a) Initial condition; (b) 500 days; (c) 1000 days; (d) 10000 days.

pared to the results obtained by the legacy simulator. It can be seen from the table that with a coarse OBL resolution, there is a big difference between the solutions with conventional linearization of nonlinear physics vs. the parametrized solutions, especially for pressure. However, if the OBL resolution increases, the difference decreases significantly, corresponding with a minor increase in the nonlinear iterations.

This is because as parametrization in physics is refined, the shape of state-dependent operators becomes more nonlinear, causing the increase in nonlinear iterations. At the same time, the number of nonlinear iterations for 500 points and 1000 points is nearly the same, while the discrepancy of pressure is significantly reduced. This reflects the fact that the location of points in the current OBL approach is chosen blindly, depending on a uniform distribution without any analysis of nonlinearity [42]. The comparison of CPU time shows that the computational cost is reduced significantly by utilizing the OBL approach, compared to the conventional simulation. As a result, DARTS exhibits both high accuracy and robustness.

Table 3.1: Numerical difference and nonlinear behavior of 1D black oil simulation.

Resolutions	Newton iterations	E_p	E_{sw}	E_{so}	CPU time, s
Legacy simulator	1198	-	-	-	5.5
n = 100	1196	42.0	0.007	0.035	0.192
n = 500	1227	6.9	0.007	0.024	0.297
n = 1000	1230	2.38	0.002	0.015	0.324

3.3. BENCHMARK STUDIES

3.3.1. 1ST SPE COMPARATIVE SOLUTION PROJECT

This is a basic test for a three-phase three-component black-oil modeling technique by using gas flooding. The top of the reservoir is at 2540.0 m with the total thickness of 30

m. The corresponding PVT properties, relative permeabilities, and reservoir conditions can be found in [70]. The difference with the original model is that in this case the capillary effect is included, which increases the nonlinearity of the problem. There are two vertical wells located in the opposite corners of the domain: gas is injected from the top layer with fixed BHP (400 bar), whereas oil is produced from the bottom layer by controlling the oil production rate (3000 m^3/day). The Stone I relative permeability model and the Brooks-Corey capillary-pressure model are used to interpolate the fluid properties. In water-oil system, p_d is 0.2 bar and the exponent λ is 0.5, while in gas-oil system, p_d is 0.12 bar and the exponent λ is 0.8. Then we can obtain the corresponding capillary pressure curves using Eq. A.3. All simulations are run for 10 years with a maximum timestep of Δt = 10 days. There is no gas in the initial condition. The big density difference between liquid and gas leads to small changes in gas composition (i.e., higher OBL resolution is required to interpolate gas properties). In order to reduce the OBL performance and keep the accuracy, we take logarithmic axes for composition-space instead of using uniform parametrization-space in this case with an OBL resolution of 1000.

Fig. 3.3 shows the comparison of well rates and BHP of producer between two simulators. Before the gas breakthrough, the oil production rate keeps constant with a certain gas-oil ratio (GOR). Once the injected gas arrives at the producer, the oil production rate decreases quickly; the gas production rate, however, increases significantly, leading to a lower BHP at the producer. Under the chosen OBL resolution, DARTS demonstrates a good match with the solution of the legacy simulator.

Fig. 3.4 shows the results by the end of the simulation. Gas is injected from the top layer, leading to a relatively higher gas saturation and lower oil saturation on the top layer (Fig. 3.4(b) and Fig. 3.4(c)). In order to show the solution difference of each layer between DARTS and the legacy simulator, the l_2 norm is adopted to evaluate the relative difference in each layer. The normalized difference of k^{th} layer can be calculated as follows

$$e^k = \frac{\|\vec{x_1}^k - \vec{x_2}^k\|_2}{\|\vec{x_2}^k\|_2}. \tag{3.1}$$

The relative differences of pressure and water saturation are plotted in Fig. 3.5(a). As is shown, the relative difference of each layer is pretty small (pressure difference is below 2.0%, and maximum gas saturation difference is below 3.5%) under this OBL resolution, which exhibits a good match between two very different simulation software.

Fig. 3.5(b) displays the performance of DARTS and the legacy simulator in terms of nonlinear iterations, linear iterations, and CPU time. The number of nonlinear iteration of DARTS is slightly reduced (790 vs. 803), but DARTS requires more linear iterations compared to the legacy simulator (3164 vs. 2116). However, due to the implementation of the OBL approach, the computational cost is in turn reduced significantly, around 3 times faster than the legacy simulator (1.25 seconds vs. 3.42 seconds). In order to improve the simulation performance by another order of magnitude further, one can run DARTS at GPU architecture [45].

3.3.2. 9TH SPE COMPARATIVE SOLUTION PROJECT

Here, we present the 9th SPE comparative project, which is based on 24×25×15 grid blocks placed on a dipping, initially undersaturated reservoir (dipping angle of 15 de-

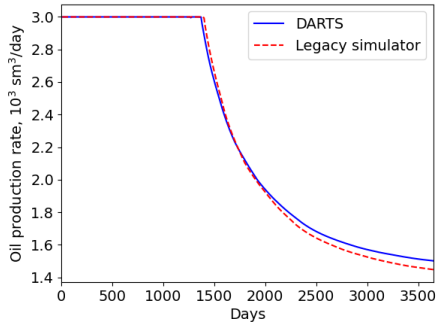

(a) Oil production rate

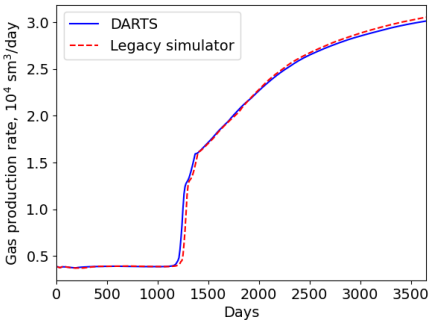

(b) Gas production rate

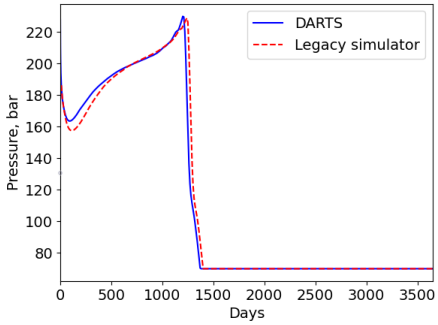

(c) BHP of producer

Figure 3.3: Comparison of well rates and BHP of producer with different simulators.

grees in X-direction). The top of the reservoir is at 2743.2 m and the total thickness is 109.422 m with variations in each layer. The grid block is in conventional rectangular coordinates without local grid refinement. The reservoir has a high degree of heterogeneity provided by a geostatistically-based permeability field, as shown in Fig. 3.6(a). The permeability varies within the layers, whereas the porosity and thickness are homogeneous in every layer. There are 25 producers and a single water injector. All wells are operated under a constant rate. The water injector is set to a maximum rate of 795 m^3/day with a maximum bottom-hole pressure of 300 bar. The maximum oil rate for all producers is set at 240 m^3/day in the beginning; at 300 days, the rate is switched to 15.9 m^3/day for all wells. Finally, at 360 days, the rate is again raised to 240 m^3/day for all producers until the end of the simulation at 900 days. The minimum bottom-hole pressure for all producers is set to 70 bar. Taking the great heterogeneity of the reservoir and complex physics into account, we directly use a higher OBL resolution with 1000 supporting points in the logarithmic space.

One interesting feature of the water-oil capillary-pressure curve, as shown in Fig. 3.6(b), is the discontinuity around $S_w = 0.35$. After this saturation, the capillary pressure becomes negative. Such a discontinuity usually causes difficulties in Newton-Raphson convergence for cases in which water saturations are changing significantly. Another

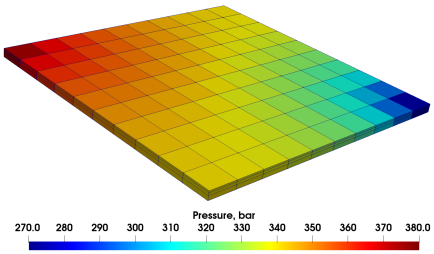

(a) Pressure

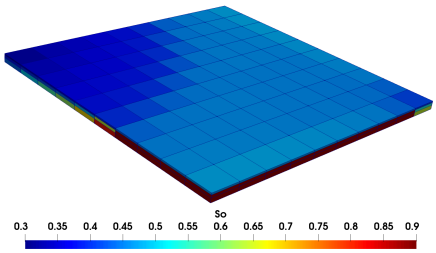

(b) Oil saturation

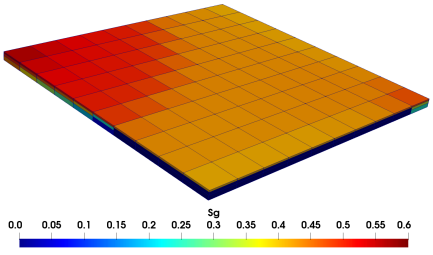

(c) Gas saturation

Figure 3.4: Pressure and saturation profiles at t = 10 years.

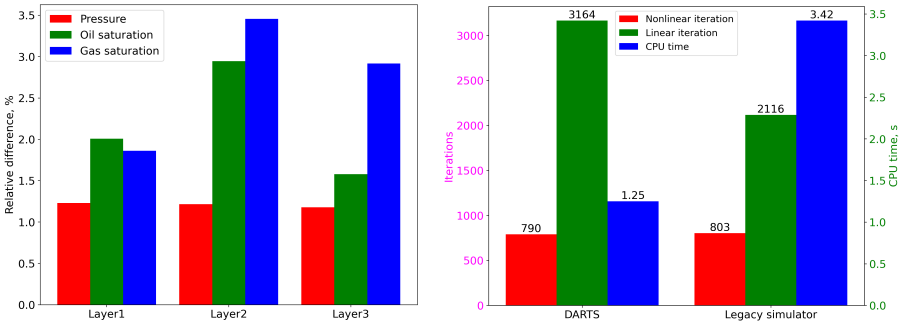

(a) Relative difference

(b) Performance

Figure 3.5: The accuracy and performance of two simulators for the 1st SPE comparative study. (a) Relative difference of pressure and saturation between DARTS and the legacy simulator in each layer; (b) Comparison of the numerical performance between two simulators.

feature of the capillary-pressure curve is the tail, which does not extend to a water saturation of 1.0. This feature does represent reality in certain reservoirs where imbibition may have occurred due to tectonics prior to discovery [71]. The main purpose of this test case is to investigate the complications brought by a high degree of heterogeneity in the permeability field and the highly nonlinear capillary pressure curve.

Fig. 3.7 displays the instantaneous well rates for the injector and all producers. The

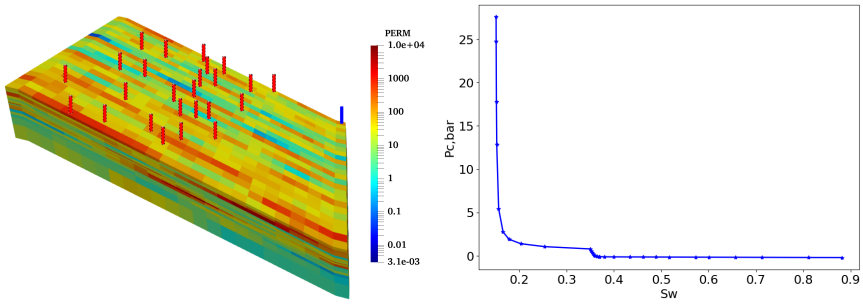

(a) (b)

Figure 3.6: Permeability distribution (a) and water-oil capillary pressure curve (b) in the 9th SPE comparative project.

difference between the two simulations is negligible. In gas production rate (Fig. 3.7(b)), there are more pronounced differences in the first 40 days, which we again address by a slightly different well implementation. Saturation and pressure maps by the end of simulations are shown in Fig. 3.8. With water injection, oil is displaced to the producers located at the top of the domain, resulting in a lower oil saturation near the water-saturated region. The pressure is also lower on the top of the domain. Once it is below bubble point pressure, gas evaporates from oil and accumulates in the upper part of the reservoir, leading to higher gas saturation there. Fig. 3.9(a) illustrates the relative difference of each layer between DARTS and the reference (l_2 norm). The differences of pressure and saturations are around 2.0%. These results indicate the capacity of the OBL approach to accurately model complex physical problems with convection, buoyancy, and capillarity.

Fig. 3.9(b) shows the numerical performance of DARTS and the legacy simulator. It can be seen that DARTS takes fewer nonlinear iterations compared to the legacy simulator (379 vs. 438), while the number of linear iterations of DARTS is still higher (3689 vs. 1064). In terms of computational time (12.50s vs. 19.17 seconds), DARTS is more efficient although the performance gain is not very significant.

3.3.3. UNISIM-I PROJECT

The UNISIM-I model is a synthetic model using publicly available data from the Namorado Field, Campos Basin, Brazil. This model is designed for uncertainty reduction [74]. There are four conditioning vertical wells to obtain the initial porosity distribution by petrophysical modeling (Fig. 3.10(a)), and one porosity-permeability correlation is used to interpolate the permeability distribution (Fig. 3.10(b)). This reservoir is highly heterogeneous, with several faults. The domain is discretized into a corner-point grid with 81×58×15 cells (28676 active cells). This project contains 14 production wells and 11 injection wells. The maximum oil rate for all producers is set at 800 m^3/day with a maximum bottom-hole pressure of 35.3 bar, and all injectors are controlled by a water injection rate of 1200 m^3/day. Other reservoir parameters are described in [73]. The simulation time spans 10 years with a maximum timestep of 15 days. In the original model,

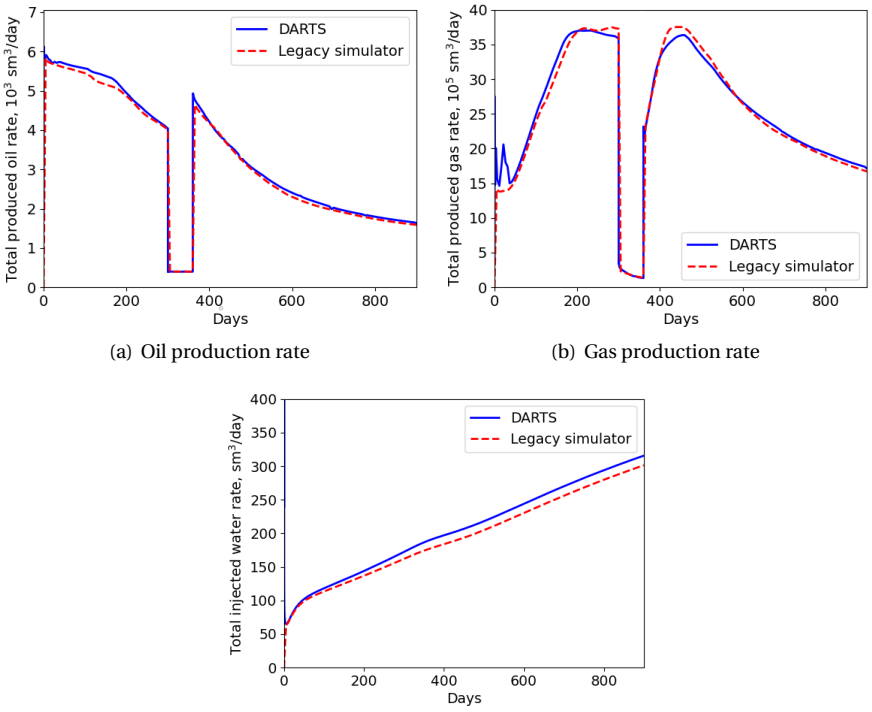

(a) Oil production rate

(b) Gas production rate

(c) Water injection rate

Figure 3.7: Comparison of total well rates between DARTS and reference for 9th SPE Comparative Solution Project.

the capillary pressure between the gas phase and the oil phase is ignored. Therefore, we consider only the capillary pressure between oil and water phase. An OBL resolution with 1000 supporting points in logarithmic space is utilized in this case as well.

Fig. 3.11 displays the total well rates for all producers. There is a small deviation from the reference solution but in general, the match is acceptable. Pressure and oil saturation profiles between the two simulators are shown in Fig. 3.12. The relative difference of each layer (Eq. 3.1) in terms of pressure and saturation is displayed in Fig. 3.13(a). In this case, by the end of the simulation, the differences between the results of the two simulations vary insignificantly.

Fig. 3.13(b) shows the performance of two simulators by the end of the modeling period. DARTS requires fewer Newton iterations by utilizing the OBL approach. As in the previous cases, DARTS needs more linear iterations to converge (2064 vs. 1081), while the computational performance of DARTS is better (56.0s vs. 142.95 seconds).

3.3.4. 10TH SPE COMPARATIVE SOLUTION PROJECT

This is another benchmark problem involving oil production from a severely heterogeneous reservoir by using a waterflooding technique. The top of the reservoir is at 3657.6

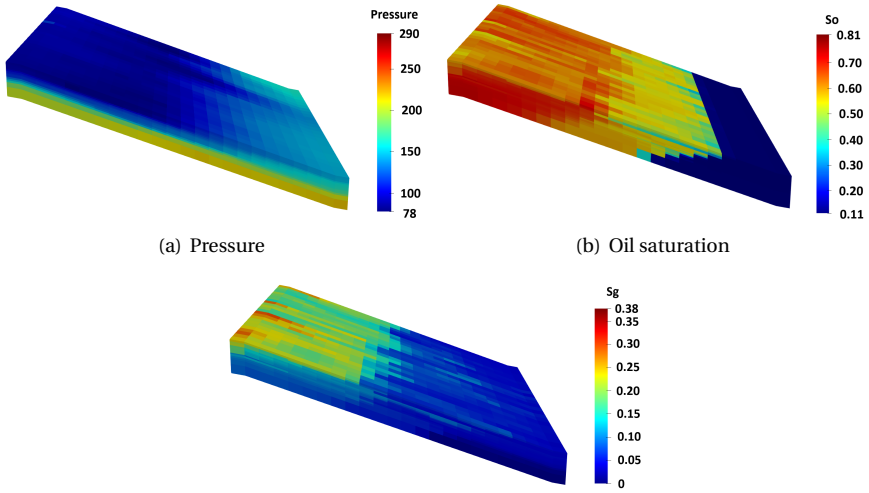

(a) Pressure (b) Oil saturation

(c) Gas saturation

Figure 3.8: Simulation results of pressure and saturations at the end of simulation.

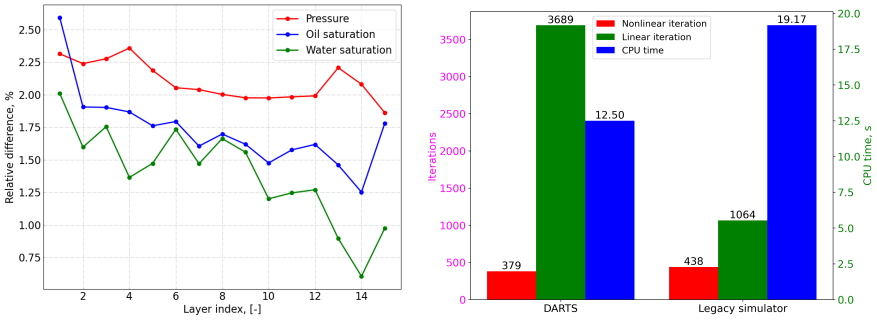

(a) Relative difference (b) Performance

Figure 3.9: The accuracy and performance of two simulators for the 9th SPE comparative study. (a) Relative difference of pressure and saturation between DARTS and the legacy simulator in each layer; (b) Comparison of the numerical performance between two simulators.

m and the total thickness is 51.8 m. Because the full model challenges the linear solver of the legacy simulator too much, we only extract the 7^{th} layer of shallow-marine Tarbert formation (corresponding thickness is 0.6096 m). The formation, which is characterized by large permeability variations (Fig. 3.14(a)), is defined on a regular Cartesian grid with 60 × 220 × 1 (13200) cells. The porosity field (Fig. 3.14(b)) is strongly correlated to the permeability. We add a capillary-pressure curve (Fig. 3.14(c)), using the Brooks-Corey model (p_d = 0.15 bar, and λ = 0.8). There are four producers (at four corners) operated under constant bottom-hole pressure (150 bar) and one water injector (in the center) with a constant injection rate (5 m^3/day). A five-spot layout is used for wells location. In

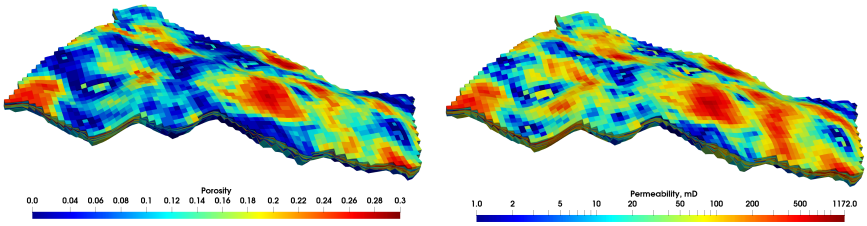

(a) Porosity (b) Absolute permeability

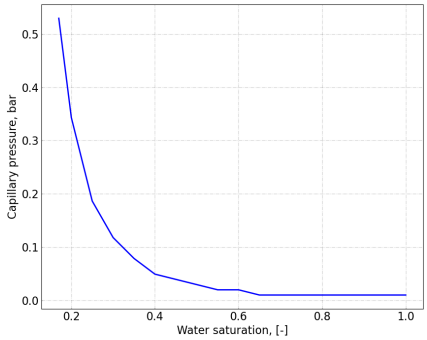

(c) Capillary curve

Figure 3.10: Porosity and permeability distribution, and capillary pressure curve of UNISIM-I model.

this case, the OBL resolution is set to 1000 points. All simulations are run for 1000 days with a maximum timestep of $\Delta t = 10$ days since the legacy simulator in the default mode has a convergence issue with larger timesteps. The other parameters, such as relative permeability and PVT table, can be found in [72].

Fig. 3.15 shows the changes in total oil production rate, total water production rate, and BHP of the injector. Before water breakthrough, only oil is produced, and its rate increases with time. Once the water breaks through to the producers, the total oil production rate starts to decrease due to the higher relative mobility of the water phase. In the presence of highly nonlinear convective flow, gravity and capillarity, DARTS shows a perfect match with the legacy simulator. Due to the high level of heterogeneity, the saturation of the domain varies over a large range (Fig. 3.16(c)). Water can easily displace the oil in the high-permeability zone, leading to relatively low oil saturation. However, oil is hard to move in the low-permeability region. The relative differences of pressure and water saturation in this layer are plotted in Figs. 3.16(b) and 3.16(d). As is shown, the relative difference is reasonably small (pressure below 1.0% and saturation below 3.0%) under the chosen OBL resolution, which again exhibits a good match between two very different simulation codes.

Fig. 3.17(a) shows the performance of two simulators. In this case, DARTS takes only around 13 seconds, with 358 Newton iterations and 4328 Linear iterations; the legacy simulator, however, takes 24 seconds and requires 412 Newton iterations and 3279 Linear iterations. With a larger timestep ($\Delta t = 20$ days), the legacy simulator would experi-

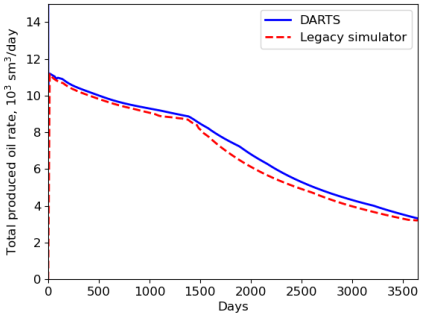

(a) Oil production rate

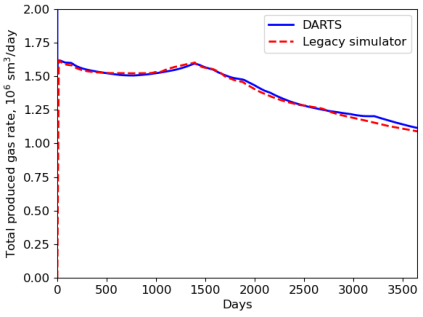

(b) Gas production rate

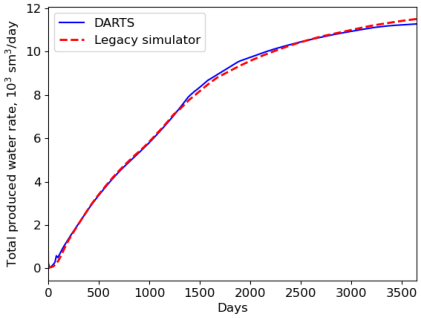

(c) Water production rate

Figure 3.11: Comparison of total well rates between DARTS and legacy simulator for UNISIM-I Project.

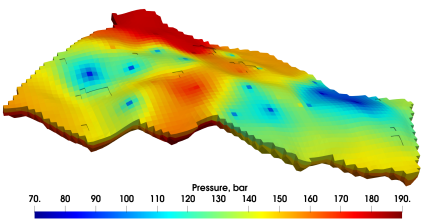

(a) Pressure

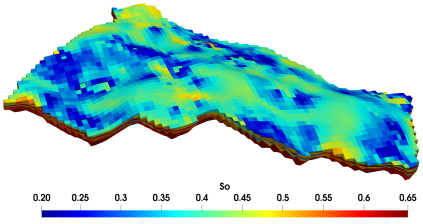

(b) Oil saturation

Figure 3.12: Comparison of pressure and oil saturation distribution between DARTS and legacy simulator.

ence convergence issues in a few timesteps. DARTS, however, is more robust and keeps the same accuracy. It indicates that the combined implementation of linear and nonlinear solution strategies using the OBL approach not only simplifies the construction of Jacobian and residual but also significantly improves the performance of the simulation process when tackling complex physical problems.

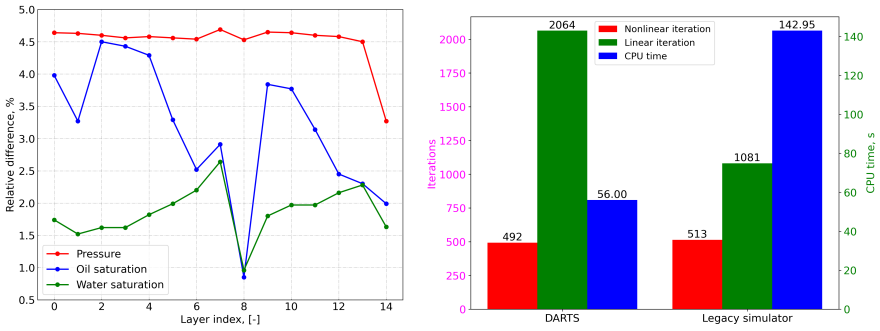

(a) Relative difference (b) Performance

Figure 3.13: The accuracy and performance of two simulators for UNISIM model. (a) Relative difference of pressure and saturation between DARTS and the legacy simulator in each layer; (b) Comparison of the numerical performance between two simulators.

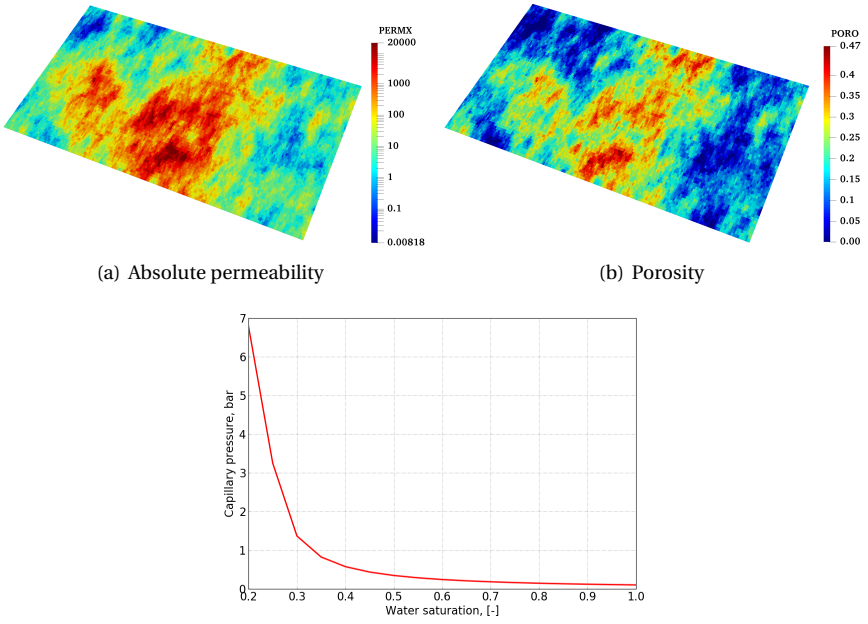

(a) Absolute permeability (b) Porosity

(c) Capillary curve

Figure 3.14: Porosity and permeability distribution, and capillary pressure curve of the 10th SPE comparative study.

3.3.5. COMPOSITIONAL 10TH SPE COMPARATIVE SOLUTION PROJECT

To further investigate the performance of the OBL approach, we run the simulation for an isothermal injection of carbon dioxide (CO_2) and methane (CH_4) into a four-component oil using the 10th SPE comparative study reservoir description. This model

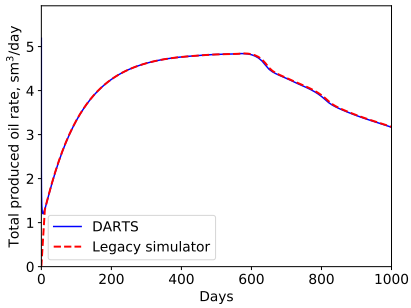

(a) Total oil production rate

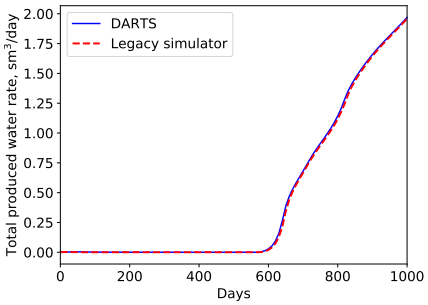

(b) Total water production rate

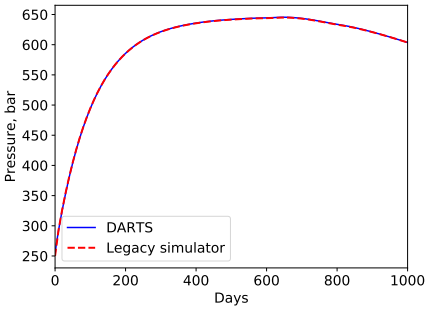

(c) Injector BHP

Figure 3.15: Comparison of total production rate and injector BHP between DARTS and legacy simulator.

is similar to one used in [42]. The initial oil consists of four components, i.e., CO_2 (1.0%), CH_4 (11%), C_4 (38%), and C_{10} (50%) following [75]. The initial reservoir pressure and temperature are 90 bar and 353 K, respectively. A mixture of 80% of CO_2 and 20% of C_1 is injected from the injector in the center at a BHP control equal to 120 bar (near-miscible conditions). The four producers at the corners are operated at BHP of 60 bar. The relative permeability and capillary pressure curves for gas-oil system are from [76]. The Peng and Robinson [77] equation of state and the Lohrenz-Bray-Clark correlations [78] for viscosity model are used to evaluate phase behavior and properties, same as that in [42]. All simulations are run for 1000 days with a maximum timestep of Δt = 10 days. After a convergence investigation, an OBL resolution with 64 supporting points in normal space is utilized in this case since a relatively low resolution already provides high accuracy, as shown in [42] where the capillary pressure is neglected.

Fig. 3.18 shows the distribution of CO_2 composition and the difference between the two simulators by the end of the simulation. The difference is mainly distributed near the leading displacement shock. Fig. 3.17(b) shows the performance of two simulators. In this compositional kernel, DARTS significantly improves the performance of the simulation process compared to the dead-oil and black-oil kernels, corresponding to fewer nonlinear (510 vs. 645) and linear iterations (5870 vs. 6191). DARTS takes around 36 seconds, nearly three times faster than the legacy simulator. In DARTS, only 13956 sup-

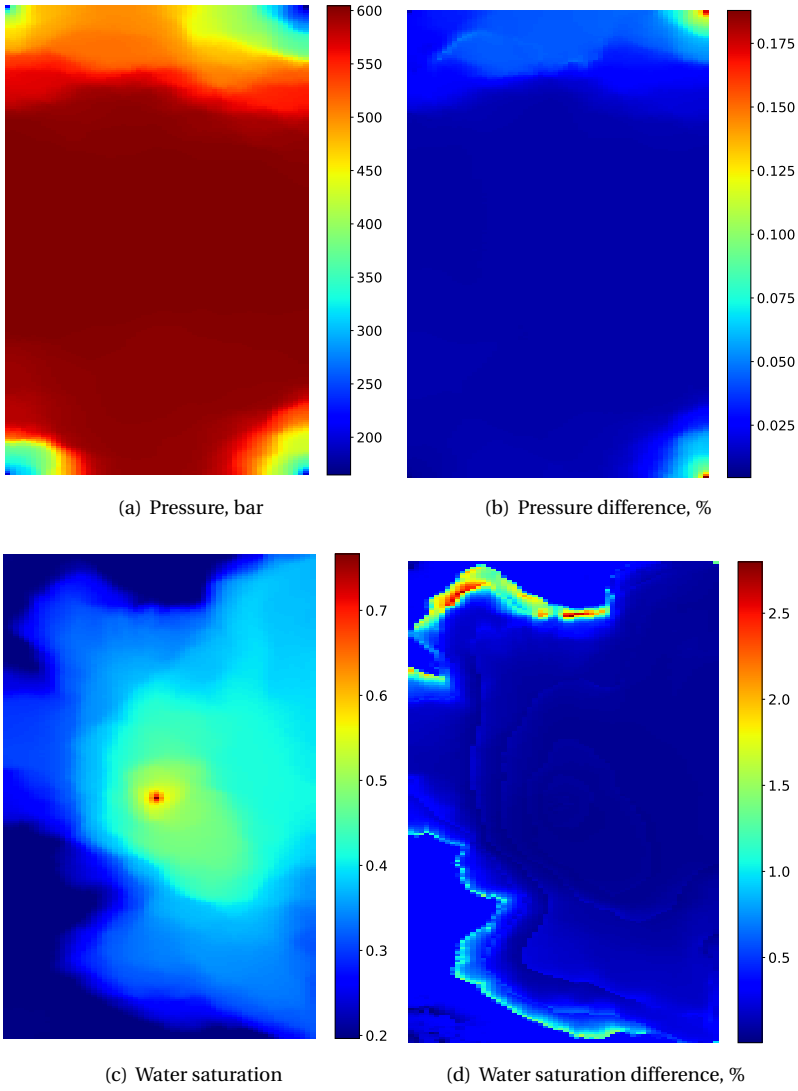

(a) Pressure, bar

(b) Pressure difference, %

(c) Water saturation

(d) Water saturation difference, %

Figure 3.16: Comparison of pressure and water saturation distribution between DARTS and legacy simulator.

porting points (0.083% of entire parameter space) are evaluated to obtain phase properties in the simulation; the legacy simulator, however, requires 8.514×10^6 times, i.e., all blocks need to perform phase-behavior evaluations in each nonlinear iteration, which is a computationally expensive process. It further indicates the ability of the OBL approach to improve the performance of the simulation with complex physical problems.

Due to the implementation of adaptive parametrization approach, all the computed supporting points are stored after the simulation. For the second or further runs, we can

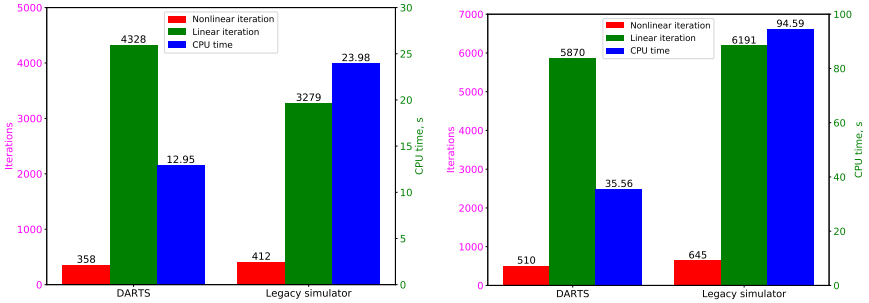

(a) Dead-oil kernel (b) Compositional kernel

Figure 3.17: The performance of two simulators for the 10th SPE comparative study with different physics.

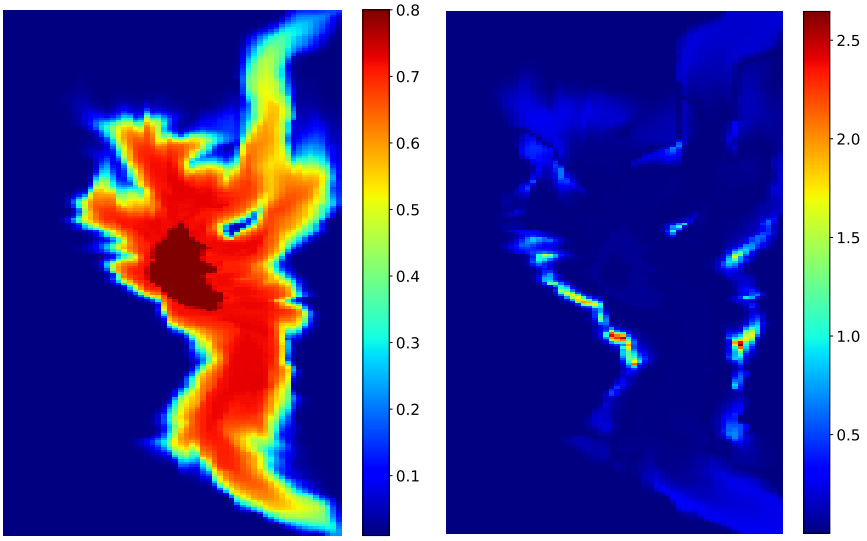

(a) CO_2 composition (b) CO_2 composition difference, %

Figure 3.18: Comparison of CO_2 composition distribution between DARTS and legacy simulator.

avoid property computations almost completely by loading previously computed points. This process can speed up the simulation in optimization or uncertainty quantification studies quite significantly if the time cost for points generation is large.

3.4. CONVERGENCE OF OBL RESULTS

Table 3.2 shows the numerical convergence of DARTS on the desktop Intel(R) Xeon(R) CPU 3.50GHz. We perform the convergence study by setting a threshold for the difference in pressure (1%) and saturations (1%) between the exhaustive OBL resolution (10^6 points) close to the continuous physics and the OBL resolution, which provides the so-

lution satisfying the threshold (the second column in the table). The last two columns show the Newton iterations of the reference case (exhaustive OBL resolution) and current realization (OBL resolution in the second column). Once the solution is below the threshold, the number of nonlinear iterations does not change much. Generally, the black-oil kernels require a higher OBL resolution to converge to the reference solutions due to the more nonlinear three-phase properties. In the investigated benchmark cases, the selected OBL resolution (1000 points) always satisfies the convergence criteria. The reduced number of interpolation points can help with advanced nonlinear solvers based on a second-order analysis of parametrization tables, similar to one proposed in [79].

Table 3.2: Convergence performance of DARTS and reference.

Scenarios	OBL resolution	E_P, %	E_{So}, %	E_{Sw}, %	Newton iterations	
					Reference	Current realization
1st SPE comparative study	220	0.313	0.854	0.466	798	804
9th SPE comparative study	500	0.823	0.383	0.473	383	392
UNISIM-I	680	0.473	0.285	0.330	497	506
10th SPE comparative study	20	0.012	0.028	0.042	306	298
Compositional 10th SPE comparative study	30	0.026	0.035	-	486	492

3.5. DISCUSSION

In this work, we extend the capacity of DARTS to the modeling of petroleum-related applications with gravity and capillarity. In the presence of buoyancy and capillarity, the nonlinearity of the system of governing equations is amplified. The newly proposed linearization approach is implemented in DARTS to control the nonlinearity of the coupled system by grouping the variables depending on the physical state into operators. These state-dependent operators are evaluated and stored at vertices of parameterization space. In the course of the simulation, a multi-linear interpolation is used to interpolate the corresponding values and derivatives of operators.

Through the set of benchmark tests based on dead-oil, black-oil , and compositional physical kernels, we demonstrate the high accuracy and good performance of the OBL approach to solve the problems with complex nonlinear physics. However, there are still two limitations which need to be resolved in future research:

1. In the current approach, the location of the supporting points is chosen blindly based on a uniform distribution. In the black-oil kernel, gas density is usually relatively low, leading to a small gas composition of the mixtures. Therefore the presence of gas requires a higher OBL resolution to reproduce the reference results, which, in turn, increases the computational cost. The transformation of the interpolation kernel into a logarithmic scale can solve this problem to some extent. However, we still need to explore more-efficient alternatives.

2. In the presence of gravity and capillarity, the PPU scheme is applied in our framework to approximate the numerical flux. The number of operators involved in OBL with PPU approximation increases by $[(n_c+1)n_p]$, which increases the computational cost, since more time is required to interpolate the values of different operators. One approach, named component-potential upwinding, which can reduce

the number of operators, is proposed in Khait [80] and will be effectively coupled with capillary operators in future research.

In simulations, the table resolution is one key factor that affects the accuracy of the OBL approach. A coarser parameterization space, corresponding to a smaller OBL resolution, usually gives a greater deviation from the conventional solution [38, 42]. To choose a proper resolution, a sensitivity study is required, similar to one shown in Table 3.2. Notice that this study can be performed on a simplified 1D model. In order to improve the accuracy, a higher OBL resolution can always be applied considering the efficiency of the advanced linearization scheme.

To demonstrate the ability of DARTS to perform challenging buoyancy-capillary dominated simulation, we include only relatively simple physical kernels corresponding to the dead-oil, black-oil and compositional physics. In the future, we will test the applicability of the OBL approach to more complicated physics describing foam EOR and CO_2 sequestration processes where gravity and capillarity play a crucial role. Another focus of our future work is to reduce the number of operators, especially for the convective flux operators, thus improving the performance of the OBL approach. We also expect that we will be able to improve performance even further by using specifically designed nonlinear solvers for the OBL approach.

3.6. CONCLUSIONS

In this study, the ability of handling complex physical models in DARTS is investigated for several benchmark tests in the presence of buoyancy and capillarity. We compare the accuracy and computational performance of DARTS against a commercial legacy simulator widely utilized in the petroleum industry. DARTS can reproduce the results of the legacy simulation with a negligible difference. By approximating the reference physics based on parameterization, the Operator-Based Linearization (OBL) approach simplifies the assemble of Jacobian at the linearization stage, leading to a better simulation performance. In all simulation tests, starting from the 1D homogeneous model and finishing with 3D highly-heterogeneous models, OBL resolution plays an important role in the accuracy of the OBL approach. With increasing degrees of freedom in the simulation problem, DARTS shows its advantages to speed up the modeling process.

4

FOAM ENHANCED OIL RECOVERY PROCESSES

Summary

Foam injection is a promising enhanced oil recovery (EOR) technology through significantly improving the sweep efficiency of gas injection. Simulation of foam-oil displacement in reservoirs is an expensive process for conventional simulation due to the strongly nonlinear physics. In this chapter, the Operator-Based Linearization (OBL) approach, combined with the representation of foam by an implicit-texture (IT) model with two flow regimes, is extended for simulation of foam EOR process. The numerical-simulation results are validated by using three-phase fractional-flow theory for foam-oil flow. Starting with an initial guess based on the fitting of steady-state experimental data with oil, the OBL foam model is regressed to experimental observations using a gradient-optimization technique. A series of numerical validation studies are carried out to investigate the accuracy of the proposed approach. The numerical model shows good agreement with analytical solutions at different conditions and with different foam parameters. The foam-quality scan is accurately fitted to steady-state experimental data, except in the low-quality regime. 1D and 3D simulation results clearly demonstrate two stages of foam propagation from inlet to outlet as seen in the CT coreflood experiments.

The material presented in this chapter has been published in SPE Journal 2021, 1-18 [50].

4.1. INTRODUCTION

Foam, discontinuous gas bubbles separated by liquid films, can improve the injection profile in gas-injection processes by reducing or mitigating the effects of high gas mobility and reservoir heterogeneity [4–6, 81]. Currently, foam is widely used in gas EOR, well-stimulation, and soil remediation processes [82–84]. Recently, the foam EOR technique is being extended to CO_2 storage, thus reducing greenhouse gas emissions [8, 9, 85–87]. In these processes, foams mainly exhibit two steady-state flow regimes based on foam quality f_g (injected gas volume fraction): the high-quality and the low-quality regime, as illustrated in Fig. 4.1 [63, 64]. In the high-quality regime, pressure gradient is dependent only on water superficial velocity, while it is a function of gas superficial velocity in the low-quality regime. These two regimes are essential to our understanding of foam, especially in the presence of oil. Due to the limited data available on foam/oil interaction, studies extending the model to oil are relatively few [88–90]. This issue hinders the reliable design of foam processes.

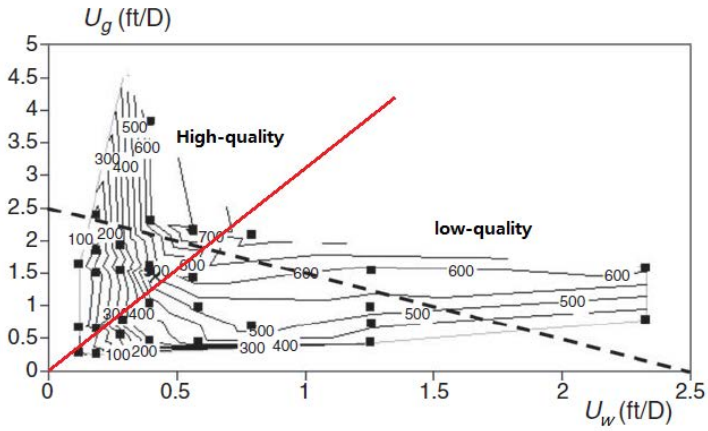

Figure 4.1: The relationship between pressure gradient (psi/ft) and superficial velocities (ft/D) of water (U_w) and gas (U_g) at steady-state, from Alverez *et al.* [64]. Dotted line represents a salinity scan at fixed total superficial velocity.

Some researchers have conducted laboratory experiments or field pilots to understand the complicated foam rheology and the mechanics of foam EOR with the presence of oil in porous media. Mannhardt *et al.* [91] found that oil can kill foam completely once the oil saturation is greater than a critical oil saturation. This critical oil saturation represents the effect of oil on foam at local-equilibrium [65]. This saturation is dependent on the type of oil, rock, and surfactant chemistry. However, there is not a broad range of experimental data to prove this theory in this literature. Some studies [92–95] investigated the oil effect on foam and found most oils reduce foam stability, but did not provide a quantitative predictive model for the effect of oil.

Even though there are numerous laboratory studies and field pilots on foam properties, numerical simulations of foam rheology and flow are relatively few, especially in the presence of oil in a porous medium, due to the challenges of accurate simulation

and numerical issues. Hussain *et al.* [96] found a single-cycle surfactant-alternating-gas (SAG) flood can result in two different regions in a 3D case where the mobile oil is present: that is, foam overriding oil and gas overriding the foam. However, so far, there is no experimental evidence to prove their simulation results. Hosseini-Nasab *et al.* [97] investigated the applications of IT foam model for simulating foam flow in the presence of an oleic phase through Puma-Flow reservoir simulator. The 1D model, however, causes some discrepancies between the measured and numerically calculated oil recovery data. To design miscible CO_2-foam flooding in a field trial, Alcorn *et al.* [17] presented an integrated upscaling approach based on the East Seminole Field and provided an improvement to the overall CO_2-foam field pilot project design. However, the underlying mechanism of the oil effect on foam strength is not a focus of their work because the foam-quality scan is performed on water-saturated cores.

Currently, two fundamental approaches, population-balance (PB) models and local-equilibrium (LE) implicit-texture (IT) models, are used to represent the effect of foam on gas mobility. The PB models introduce a separate variable, lamella density which describes the number of lamellae in one unit volume of the gas phase, in a new balance equation coupled with mass-conservation equations for each phase present in the porous medium [5, 11, 12, 55, 56]. The local lamella density is obtained through solving this additional partial differential equation at each location and timestep. The LE IT modeling assumes foam generation and destruction reaches a local steady-state instantaneously [13, 57–61]. A mobility-reduction factor (MRF), used to rescale gas mobility with foam, is introduced to implicitly represent the effect of gas bubbles. This MRF is a function of water saturation, oil saturation, surfactant concentration, capillary number, and salinity. These two models introduce nonlinear properties, especially when the oil is taken into account, which could increase the computational cost significantly. Moreover, foam behavior is complex, responding in an abrupt, nonlinear way to the variations of some properties, which may cause fluxes to fluctuate in time and space in simulations [62]. Population-balance models are essential for representing the entrance regions of the core or formation where foam is created, the dynamics of foam propagation at the leading edge of the foam bank, and cases where foam generation is in doubt [11]. They are much more complex than IT models, however, and must contend with the orders-of-magnitude difference in time scales of foam dynamics and the displacement [12]. Therefore we use an IT model here, and the model can be found in Section 2.4.

In order to accurately simulate these highly nonlinear foam EOR processes, a finer computational grid in space or time should be implemented, which in turn is counterbalanced by the increase of the simulation cost. The OBL approach is applied to improve the performance of numerical simulation. In simulations, the resolution of the parameter space is one key factor that affects the accuracy of the OBL approach. To choose a proper resolution, a sensitivity study is required. A coarser parameterization space, corresponding to a smaller OBL resolution, can provide satisfying results, with higher efficiency compared with some academic or legacy simulators in previous tests [42–44]. The proper implementation of the OBL approach can speed up Jacobian assembly by an order of magnitude and even faster on GPU architecture [45], which saves computational costs significantly. In order to improve the accuracy, a higher OBL resolution can be always applied considering the efficiency of the new linearization scheme.

In this chapter, first, the wet-foam model is examined, where oil changes only the mobility of full-strength foam in the low-quality regime and has no direct effect on the high-quality regime (Ref. Section 2.4). Then the numerical-simulation results are validated using three-phase fractional-flow theory for foam-oil flow and investigate the effects of grid resolution on the results. Next we successfully obtain the parameters of the wet-foam model by fitting a single foam-quality scan using a least-squares optimization approach. Based on the fitting of steady-state experimental data with oil, numerical simulations are conducted to fit to foam displacement experiments through our simulator by a gradient-optimization approach, assuming a 1D homogeneous model for the porous medium. Finally, based on computed tomography (CT) images, we construct a more-accurate 3D heterogeneous model to represent the core utilized in the experiment. This high-fidelity 3D model is used to reproduce the displacement experiments. The developed simulator shows good performance with an improved accuracy and flexibility.

4.2. COMPARISON WITH ANALYTICAL SOLUTIONS

In this part, the foam-oil flow problem is solved by three-phase fractional-flow theory [3], and we validate the numerical simulation results by comparison to analytical solutions. The saturations of injection conditions (J) and initial conditions (I) in all cases presented are summarized in Table 4.1. All saturations listed here are normalized by Eq. 4.1 with respect to the total movable saturations, as in Tang [3], except for the foam-oil parameters. Based on different J and I, all these cases are divided into four representative scenarios, with subscripts fm and nf denoting conditions inside or outside the foam region, respectively. Other parameters, such as relative-permeability and dry-out parameters, used in these cases are given in Table 4.2. In these cases, shear-thinning is neglected, to keep the same conditions as in the analytical solutions, and we assume that surfactant is already present in the water phase throughout the porous medium.

In Table 4.1, all Case 1 are the reference cases to show the displacement structure, while Case 2 of Scenarios 3 and 4 with a higher $fmoil$ are solved to illustrate foam stability at the foam-bank front and within an oil bank, respectively. These two cases allow foam injection but with different initial conditions. Normalized saturations are used in Fig. 4.2 through 4.8:

$$S_j = \frac{S_{j,a} - S_{j,r}}{1 - S_{wc} - S_{or} - S_{gr}}, \tag{4.1}$$

where $S_{j,a}$ and $S_{j,r}$ are the phase saturation and phase residual saturation, respectively. S_{or}, S_{wc}, and S_{gr} are the residual oil saturation, connate water saturation, and residual gas saturation.

Figs. 4.2(a) to 4.5(a) illustrate the composition path in ternary composition space for Case 1 in four Scenarios with $fmoil = 0.3$. In these four cases, the J and I are either inside or outside of the foam region. Due to the large value of $epdry$, F_6 in Eq. 2.29 switches from 0 ($S_w < fmdry$) to 1 ($S_w > fmdry$) abruptly around $fmdry$. Hence the mobility reduction factor holds almost constant for fixed oil saturation, though water and gas saturation vary. Fig. 4.2(a) and Fig. 4.3(a) describe the same injection condition, where S_w at J_{nf} is too low (too dry) to generate foam, while they have different initial conditions. S_o at I_{nf} is too high for foam to be stable, which causes the whole path to

Table 4.1: A summary of cases presented for comparison between numerical and analytical solutions

Scenarios		Injection conditions J = (S_w, S_o)	Initial conditions I = (S_w, S_o)	Foam model parameters
Scenario 1 (J_{nf} to I_{nf})	Case 1	J = (0.2, 0)	I = (0.1875, 0.8125)	$fmoil = 0.3$, $floil = 0.1$
Scenario 2 (J_{nf} to I_{fm})	Case 1	J = (0.2, 0)	I = (0.7750, 0.2250)	$fmoil = 0.3$, $floil = 0.1$
Scenario 3 (J_{fm} to I_{fm})	Case 1	J = (0.3125, 0)	I = (0.7750, 0.2250)	$fmoil = 0.3$, $floil = 0.1$
	Case 2	J = (0.3125, 0)	I = (0.7750, 0.2250)	$fmoil = 0.5$, $floil = 0.1$
Scenario 4 (J_{fm} to I_{nf})	Case 1	J = (0.3125, 0)	I = (0.1875, 0.8125)	$fmoil = 0.3$, $floil = 0.1$
	Case 2	J = (0.3125, 0)	I = (0.1875, 0.8125)	$fmoil = 0.5$, $floil = 0.1$

Table 4.2: Parameter values of Brooks-Corey relative-permeability model and foam model

Corey parameters and fluid viscosity						Foam parameters	
k^e_{rw}	k^e_{ro}	k^e_{rg}	n_w	n_o	n_g	fmmob	fmdry
1	1	1	2	2	2	2000	0.3
S_{wc}	S_{gr}	S_{or}	μ_w, cp	μ_o, cp	μ_g, cp	epdry	epoil
0.1	0	0.1	1	5	0.01	32000	3

bypass the foam region (suggesting there is no foam generation at all) in Fig. 4.2(a). Foam propagates some distance from the injection well in Fig. 4.3(a), although its strength is substantially reduced by oil. Fig. 4.4(a) and Fig. 4.5(a) describe the same situation as the previous two cases except for altering J_{nf} to J_{fm}. As shown in Fig. 4.4(a), where both J_{fm}, I_{fm} and the whole path are inside the foam region, foam is generated starting from the injection well, and water saturation is sufficient to maintain foam. Meanwhile, oil does not kill foam entirely anywhere along the displacement. Nevertheless, most injected gas escapes ahead of the foam bank, which propagates very slowly. Fig. 4.5(a) shows the case where J_{fm} is inside but I_{nf} outside of the foam region. The path crosses the foam boundary at $S_o = fmoil$ with a sharp inflection. Note that Case 1 in Scenario 2 presents a big challenge to our simulator: the simulator shows oscillations (Fig. A.1 in Appendix A.1). By adding a small capillary diffusion term, we eliminate the oscillations (see details in Appendix A.1).

Fig. 4.2(b) to Fig. 4.5(b) illustrate the saturation profile at the given pore volume injection (PVI) for Case 1 in four scenarios with $fmoil = 0.3$. Compared Fig. 4.2(b), without foam, to Fig. 4.5(b), gas is much more mobile than oil (and water), which causes extremely slow oil displacement. However, the slow-moving foam bank displaces nearly all the oil as shown in Fig. 4.5(b). Ahead of the foam region, it is waterflooding that re-

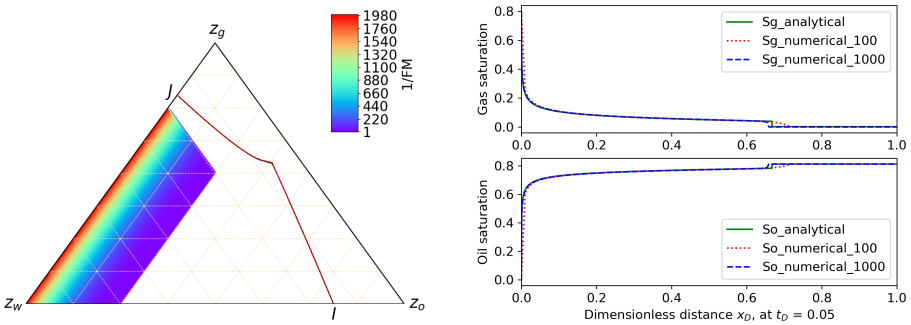

(a) (b)

Figure 4.2: (a) Composition path (fmoil=0.3) for Case 1 of Scenario 1 in ternary diagram. Both injection (J) and initial (I) conditions are outside the foam region. The three vertices represent the compositions of gas, oil and water, respectively. J and I are the injection and initial composition, respectively. The region with colors is the foam region, with color indicating the magnitude of mobility reduction; the rest is the no-foam region. The black solid line is the analytical solution, and the red dashed line is the OBL solution in the ternary diagram. (b) Gas-saturation and oil-saturation profiles as functions of dimensionless position x_D at time t_D = 0.05 PVI. 100 and 1000 in numerical solutions represent different grid resolution.

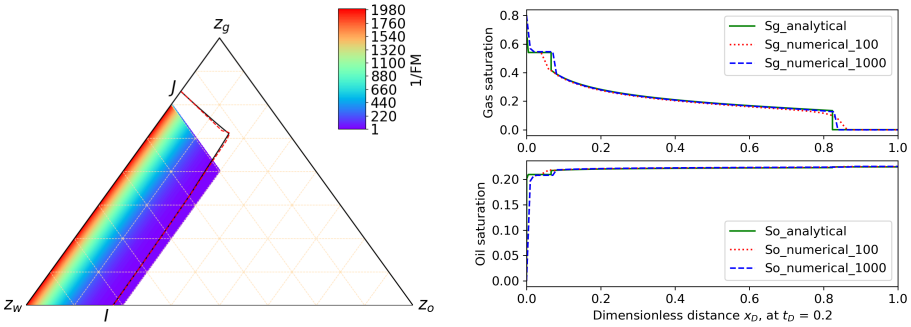

(a) (b)

Figure 4.3: (a) Composition path (fmoil=0.3) for Case 1 of Scenario 2 in ternary diagram. The injection condition (J) is outside but initial condition (I) is just inside the foam region. (b) Gas-saturation and oil-saturation profiles as functions of dimensionless position x_D at time t_D = 0.2 PVI. 100 and 1000 in numerical solutions represent different grid resolution.

duces S_o below $fmoil$ and allows a stable foam bank to form. In Fig. 4.3(b), gas hardly displaces oil but can displace water forward. In Fig. 4.4(b) the gas saturation is high near the entrance, suggesting that the foam displaces oil there, though very slowly.

For Case 2 in Scenarios 3 and 4, a larger $fmoil$ than that in Case 1, representing a surfactant formulation more tolerant to oil, is used to analyze the displacement. Fig. 4.6 and Fig. 4.7 demonstrate that the increase in $fmoil$ extends the foam region, reflecting foam more stable to oil. Fig. 4.6(a) illustrates that ahead of foam bank, an oil bank ($S_o > S_{o,i}$) is created; but S_o in the oil bank cannot exceed the upper limit $fmoil$ for stable foam. Therefore the oil within the oil bank reduces the foam strength but does not kill foam completely, which keeps the whole path inside the foam region. Fig. 4.7(a) exhibits

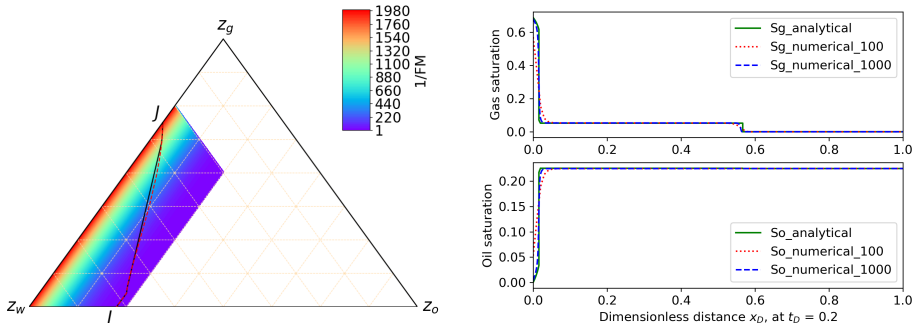

(a) (b)

Figure 4.4: (a) Composition path (fmoil=0.3) for Case 1 of Scenario 3 in ternary diagram. Both injection (J) and initial (I) conditions are inside the foam region. (b) Gas-saturation and oil-saturation profiles as functions of dimensionless position x_D at time t_D = 0.2 PVI. 100 and 1000 in numerical solutions represent different grid resolution.

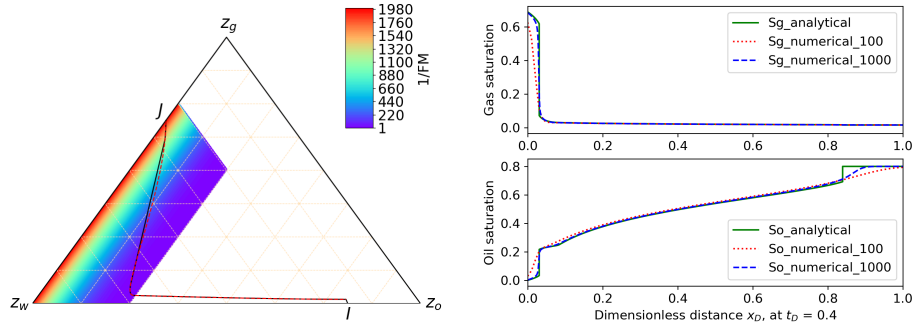

(a) (b)

Figure 4.5: (a) Composition path (fmoil=0.3) for Case 1 of Scenario 4 in ternary diagram. The injection condition (J) is inside but initial condition (I) is outside the foam region. (b) Gas-saturation and oil-saturation profiles as functions of dimensionless position x_D at time t_D = 0.4 PVI. 100 and 1000 in numerical solutions represent different grid resolution.

the composition path for I_{nf} outside of the foam region, where the stable foam is not allowed, although the foam region is extended by increasing $fmoil$.

Figs. 4.2(b) to 4.7(b) also illustrate the influence of grid size on the prediction by the OBL approach. In all cases, the difference in saturation profiles shows that using a finer grid, the numerical results are much closer to the analytical solution. The computational cost, however, increases. For instance, it takes 0.478s, with 3117 Newton iterations, for a coarse mesh (100 gridblocks) by the end of simulation in Case 2 of Scenario 3. When using a finer mesh (1000 gridblocks), it takes 5.41s with 4669 Newton iterations. As seen in Fig. 4.6(b), the simulation does not capture the shock at $x_D = 0.25 \sim 0.30$ well. The change of saturation along this shock is quite small: gas saturation jumps from 0.401 to 0.362, which requires greater resolution of both the OBL and grid to reproduce the shock more accurately (cf. Fig. 4.8(b) discussed below). Here we do not use very fine OBL and

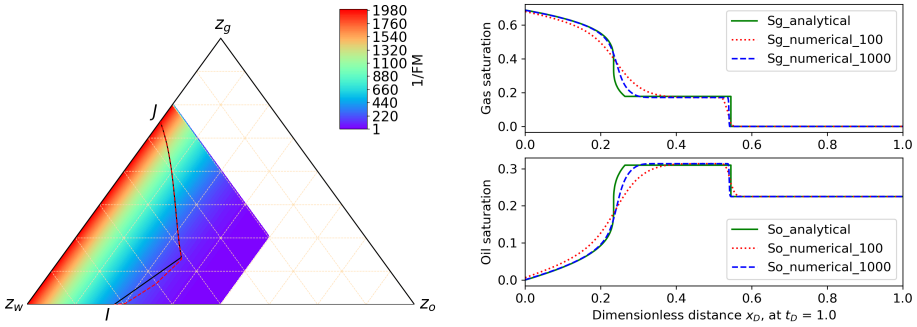

(a) (b)

Figure 4.6: (a) Composition path (fmoil=0.5) for Case 2 of Scenario 3 in ternary diagram, with injection (J) and initial (I) conditions both inside the foam region. In this case, fmoil is increased to 0.5. (b) Gas-saturation and oil-saturation profiles as functions of dimensionless position x_D at time t_D = 1.0 PVI. 100 and 1000 in numerical solutions represent different grid resolution.

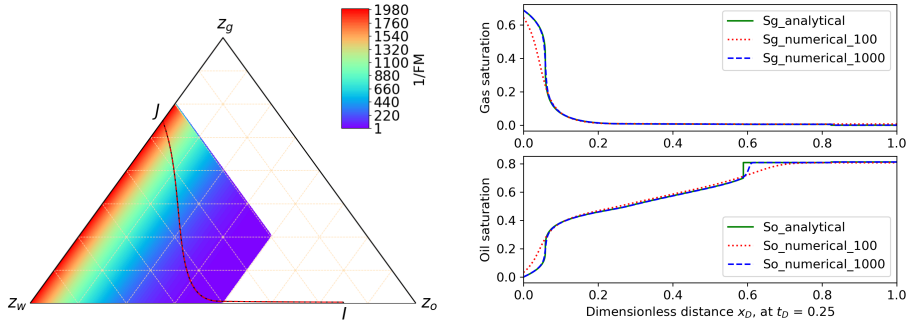

(a) (b)

Figure 4.7: (a) Composition path (fmoil=0.5) for Case 2 of Scenario 4 in ternary diagram, with injection condition (J) inside but initial condition (I) outside the foam region. In this case, fmoil is increased to 0.5. (b) Gas-saturation and oil-saturation profiles as functions of dimensionless position x_D at time t_D = 0.25 PVI. 100 and 1000 in numerical solutions represent different grid resolution.

grid resolutions for these comparisons, to save computational time. In our work, we do not present a detailed analysis of the displacement, i.e. the positions of the shocks and spreading waves, which have been demonstrated in Tang [3]. We mainly focus on the stability and accuracy of this new linearization technique. From these six cases, we can deduce that the OBL approach can capture the complex foam physical behavior and have overall good agreement with analytical solutions with acceptable accuracy.

4.3. EFFECT OF OBL RESOLUTION

To demonstrate the effect of OBL resolution, we show a set of simulations and compare the reference solution with results obtained at different resolutions based on Scenario 3, Case 2 (Fig. 4.6(b)). In Fig. 4.8(a), we present the spatial distribution of gas saturation

and oil saturation at time t_D = 1.0 pore volume injected (PVI) for simulations with different OBL resolutions (i.e., different distances between supporting points in the parameter space). From this figure we can see the difference between the analytical solution and the parametrized solutions with three different resolutions of parameter space. The finest resolution shown in the figure contains 150 values for each unknown and it obtains good agreement with the analytical solution with acceptable accuracy. However, when the resolution is 50, there is a big difference between the analytical solution and the numerical solution, which indicates that a finer OBL resolution is required in order to capture the highly nonlinear foam physics. The results with the two higher resolutions are close to each other, which demonstrates increasing OBL resolution can improve the numerical accuracy. However, the benefit is reduced at some point: if one resolution gives a good approximation, increasing resolution continuously cannot improve accuracy significantly. Moreover, a higher resolution increases the computational cost because more points need to be generated.

Fig. 4.8(a) shows that the two finer resolutions approach each other, but still smear out the shock at x_D = 0.23. This mismatch is caused by numerical dispersion. The first shock exits between the foam bank (behind of the shock) and oil bank (ahead of the shock). As mentioned above, the variation of saturation along this shock is quite small; thus a finer resolution for both OBL and grid is required to reproduce the shock more accurately. As shown in Fig. 4.6(b), a coarse grid gives a smooth change near the shock; however, the numerical solutions obtained from a finer mesh show better agreement with the analytical solutions, i.e., a sharp transition near the shock followed by a spreading wave. We can infer that with the decrease of grid-block size, the shock position can be reproduced within a small deviation [98]. A finer grid resolution can reduce the effect of numerical dispersion (Fig. 4.8(b)), but again, the computational cost also increases.

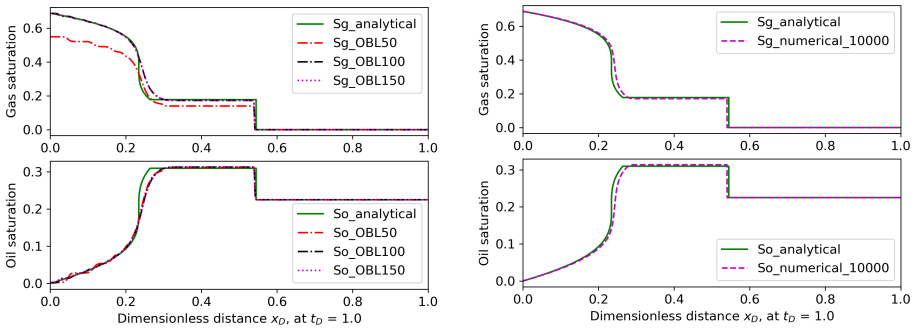

Figure 4.8: Comparison between gas saturation (upper) and oil saturation (lower) for different resolutions of parametrization in Case 2 of Scenario 3. (a) Different OBL resolutions with 1000 gridblocks; (b) Fine grid (10000) and fine OBL resolution (150).

4.4. FOAM PARAMETER-FITTING AND COREFLOOD SIMULATION

4.4.1. FOAM MODEL FIT TO STEADY-STATE DATA

Fitting foam scans to obtain foam parameters can be carried out using several techniques. One, proposed by Boejie and Rossen [14], can quickly provide initial estimation of foam parameters. By plotting a straight line and a convex curve passing through (f_g, ∇p) = (1, 0) and (0, 0) separately, the corresponding foam parameters can be estimated. However, it assumes that a large value of $epdry$, i.e., an abrupt transition between low and high quality regime. Zeng *et al.* [99] proposed an algorithm to estimate foam parameters in the absence of oil using linear regression and single-variable optimization. In order to obtain the water-saturation-dependent and shear-rate-dependent parameters, two kinds of experiments, i.e., foam-quality-scan with a fixed total superficial velocity and flow-rate-scan with a fixed foam quality experiments, are carried out. Zeng *et al.* [99] assume that in quality-scan experiments, the shear-thinning effect can be ignored because the total flow rate was held constant. This is not true in the STARS model [14]. The ability to fit oil-saturation dependence is also unclear. A third approach is based on a nonlinear least-squares minimization, which can simultaneously compute all seven parameters by minimizing the sum of squared errors [100]. The same foam-scan data can be fitted roughly equally well by using Boejie and Rossen's approach and a nonlinear least-squares minimization method [100]. In our work, the latter approach is implemented to obtain the foam parameters by fitting the experimental data in the presence of oil.

Tang *et al.* [89] carried out steady-state foam experiments in the presence of oil. In their experiments, the surfactant concentration is 0.5wt%, which is above the critical concentration. Oil was co-injected with foam at a fixed ratio of oil to water superficial velocity. Unfortunately, the oil saturation was not measured in these experiments. We assume that Corey relative-permeability functions can be applied to three phase flow; then the oil saturation is obtained indirectly through flow and pressure data using Darcy's law. In this work, we fit only the experimental data with hexadecane (C_{16}), which is benign to foam stability, using the wet-foam algorithm, where oil changes the mobility of full-strength foam in the low-quality regime. The foam simulation model includes the following parameters: $fmmob$, $fmdry$, $epdry$, $fmcap$, $epcap$, $fmoil$, $floil$, $epoil$, while the fluid and transport properties used in the parameter-fitting could be found in Tang *et al.* [89]. The detailed procedure is described as below:

Step 1. Draw ∇p contours as a function of U_w and U_g. One might need to screen the data and smooth the ∇p contours to efficiently fit foam parameters. For fixed ∇p, the fitted contour comprises a vertical line (the high-quality regime) and a horizontal line (the low-quality regime), as shown in Fig. 4.10.

Step 2. Plot a single foam-quality scan. Pick one fixed total superficial velocity (U_t); then one can determine ∇p along this scan by making a diagonal line, the same as Fig. 4.1.

Step 3. Determine the oil saturation with respect to the corresponding water saturation. Without the effect of gravity and capillary pressure, Darcy's law is applied to the water phase to obtain the water saturation. Water relative permeability is thus obtained; then oil relative permeability can also be obtained due to the fixed ratio of oil and water superficial velocity. Using Corey relative permeability, one can calculate the oil satura-

tion.

Step 4. Define the objective function. Once water and oil phase saturations are known, one can define the objective function. In our project, the objective function is defined as the difference between experimental data and model data:

$$\min f = \sum_{i}^{n} (\mu_{app_{exp}} - \mu_{app_{model}}), \tag{4.2}$$

$$\mu_{app_{model}} = \frac{1}{k_{rw}(S_w)/\mu_w + k_{rg}(S_w) * FM(S_w, S_o, \nabla p)/\mu_g + k_{ro}(S_w)/\mu_o}. \tag{4.3}$$

Step 5. Apply a nonlinear least-square minimization approach to find the optimal solution in the given range by minimizing the sum of squared errors.

Fig. 4.9 and Table 4.3 show the final data fit for the foam-quality-scan experiment. In the high-quality regime, the model shows good agreement with experimental data. In our model, the foam behaves as a Newtonian fluid, and oil does not change the foam strength in the high-quality regime [14, 101]. Therefore, and because a large value of $epdry$ fits the data, the fit gives a straight line in this regime. In the low-quality regime, although the effects of oil saturation, water saturation and shear-thinning rheology on foam are taken into account, our model does not show perfect agreement with the experimental data, especially where foam quality approaches the transition between regimes.

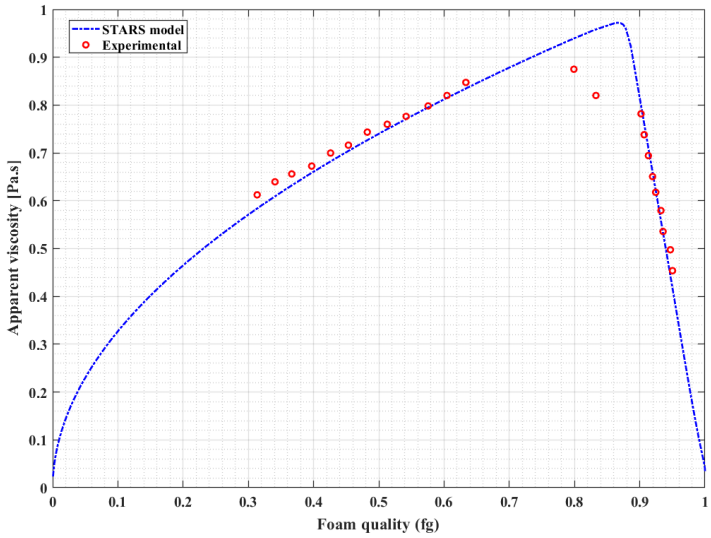

Figure 4.9: The relationship between apparent viscosity and foam-quality (f_g) at fixed U_t = 3 ft/D in a Bentheimer sandstone core, from Tang *et al.* [89].

Once these foam parameters are obtained, the pressure-gradient / velocity contours are constructed. Fig. 4.10 compares these contours to the experimental data. The model fit provides a good match with the experimental data and the implemented wet-foam model can predict the foam behavior in high- and low-quality regimes. However, in the

Table 4.3: STARS model parameters fitted to foam-scan experiment

Foam parameters	values	Foam parameters	values
fmmob	50000	epcap	1.321
fmdry	0.215	fmoil	0.823
epdry	19950	floil	0.295
fmcap	0.0001	epoil	3.827

low-quality regime, this model cannot capture the upward-tilting ∇p contours, therefore ∇p in this regime is greatly overestimated at high water superficial velocity [89]. Pressure gradient increases with increasing water velocity in the low-quality regime in the experiments (see red contour in Fig. 4.10) [102]: the pressure gradient is not independent of the water velocity in the low-quality regime. In order to address this issue, this foam model should be improved to represent this behavior in the low-quality regime. This lies beyond the scope of this work.

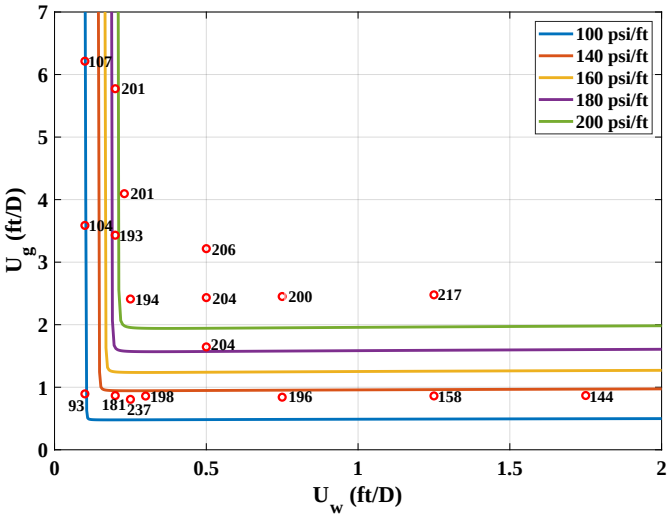

Figure 4.10: Model fit by use of our method to the data of Tang *et al.* [89]. The red circles with numerical values denote experimental data.

4.4.2. SIMULATION OF CT FOAM COREFLOOD WITH OIL

In this section, we model a CT coreflood study of foam displacement with C_{16} [3]. Our purpose is to understand the transient dynamics of foam using the OBL approach based on the experimental data. We also want to check whether the foam parameters obtained at steady-state can be applied to a foam-displacement process. The core sample in the experiment is Bentheimer sandstone with length 40 cm, diameter 4.0 cm, porosity 0.22, and absolute permeability 2820 mD. The core is initially filled with water and oil (S_{oi} = 0.46 and S_{wi} = 0.54, respectively) and pre-generated foam is injected into the core with

f_g = 70%. In the simulation, a simple 1D domain consisting of 100 grid cells is used to represent the core. A OBL resolution of 500 is chosen in this case which is sufficient to represent underlying nonlinear physics. The foam parameters are taken from the steady-state experiments, as shown in Table 4.3.

Tang *et al.* [89] did not measure the foam-free relative-permeability functions for each phase in their CT coreflood experiments, which adds some uncertainties to the simulation. In order to match the experiment data accurately, we adopted a gradient-optimization technique to regress the relative-permeability parameters based on the Corey model. The details and results are shown in Appendix A.2. Implementing these new parameter values (i.e., parameters of Corey relative permeability), we run the simulation for a period of experiment. Fig. 4.11 shows the phase-saturation profiles at different PVI. The oil saturation in the oil bank in the experiment is around 0.8. From the steady-state foam modeling, the critical oil saturation $fmoil$ is 0.827. A stable oil bank forms, with oil saturation below $fmoil$ in the simulation, as in the experiment. Foam in forward propagation creates an oil bank with $S_o \sim 0.8$ at the displacement front in the core-flood experiment (Fig. 4.11). S_g is roughly zero ahead of the foam front, as seen from gas-saturation profiles. This suggests that most gas is held within the foam bank.

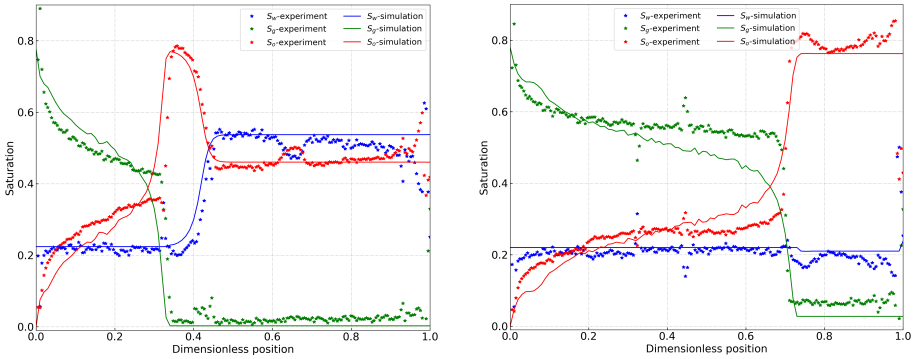

(a) 0.36 PV (b) 0.82 PV

Figure 4.11: Phase saturation profiles vs. dimensionless position at different injected pore volumes.

These results show that the simulation with OBL approach can be used to fit model parameters to a foam displacement coreflood data. Notice that with the relative permeabilities adjusted to fit the displacement coreflood data and the foam-model parameters fixed, the model no longer fits the steady-state data. The model fit overestimates the mobility in the low-quality regime by about 15%. Moreover, the new relative permeability parameters place S_{wc} (0.197) so close to $fmdry$ (0.215) that the high-quality regime virtually disappears from the fit. It is possible that fitting both steady-state and coreflood displacement data simultaneously could obtain a satisfactory fit to both. Or, it is possible that the model itself cannot represent the full physics of foam behavior. This issue remains for future investigation. However, the proposed approach helps in the representation of the physical phenomena identified during our foam experiments in realistic 3D numerical simulation shown next.

4.4.3. 3D CT COREFLOOD

To demonstrate the accuracy of the fitting model, we build a 3D heterogeneous simulation grid based on the CT images. The following correlation is used to determine the porosity in each pixel [103]:

$$\phi = \frac{CT_{brine} - CT_{air}}{CT_w - CT_a} \tag{4.4}$$

where, CT_{brine} is the CT attenuation of fully brine saturated core; CT_{air} is the CT attenuation of dry core; and CT_w and CT_a are the CT attenuation of water and air, respectively. Such a correlation is applied to each CT slice (e.g., the gray circular area in Fig. 4.12(a)). Then the porosity of each triangular grid block can be evaluated to obtain the porosity distribution, as shown in Fig. 4.12(b) and Fig. 4.12(c). On each slice, an unstructured map with 1080 elements is used to represent the porosity distribution, with an average cell area of 1.16 mm^2. From the CT scan, one can see that the variation of the porosity in the Bentheimer core is relatively small.

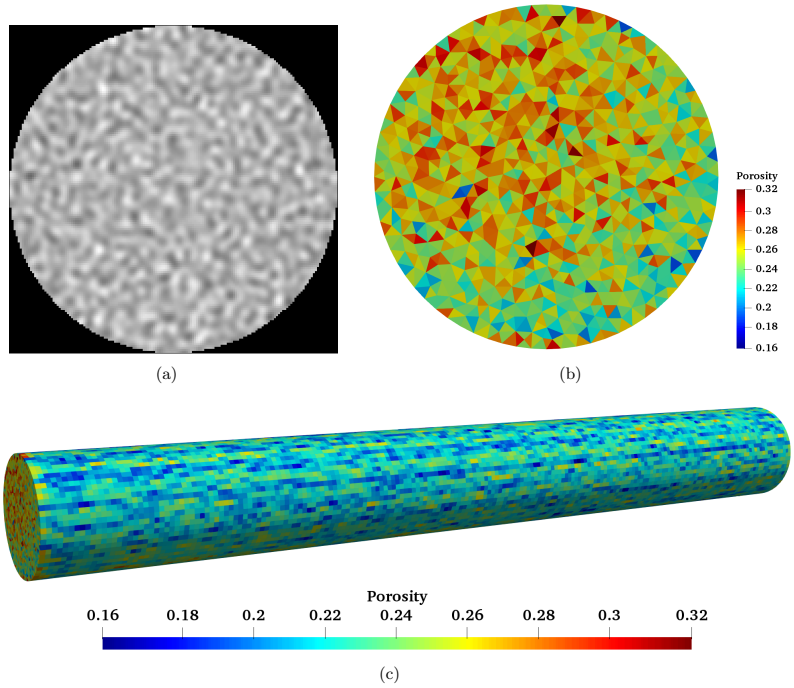

Figure 4.12: Porosity profile of Sandstone example. (a) CT image; (b) Porosity profile; (c) Porosity distribution along the core

Fig. 4.13 shows the frequency histogram of the porosity data extracted from the CT images. For this Bentheimer sandstone, the average porosity is around 0.23, which is consistent with the values in the literature where the porosity of Bentheimer sandstone is reported [89, 100, 104]. Then based on the Kozeny–Carman equation [105], the corre-

sponding permeability is:

$$k = \alpha \frac{\phi^3 D_p^2}{(1-\phi)^2} \tag{4.5}$$

where k is the absolute permeability, mD; D_p is average diameter of sand grains, mm; ϕ is the porosity of the core plug; α is the proportionality and unity factor, mD/mm^2. Due to the limited experimental data, we assume that the permeability has a same distribution as the porosity, i.e., the mean permeability shares the same frequency as the mean porosity. With this assumption, once we know the average porosity and average permeability, a combination of α and D_p^2 can be obtained to calculate permeability distribution based on the porosity distribution from CT image.

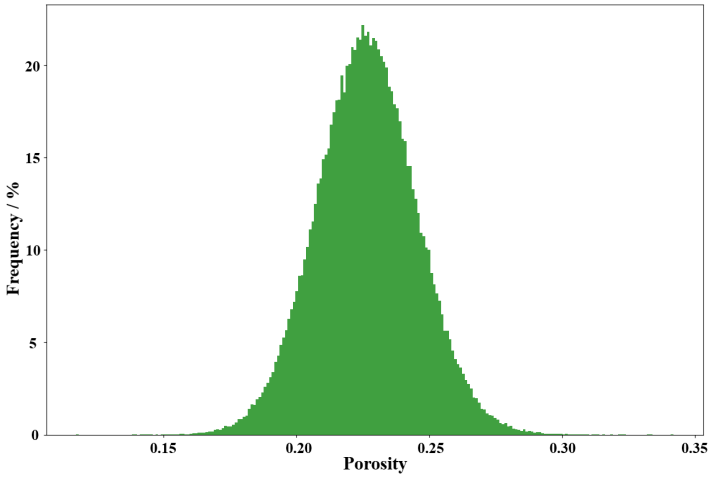

Figure 4.13: Frequency histogram of the porosity data.

Once the porosity and permeability data are obtained, we run the model for 0.36 PV injection using the same parameters as in the previous case (apart from allowing for heterogeneous porosity and permeability). In this work, we mainly focus on whether the OBL approach can capture the oil bank seen in the experiment which cannot be accurately predicted by a conventional physics based on the steady-state model. The distribution of phase saturations is shown in Fig. 4.14. Fig. 4.14(a) displays the gas-saturation distribution along the vertical plane on the central axis of the core. From the inlet to the gas front, a foam region is formed that displaces an oil bank ahead of it. However, the foam near the oil bank is weakened due to the increasing oil saturation. Ahead of the gas front, an oil bank with a higher oil saturation is created, which further reduces the foam strength (Fig. 4.14(b)). Our 3D-simulation results show good overall agreement with CT coreflood results in terms of saturation profiles (Fig. 4.15). It is obvious that 3D simulation results are more accurately representing the displacement regimes observed in the experiment in comparison to 1D simulation.

Compared to the CT image in Fig. 4.14, there are still some small differences between numerical results and experimental results. The first is that oil saturation is slightly

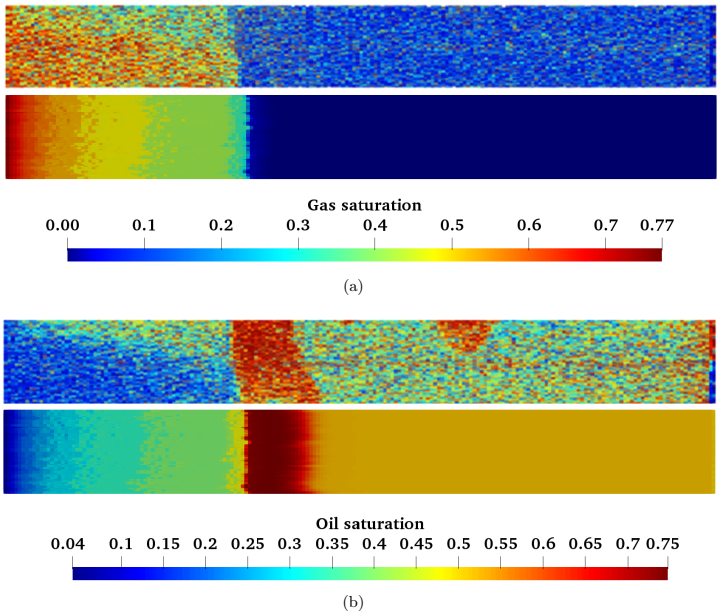

Figure 4.14: Gas saturation and oil saturation profiles at t_D = 0.36 PVI along the vertical plane at the central axis of the core. The top figure in (a) and (b) is the CT image, and the bottom is the simulation result.

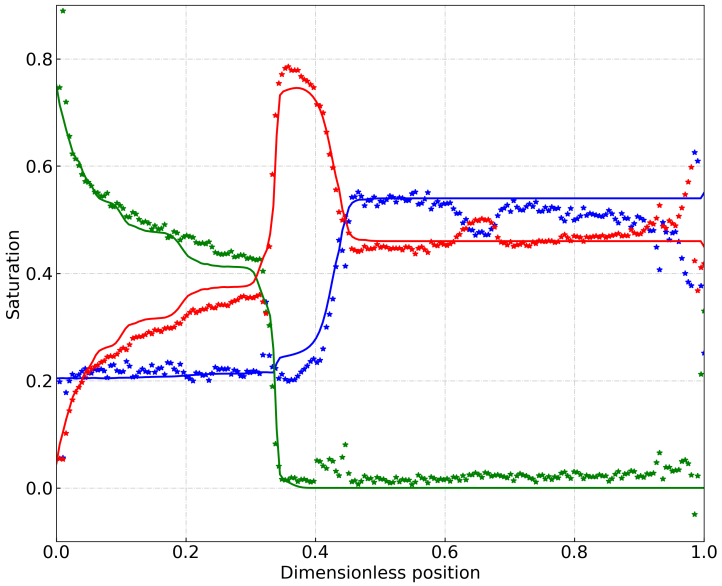

Figure 4.15: Phase-saturation at t_D = 0.36 PVI. The average saturation of each slice along the core is plotted, with comparison to experimental data.

greater at the top of the core behind the oil bank in the CT image. Although gravity is included in our simulation, this phenomenon is not fully resolved in the 3D model. The second is that there are some locations where oil saturation is slightly higher in the experiment in comparison to our simulation. Some further work is needed to explore the reasons causing these differences. However, the 3D coreflood simulation provides us with new insights to investigate the behavior of foam displacement compared to the 1D model:

(1) The heterogeneity of the core can be taken into account using the 3D simulation grid. Although the porosity of Bentheimer sandstone used in this experiment shows a small variability, this heterogeneous grid is more realistic. Then more physics can be included, such as capillary heterogeneity and gravity.

(2) Heterogeneity is an important factor which affects the foam strength [16, 100]. The 3D heterogeneous core can be used to investigate the effect of small scale heterogeneity on foam EOR processes.

Our future work will focus on the development of the data-driven approach and include more physics to represent the behavior accurately. We also want to extend this approach to general-purpose reservoir-simulation problems, for instance, a field-scale pilot. In addition, we will develop an extension of this approach to systems with gravity- and capillary-dominated flow, which have a great impact on foam behavior. These systems introduce many nonlinearities to challenge Newton-based nonlinear solvers. A more-robust nonlinear strategy is required to solve these models with highly nonlinear physics efficiently and accurately.

4.5. CONCLUSIONS

In this chapter, we extended a new linearization technique, Operator-Based Linearization, to foam-related simulation. The benefits of this nonlinear strategy is that the potential problem introduced by the rapid changes of property gradient in the presence of foam with oil can be resolved successfully with greater performance.

We compare our linearization approach to analytical solutions based on fractional-flow theory. The OBL approach shows good agreement with the analytical solutions except in the case where the initial oil saturation is close to $fmmoil$. In order to avoid oscillations in saturation profiles, a capillary diffusion term, which eliminates the oscillations, is introduced. Notice that this correction is only required for near numerical dispersion-free simulations performed for an accurate representation of the analytic solution. The nonlinear least-squares minimization approach can give a good match with the foam-scan data, but still cannot capture the upward-tilting ∇p contours in the low-quality regime due to a limitation of the current foam model.

Given the foam parameters obtained from steady-state experiments, it is still a challenge to match the experimental data. The gradient-optimization technique improves the accuracy of simulation significantly by optimizing the relative-permeability data. But based on the fitted parameters, the 1D simulation does not show a perfect match with experimental results due to the limitation of the steady-state foam model. The 3D simulation results improve the accuracy but still missing few important features. It may be important to explore a new model, for instance, the population-balance model, to accurately represent the dynamic behavior of foam in porous media.

We introduce the OBL approach here and illustrate its accuracy and usefulness in simulations of laboratory-scale experiments. There are additional challenges in the scale-up of simulations for reservoir applications, among them representing the range of conditions (temperature, salinity, surfactant concentration, formation properties) that would be encountered in a reservoir application, surfactant retention in the formation, modeling the effects of heterogeneities below the grid-block scale, the effects of layer boundaries on foam properties [106], and near-well mechanisms affecting foam injectivity [107]. Incorporating these factors into field-scale simulation remains a research priority.

5

MITIGATION OF GRAVITY SEGREGATION BY FOAM

Summary

Foam can improve the injection profile in gas-injection processes by mitigating gravity segregation, especially in heterogeneous reservoirs. To assess CO_2 foam transport in enhanced oil recovery (EOR) and for CO_2 storage processes in heterogeneous reservoirs, an accurate prediction of foam behaviour is essential. This chapter presents simulation results on using an implicit-texture (IT) foam model with two flow regimes to investigate the effect of heterogeneity on gravity segregation. We first validate the numerical accuracy of the simulation, including water-gas co-injection and pre-generated foam injection, with the OBL approach by comparing segregation length to analytical solutions. Next, the foam-model parameters are fit to foam-quality scan data for four sandstone formations ranging in permeability by an order of magnitude, using a least-squares optimization approach. We then construct several hypothetical reservoir models containing two communicating layers with different permeabilities and thickness ratios to examine foam's effect on gravity segregation.

The material presented in this chapter has been published in IOR conference, 2021 [51].

5.1. INTRODUCTION

Gas injection can displace oil where gas sweeps [84]. The gas phase (commonly N_2, CO_2, produced hydrocarbon gas, or a combination of these) is injected into reservoirs either as a miscible or immiscible displacement agent. However, due to reservoir heterogeneity, gravity override, and viscous instability, gas injection typically suffers from poor sweep efficiency. Foam, an agglomeration of gas bubbles separated from each other by thin liquid films, can overcome these problems and thereby improve the sweep efficiency in gas-injection EOR processes [4–6] or enlarge the storage space for trapping of CO_2 in aquifers [7–9].

Stone [108] presented a steady-state analytical model for gas sweep in uniform co-injection of water and gas into homogeneous, horizontal reservoirs. This model can also be applied to water-alternating-gas (WAG) injection as long as injection cycles are short enough to guarantee that all slugs can mix thoroughly near the well. Stone [108] assumed that at steady state three regions of uniform saturation can be distinguished in a reservoir, with sharp boundaries between them: an override zone with only gas flowing, an underride zone with only water flowing, and a mixed zone adjacent to the wellbore with both gas and water flowing (Fig. 5.1).

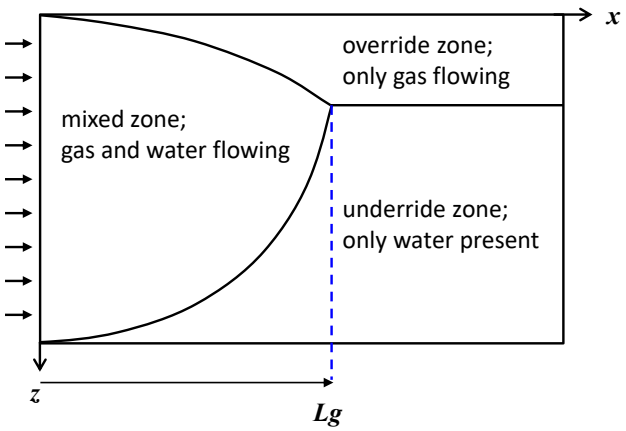

Figure 5.1: Schematic of three uniform zones at steady state in the gravity-segregation model of Stone [108] and Jenkins [109] for continuous co-injection of water and gas. L_g is the ultimate distance where gas and water completely segregate.

The distance between the injection well and the point where the mixed zone disappears is called the segregation length (L_g). Stone [108] and Jenkins [109] derived equations for L_g (in a rectangular reservoir) or R_g (in a cylindrical reservoir):

$$L_g = \frac{Q_t}{k_z(\rho_w - \rho_g)gW\lambda_{rt}^m} \tag{5.1}$$

$$R_g = \sqrt{\frac{Q_t}{\pi k_z(\rho_w - \rho_g)g\lambda_{rt}^m}} \tag{5.2}$$

where Q_t is the total volumetric injection rate of gas and water, k_z vertical permeability, ρ_w and ρ_g densities of water and gas respectively, g the gravitational acceleration, W the thickness of the rectangular reservoir perpendicular to flow, and λ_{rt}^m the total relative mobility in the mixed zone. The volumetric sweep increases with increasing L_g or R_g, which depend on the total injection rate Q_t.

Shi and Rossen [110] declared that the only way to control gravity segregation is to increase injection-well pressure when steady injection is performed into a given reservoir. They also discussed the implications of this model for field application of foams. Rossen and Van Duijn [111] proved that Eqs. 5.1 and 5.2 are rigorously correct as long as the standard assumptions of fractional-flow theory are applied. Rossen and Shen [112] derived the relation between injection-well pressure and segregation length. Rossen and Stolwijk [113] found that these two equations are reasonably accurate for heterogeneous reservoirs with small degrees of heterogeneity, such as mildly heterogeneous layered or checkerboard reservoirs, if one adjusts the vertical permeability to account for the heterogeneity. However, when heterogeneity is more severe, L_g is not a good measure of sweep efficiency. Rossen *et al.* [114] showed that this model can be extended to foam flow as long as injection is uniform along the wells, despite the complexity of foam behaviour.

Stone's model is extended to dipping reservoirs based on numerical simulations [115, 116] or derivation of an analytical model where some assumptions are not rigorously accurate [117–119]. As per our knowledge, until now, there have been few studies to investigate the gravity segregation in the foam-EOR process, especially considering reservoir heterogeneity. In this chapter, we investigate the effect of reservoir heterogeneity on gravity segregation in foam-EOR processes. The implicit-texture (IT) 'STARS' model [65] is used. For simplicity, we assume that oil is absent in our model and surfactant is already present in the water phase throughout the porous medium. The foam model we use is shown in Section 2.4.

In this chapter, we first validate the simulation by comparing numerical results with the analytical solutions mentioned above. Then, we investigate the effect of permeability and reservoir heterogeneity on gravity segregation. We end the chapter up with a discussion and summary of main conclusions.

5.2. COMPARISON WITH THE ANALYTICAL MODEL

5.2.1. GAS-WATER COINJECTION AND FOAM INJECTION

We first compare numerical results with the analytical model for a horizontal homogeneous reservoir with different injected water fractions in the presence and absence of foam. In this study, a 2D horizontal rectangular grid is constructed and the size of a grid block is 1×1×1 m. The parameter values, such as permeability and foam parameters, are listed in Table 5.1. For a better resolution, the permeability of the cases with foam injection is 10 times higher than that without foam. The parameters of the Corey relative-permeability model is shown in Appendix A.3. The top and bottom surfaces of the reservoir are no-flow boundaries. The injection wells (with fixed total injection rate of 1.5 m^3/day at reservoir condition) and one production well (fixed bottom-hole pressure at 138 bar) are located at the left boundary and right boundary, respectively, perfo-

rating all layers in the vertical direction.

In this study, we run simulations with separate injection wells in each grid block with a fixed injection rate and f_w in each well to ensure that f_w^J is uniform along the entire length of the reservoir. Such a small injection rate is chosen so that segregation would occur within the reservoir volume. We assume the reservoir is isotropic; the horizontal permeability is equal to the vertical permeability. Capillary pressure is neglected in this study. From Stone [108] and Jenkins [109], one pore volume (PV) of gas should be sufficient to reach steady state. In our simulations, 2 PV of gas are injected to ensure that the injected gas and water can segregate completely. We test eight cases with different injected water fractions, of 5%, 10%, 15%, 20%, 25%, 30%, 35% and 40%.

Table 5.1: Parameter settings used in 2D horizontal models

	Reservoir dimension	Permeability, mD	Porosity	Foam parameters		
				$fmmob$	$fmdry$	$epdry$
No foam	100×1×30	100	0.2	-	-	-
Foam	400×1×30	1000		3400	0.13	10000

5

Fig. 5.2 shows the water-saturation profile without and with foam at steady state for uniform co-injection of gas and water (f_w = 25%) along the entire vertical interval. There are a mixed zone of nearly homogeneous saturation, an underride zone of uniform saturation (S_w = 1), and a steady-state override zone with water at its residual saturation. There are some visible differences if foam is injected. First, in the mixed zone, the water saturation with foam injection is much lower than that without foam, in order to accommodate the same fractional-flow of water. Foam can significantly reduce gas mobility; the reduction of gas mobility by foam causes the injection pressure to increase if the injection rate is fixed.

After steady state, the foam-injection pressure (289 bar) is around 2.0 times higher than that without foam (146 bar), even with 10 times greater absolute permeability. The higher apparent viscosity of foam could increase injection pressure beyond that allowed by surface facilities or above formation fracturing pressure [120–122]. The second difference is the segregation length. With the same injection rates, when foam is injected, the segregation length increases by over two orders of magnitude compared to that without foam. Eq. 5.1 predicts that the reduction of the total mobility in the mixed zone with foam mitigates the effect of gravity segregation at the price of increased injection pressure.

Fig. 5.3 compares the variation between the analytical solutions and numerical solutions of the segregation length with different injected water fractions in the absence and presence of foam. In Fig. 5.3(a), we show the ultimate segregation length with and without the transition zone. As predicted by Stone's model, water saturation is uniform at a saturation $S_{w,mix}$ in the mixed zone. To minimize the effect of numerical dispersion, we distinguish the mixed zone where the water saturation is equal to or smaller than ($S_{w,mix}$ + 0.001). Numerical dispersion plays a significant role in the segregation length for the case without foam, as discussed below.

Fig. 5.3(b) shows that foam quality significantly affects the segregation length by modifying the total relative mobility in the mixed zone in Eq. (5.1). In the high-quality regime, the segregation length increases with decreasing foam-quality; on the contrary,

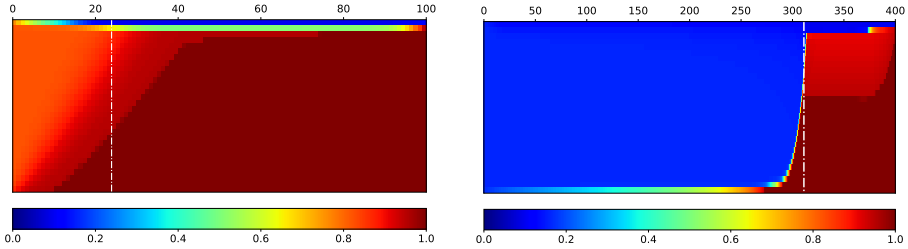

(a) No foam (b) Foam injection

Figure 5.2: Water saturation profile (f_w = 25%) at steady state. The white dashed line is the segregation point predicted by Eq. 5.1. In both cases, there are transition zones where water saturation is lower than that at the initial condition.

it decreases when foam-quality decreases in the low-quality regime. The segregation length approaches a maximum value in the transition between the two regimes, where the foam apparent viscosity is highest, i.e., lowest total relative mobility. The distance of complete gravity segregation agrees with the analytical solutions quite well. Excluding the effect of numerical dispersion, our numerical model shows good agreement with analytical solutions predicted by Stone [108] and Jenkins [109].

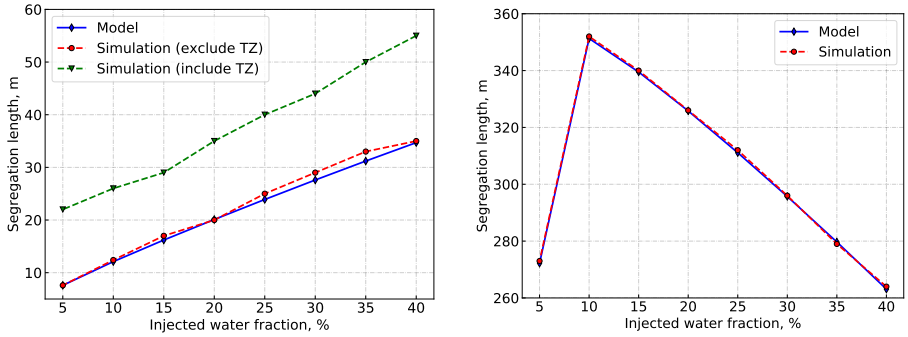

(a) No foam (b) Foam injection

Figure 5.3: Comparison between analytical model and simulation results. (a) no foam; (b) foam. 'TZ' is an abbreviation of 'Transition Zone'.

5.2.2. EFFECT OF PERMEABILITY ON GRAVITY SEGREGATION WITH FOAM INJECTION

In this section, we investigate the effect of permeability on gravity segregation in the presence of foam using the parameters in Table A.2. The dimension of the domain is 300 × 1 × 30 m with gridblock size of 1 m × 1 m × 1 m. Due to the mobility reduction in the presence of foam, the magnitude of the segregation length predicted by Eq. (5.1) is of order 10^3 m for all four permeabilities if the total injection rate along the entire vertical

interval is 1.5 m^3/day, with f_w = 25%. In practice, the distance between an injector and a producer is usually shorter while an effective thickness is larger. Therefore, in this and following simulation results (except where noted), the injection rate is reduced to 0.12 m^3/day, with f_w = 25%, for better resolution of foam behaviour in a reasonable distance. In all cases, 2.67 PV (corresponding to 2.0 PV of gas) injection is sufficient to achieve steady state.

Under the same injection conditions, the segregation length in different formations is different, as shown in Fig. 5.4. In the higher-permeability formation with K = 551.5 mD, gas and water separate from each other in a relatively short distance; the segregation length is longer in the lowest-permeability case, approximately 255 m. With a fixed total injection rate, the segregation length increases with decreasing permeability, as predicted by Eq. 5.1. Because apparent viscosity increases with increasing permeability (Fig. A.3), the increase in segregation length is relatively small. Water saturation in the mixed zone is close to the limiting water saturation ($fmdry$ in the IT model) in all cases.

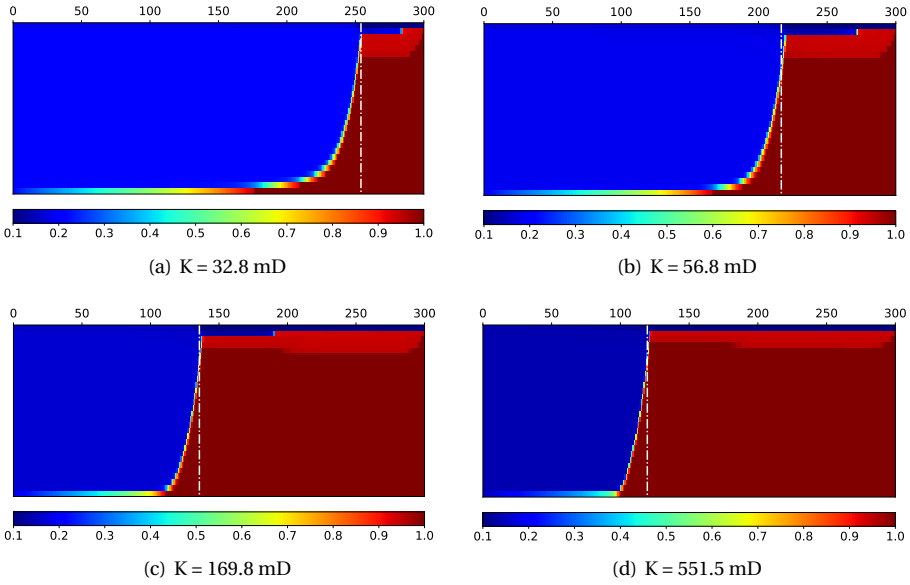

(a) K = 32.8 mD (b) K = 56.8 mD

(c) K = 169.8 mD (d) K = 551.5 mD

Figure 5.4: Water-saturation profiles at steady state in formations with different permeabilities. The white dashed line is the segregation point predicted by Eq. 5.1.

Fig. 5.5 illustrates the relationship between the segregation length, apparent viscosity and permeability. The foam is stronger (higher apparent viscosity) in the higher-permeability formation where the limiting capillary pressure is lower, as shown in Fig. 5.5(a). The segregation length, however, decreases with the increase of permeability. From Eq. 5.1, the segregation length depends on the combination of vertical permeability and total relative mobility (i.e., apparent viscosity) in the mixed zone if the total injection rate is fixed in a given grid. Fig. 5.5(b) shows the variation of segregation length with

the permeability and apparent viscosity in the mixed zone. The segregation length decreases with the increase in $(K/\mu_{app}) = (K_z\lambda_{rt})$. Under the same injection condition, the low-permeability formation gives a longer segregation length, as predicted by Eq. 5.1. In our study, we only have these four sandstone formations available with limited physics. More studies should be carried out to investigate the effect of permeability on foam strength and segregation length.

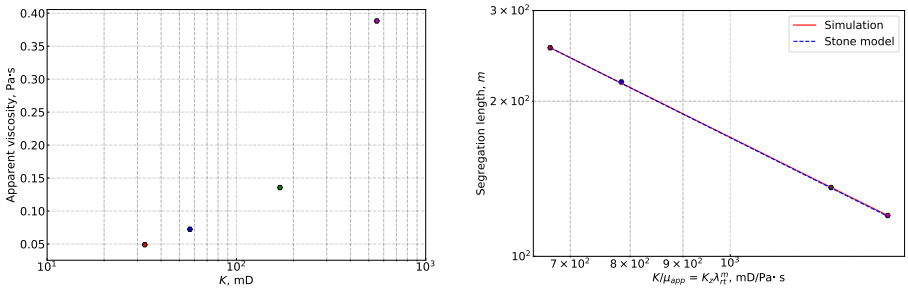

(a) μ_{app} vs. K

(b) L_g vs. K/μ_{app} (= K$_z\lambda_{rt}$)

Figure 5.5: The relationship between segregation length (or apparent viscosity) and permeability. (a) The absolute permeability is plotted in the logarithmic space; (b) In log-log space, the segregation length is a linear function of $(K/\mu_{app}) = (K_z\lambda_{rt})$: the simulation results agree with Stone's prediction.

Rossen *et al.* [114] derived a relation between injection pressure and gravity segregation in cylindrical flow. We extend this relation to a rectangular coordinate system (see details in Appendix. A.4). The upper bound of the relation is

$$p(r_w) - p(L_g) = \frac{L_g^2 k_z(\rho_w - \rho_g)gW}{k_h A} \tag{5.3}$$

and the lower bound is

$$p(r_w) - p(L_g) = \frac{L_g^2 k_z(\rho_w - \rho_g)gW}{2k_h A} \tag{5.4}$$

where $p(r_w)$ and $p(L_g)$ are the pressure at the wellbore and at the segregation point. Neither Q nor λ_{rt}^m is included in Eqs. 5.3 or 5.4; i.e., the segregation length is controlled by the injection-well pressure, consistent with the findings in Rossen *et al.* [114]. Meanwhile, the pressure difference of the upper bound between the injection point and segregation point is twice that of the lower bound. Table 5.2 compares the injection pressure in the model and simulations. As shown in Fig. 5.4, the shape of the mixed zone is close to the case where the height of the mixed zone decreases negligibly with increasing distance from the injection well. The injection pressure in simulation, however, approaches the lower bound where the height of the mixed zone shrinks nearly proportionately to total flow rate (Eq. 5.4). It indicates that this approximation based on the shape of the mixed zone may cause deviations in predicting the injection pressure in this study. An analytic model to accurately describe the relationship between the injection pressure and the shape of the mixed zone is still required. To reach the same segregation point for stronger foam, the required injection pressure is also higher.

Table 5.2: Comparison of injection pressure in different models

Case	Model (Lower), bar	Model (Upper), bar	Simulation, bar
K = 32.8 mD	224.0	311.9	233.4
K = 56.8 mD	199.9	263.8	207.4
K = 169.8 mD	161.1	186.2	165.5
K = 551.5 mD	155.5	175.0	158.9

5.3. EFFECT OF NUMERICAL DISPERSION

Both cases show a dispersed zone along the boundaries between zones, and this zone is extended a few grid blocks in the simulations (Fig. 5.2 and Fig. 5.4) in part due to the numerical dispersion and in part due to the lower gas mobility during the period of two-phase transient displacement [113, 114, 116, 123]. These transition zones are not included in Stone's model because it is a static model designed to depict a steady state. Stone notes that numerical dispersion plays an important role and is difficult to control in the course of simulation of these processes. In this section, the effect of numerical dispersion on gravity segregation is discussed in terms of grid size for the case where gas and water are co-injected with f_g = 75% and only gas is injected with f_g = 100% (i.e., in the override zone). We ignore the influence of time-step and OBL resolution. Then we quantitatively evaluate the differences between the analytical and numerical solutions.

At first, we use a simple 1D model to investigate the effect of numerical dispersion in the presence and absence of foam with different f_g by comparing to the analytical solution using fractional-flow theory [15]. The corresponding fractional-flow curves and total-relative-mobility curves for gas-water and foam system are shown in Fig. 5.6. We simulate a 1D homogeneous porous medium with 1000 grid blocks (grid size is 0.1m). In all tests, the total injection rate (0.05 m^3/day) is fixed with a value of f_g of 75% and 100%, respectively.

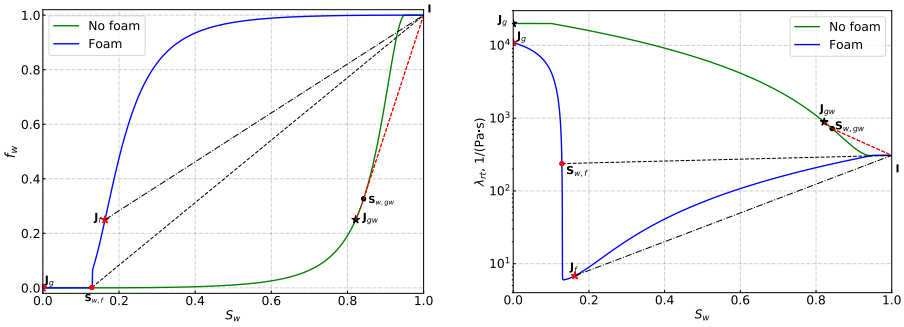

(a) Water fractional flow curves

(b) Total relative mobility curves

Figure 5.6: Water-fractional-flow and total-relative-mobility curves without and with foam. The total relative mobility is defined as the sum of water and gas relative mobility. The dashed lines connect the initial condition (f_w=1) and shock position at leading edge of gas bank. I is the initial condition, J_g is the gas injection condition (f_g=1), and J_f and J_{gw} are foam injection and gas-water co-injection with f_g of 75%, respectively. $S_{w,f}$ and $S_{w,gw}$ are the shock positions with and without foam, respectively.

Fig. 5.7 shows the total-relative-mobility and gas-saturation profiles after 0.2 PVI with f_g = 75% (J_f foam injection and J_{gw} gas-water coinjection in Fig. 5.6). With foam injection (J_f), the total relative mobility is reduced significantly behind the leading edge of the gas bank; the gas saturation thus increases. With the same injected gas fraction, with foam there is a uniform state behind the shock, while the shock is followed by a spreading wave if the foam is absent (Fig. 5.7(a) and Fig. 5.6). The numerical solutions show good agreement with analytical solutions, except for small deviations without foam (Fig. 5.7(a)) which can be eliminated by increasing the grid resolution. These two cases can represent the advance of the mixed zone, as shown in Fig. 5.2.

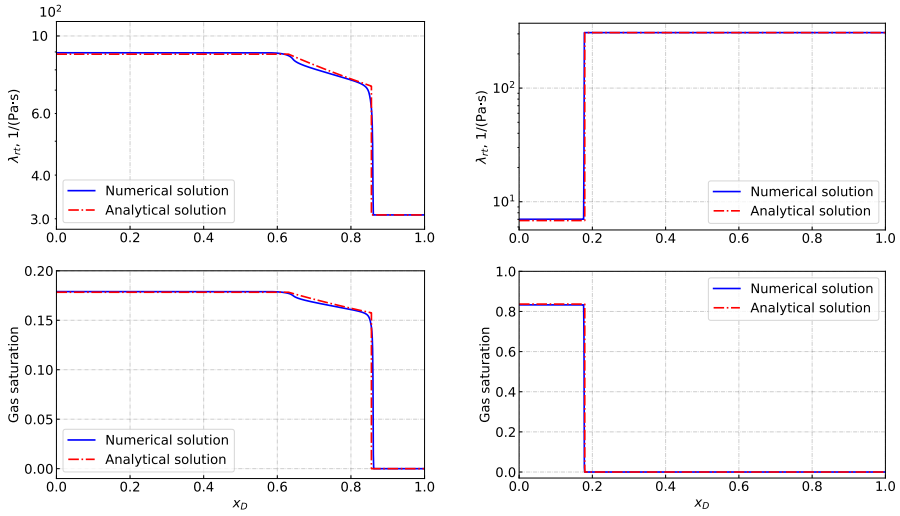

(a) No foam (b) Foam injection

Figure 5.7: Total-relative-mobility and gas-saturation profiles with f_g=80% after 0.2 PVI without and with surfactant present. The top figure is the total-relative-mobility profile, and the bottom is the gas-saturation profile. These two cases can represent the advance of the mixed zone.

Fig. 5.8 shows the total-relative-mobility and gas-saturation profiles after 0.2 PVI with f_g = 100% (J_g in Fig. 5.6). In these two cases, during gas injection, there is a spreading wave behind the shock front. The numerical solutions show good agreement with analytical solutions except at the shock front. Because numerical simulations do not represent shocks well, the numerical total relative mobility is smaller, with an intermediate saturation in at least one grid block between the two banks. In the presence of surfactant, there is an intermediate-mobility zone behind the shock front, a high-gas-mobility zone near the well, and at least one gridblock with extraordinarily low mobility behind the shock front (Fig. 5.8(b)). This low mobility at the leading edge of the gas bank forces a thicker override zone as gas first advances across the reservoir. Thus numerical dispersion (Fig. 5.8, top right) causes the large transition zone between override- and underride-zone in the presence of surfactant, as shown in Fig. 5.2(b). There is no similar effect in the absence of surfactant (Fig. 5.8, top left).

To further verify the causes of transition zones in Fig. 5.2, we then run several small

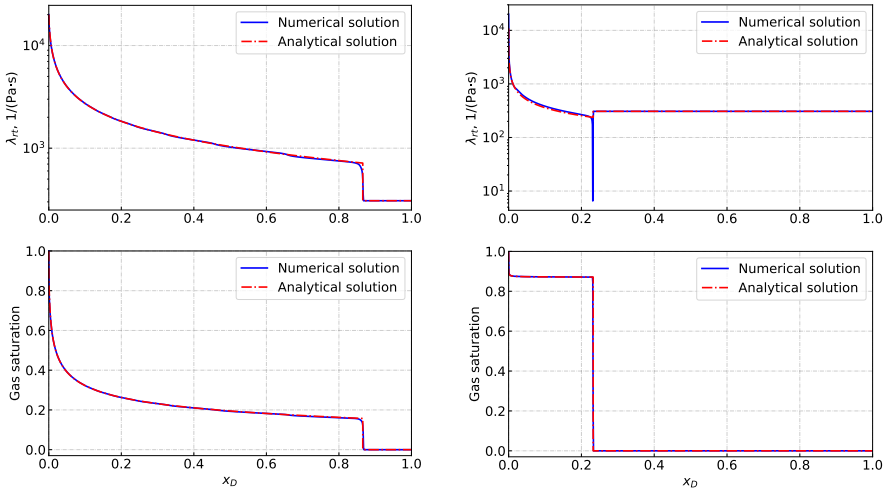

(a) No foam (b) Foam injection

Figure 5.8: Total-relative-mobility and gas-saturation profiles with f_g=100% after 0.2 PVI without and with surfactant present. The top figure is the total-relative-mobility profile, and the bottom is the gas-saturation profile. These two cases can represent the advance of the override zone.

2D models to investigate the effect of grid resolution. For a better resolution, without foam injection, the size of the domain is 30 m × 1 m × 20 m, with different sizes of grid blocks (0.1 m × 1.0 m × 0.1 m, 0.5 m × 1.0 m × 0.5 m and 1.0 m × 1.0 m × 1.0 m); in the presence of foam, the size of the domain is 400 m × 1 m × 30 m with grid block sizes of 1.0 m × 1.0 m × 0.5 m and 1.0 m × 1.0 m × 1.0 m, respectively. The other parameters are the same as those in Section 5.2.1. We find that the transition zone between the mixed and underride zones is insignificant when surfactant is present. We therefore only change the grid block size in vertical direction (dz) to check the effect of grid size on the transition zone beneath the override zone. The injected f_g is fixed at 75% in all cases.

According to Jenkins's model [109], the thickness of over-/under-ride zone at steady-state can be determined by:

$$\frac{H_w}{H_g} = WAG\frac{\lambda_{gg}}{\lambda_{ww}} = \frac{Q_w}{Q_g}\frac{\lambda_{gg}}{\lambda_{ww}} \tag{5.5}$$

where H_w and H_g are the thickness of override zone and underride zone, and λ_{gg} and λ_{ww} are the gas relative mobility in override zone and water relative mobility in underride zone, respectively. Specifically, Jenkins [109] assumes that λ_{gg} is the gas mobility at irreducible water saturation, and λ_{ww} is water mobility at 100% water saturation. WAG ratio is determined by the water volumetric injection rate Q_w, and that of gas, Q_g.

Fig. 5.9 shows gas saturation (no surfactant present) at steady state with different grid sizes. The segregation length differs among the cases due to the change of grid resolution. There is a transition zone existing at the boundary between the mixed and underride zones. Below the override zone, there is another region where gas is not expected to

be present in the model. The height of the override zone is around 1.32 m from Eq. 5.5. With size $dz = 1.0$ m, there is a large deviation in either segregation point or the thickness of the override zone from the analytical result. With a finer grid, this transition shrinks but still appears.

When the grid block size is 0.1 m, the differences between the analytical solutions and numerical solutions are insignificant, as shown in Fig. 5.9(a). Behind the shock front, there is at least one grid block with relatively lower total relative mobility (Fig. 5.6(b)); this difference, however, is insignificant. Numerical simulations do not represent shocks well, we thus can infer that the transition zones between regions are caused by numerical dispersion when the surfactant is absent. By increasing the grid resolution, the numerical solutions are close to analytical solutions, but the computational cost, in turn, increases.

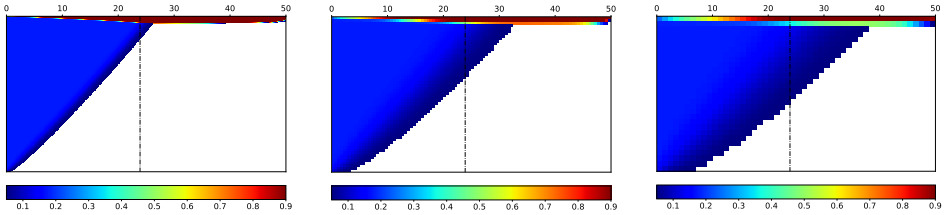

(a) $(dx, dz) = (0.1, 0.1)$ m (b) $(dx, dz) = (0.5, 0.5)$ m (c) $(dx, dz) = (1.0, 1.0)$ m

Figure 5.9: Gas saturation profile (no foam) at steady state with different grid size. In a region with white color, the gas saturation is less than the residual gas saturation. The black dashed line is the segregation point predicted by Eq. 5.1.

Fig. 5.10 shows the gas saturation (with surfactant present) after 2.0 PV gas injection at fg = 75%,with different grid sizes. The transition zone between the mixed zone and the underride zone is negligible. Once foam is injected into the formation, the gas mobility is reduced significantly. Each grid block travels through saturations from injection condition (shock) to initial condition, as shown in Fig. 5.7(b). At all these saturations, the total mobility is intermediate between that at the initial and injected saturations (Fig. 5.6(b)). In the override zone ahead of foam, gas migrates to upper layers and accumulates there . Foam therefore is weaker and weaker until foam collapses completely in the override zone. In this process, all grid blocks in the override zone have to travel through saturations of extremely low mobility (Fig. 5.6(b); Fig. 5.8(b)), thus much gas is diverted into the underride zone. This process is not represented in Stone's model. After steady-state, there is a thick transition region between the override and underride zones. This effect does not disappear with grid refinement. It is a real effect caused by the low mobility in the spreading wave behind the shock [62].

5.4. GRAVITY SEGREGATION IN HETEROGENEOUS POROUS MEDIA

Reservoir heterogeneity influences sweep efficiency and thus recovery. Stone [108] demonstrated that barriers to vertical flow, such as a low-permeability zone, can give an incre-

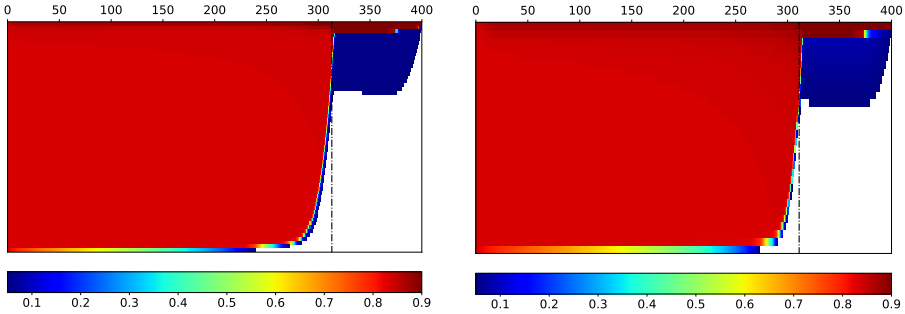

(a) (dx, dz) = (1.0, 0.5) m (b) (dx, dz) = (1.0, 1.0) m

Figure 5.10: Gas saturation profile (foam injection) at steady state with different grid size. In a region with white color, the gas saturation is less than the residual gas saturation. The black dashed line is the segregation point predicted by Eq. (5.1).

5

mental recovery compared to a homogeneous reservoir. In this part, we study the effect of reservoir heterogeneity on gravity segregation during a foam EOR process in a two-layer reservoir, as shown in Fig. 5.11, with different layer permeabilities, thickness, and foam parameters. The total thickness is the same (30 m), but the layer thickness is varied based on different thickness ratios. The permeabilities (K_1 = 32.8 mD, K_2 = 56.8 mD, K_3 = 169.8 mD, and K_4 = 551.5 mD) and the corresponding foam parameters are shown in Table A.2. The total injection rate is fixed at 0.12 m^3/day with foam quality f_g of 75%. We assume for this study that there is no barrier to flow between the layers.

To keep the injection pressure uniform along the entire length of the reservoir (left boundary), the total injection rate is split into two streams based on the total mobility in the mixed zone and the thickness ratio between two layers. Each injection well in each gridblock is fixed with an injection rate by averaging the corresponding stream in that layer. For comparison, we use two homogeneous models to calculate the segregation length as references. These two homogeneous models use the same total injection rate, total thickness, and foam quality as the two-layer model. The uniform permeability is equal to the permeability of either the top layer or the bottom layer.

A dimensionless parameter Ω is defined as

$$\Omega = \frac{L_{g,r} - L_{g,H}}{L_{g,L} - L_{g,H}}, \tag{5.6}$$

where $L_{g,r}$, $L_{g,H}$, and $L_{g,L}$ are segregation length in the two-layer model, single-layer model with higher permeability and single-layer model with lower permeability, respectively. The single-layer model keeps the same conditions as the two-layer model except for the permeability. This parameter Ω can be used to evaluate the effect of the low-permeability layer on the ultimate segregation length of a two-layer system. Ω approaching 1.0 means the segregation length of the two-layer model is dominated by the low-permeability layer; otherwise, if Ω is close to 0.0, the high-permeability layer plays a dominant role. Thickness ratio is defined as the ratio of the top to the bottom layer.

Fig. 5.12 shows the variation of segregation length with different permeability ratios

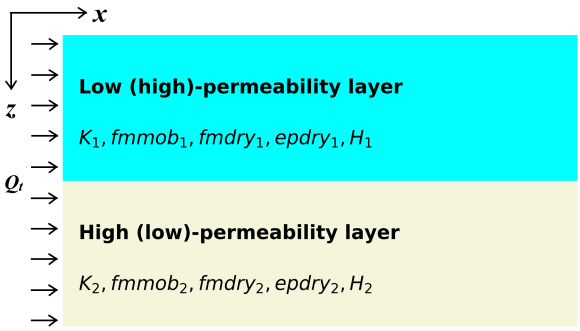

Figure 5.11: Schematic of the 2D layer-parallel flow model used in this Section. In each layer, the thickness (H), permeability (K), and foam parameters ($fmmob$, $fmdry$, $epdry$) are different. For different permeability ratios, the thickness of each layer is also varied, depending on the thickness ratio. The corresponding foam parameters can be found in Table A.2.

and thickness ratios. If the lower-permeability layer is at the bottom, Ω decreases with increasing thickness ratio. The lower-permeability layer at the bottom dominates for ratio greater. Once the thickness ratio is above a certain value, Ω does not change with thickness ratios, approaching to 0, as shown in Fig. 5.12(a). For thickness ratio of 0.5 or greater, the segregation length is completely dominated by the higher-permeability layer. The Ω follows nearly the same trend when the higher-permeability layer is at the top regardless of permeability contrast.

In contrast, Ω increases with the increasing thickness ratio and approaches 1 if the lower-permeability layer is at the top (Fig. 5.12(b)). However, there is a wide spread in results among the cases. When the permeability contrast is larger (i.e., smaller ratio), the required thickness ratio for the lower-permeability layer to dominate increases; the effect of the higher-permeability layer at the bottom is more significant. Ω is not equal to 1 (Fig 5.12(a)) if the higher-permeability layer is at the top, which indicates that the thin high-permeability layer at the top affects the final segregation of the thick low-permeability layer. Similarly, Ω is not equal to 0 (Fig 5.12(b)) when the lower-permeability layer is at the top. The final segregation length is enlarged, consistent with the conclusion that a low-permeability layer at the top can improve the sweep efficiency (i.e., larger segregation distance) [108, 113].

Fig. 5.13 and Fig. 5.14 show the effects of permeability ratio and thickness ratio on total mobility distribution and segregation distance at steady-state. If the higher-permeability layer is at the top, with a smaller thickness ratio (see the left column in Fig. 5.13), the amount of gas in the high-permeability layer almost does not affect segregation in the lower-permeability layer (bottom). Foam is stronger in the high-permeability layer, corresponding to a higher apparent viscosity (see Fig. A.3), which limits the effect of the high-permeability layer on gravity segregation. With increasing thickness of the high-permeability layer, the top layer starts to dominate the segregation process. The segregation occurs earlier in the top layer due to higher total mobility. Once gas and water segregate completely, the gas in the lower-permeability layer at the bottom cannot propagate further.

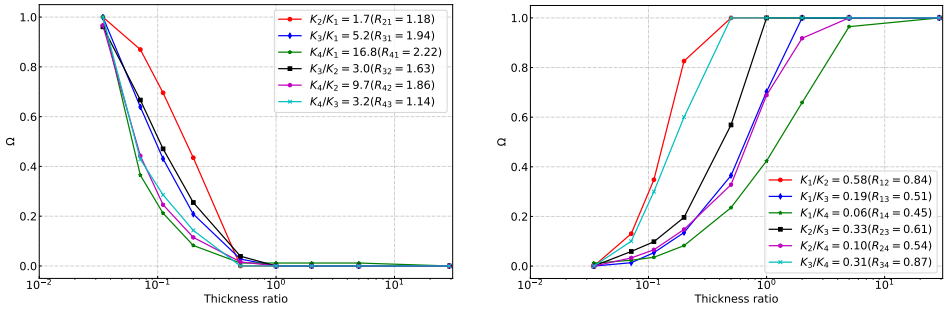

(a) Higher perm. on top (b) Lower perm. on top

Figure 5.12: Gravity-segregation parameter Ω as a function of permeability ratio and thickness ratio. In all cases, K_1<K_2<K_3<K_4. The higher-permeability is at the top in (a), and is at the bottom in (b). The thickness ratio is defined as H_{top}/H_{bottom}. R_{ij} is the ratio of total mobility in the two layers.

5

If the low-permeability layer is at the top, the effect of a thin low-permeability layer is also insignificant (Fig. 5.14); however, the final segregation length of the bottom layer is extended (Ω is above 0 in Fig. 5.12(b)). Note that the height of override zone is also extended a few grid blocks and decreases from the segregation point to the right boundary, especially with a higher permeability contrast, see the last row in Fig. 5.14. Foam moves faster in the high-permeability layer, then much gas invades into the top low-permeability layer ahead of the moving front in the top layer. The amount of gas finally merges into the override zone, leading to a larger override zone in the top layer (Fig. 5.15).

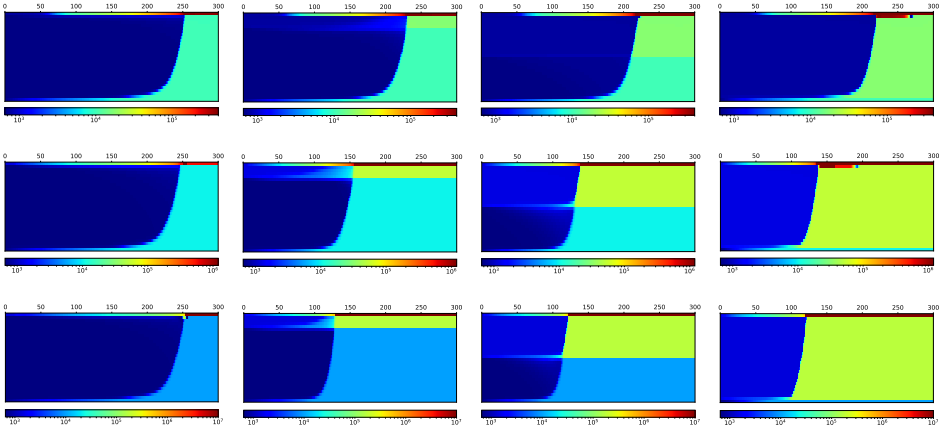

Figure 5.13: Total mobility ($mD/(Pa \cdot s)$) distributions in different layers at steady state. In all cases, the lower-permeability layer is at the bottom. The plots illustrate different permeability ratios $\left(K_2/K_1 \text{ (first row)}, K_3/K_1 \text{ (second row)}, \text{and } K_4/K_1 \text{ (last row)}\right)$ and different thickness ratios $\left(1\text{ m}/29\text{ m (first column)}, 5\text{ m}/25\text{ m (second column)}, 15\text{ m}/15\text{ m (third column)}, \text{and } 29\text{ m}/1\text{ m (last column)}\right)$, respectively.

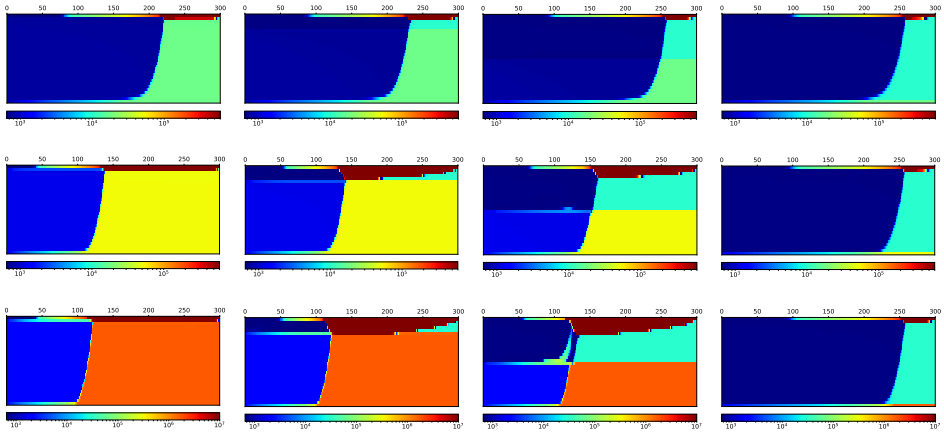

Figure 5.14: Total mobility ($mD/(Pa \cdot s)$) distributions in different layers at steady state. In all case, the higher-permeability layer is at the bottom. The plots illustrate different permeability ratios $\left(K_1/K_2 \text{ (first row)}, K_1/K_3 \text{ (second row)}, \text{ and } K_1/K_4 \text{ (last row)}\right)$ and different thickness ratios $\left(1 \text{ m}/29 \text{ m (first column)}, 5 \text{ m}/25 \text{ m (second column)}, 15 \text{ m}/15 \text{ m (third column)}, \text{ and } 29 \text{ m}/1 \text{ m (last column)}\right)$, respectively.

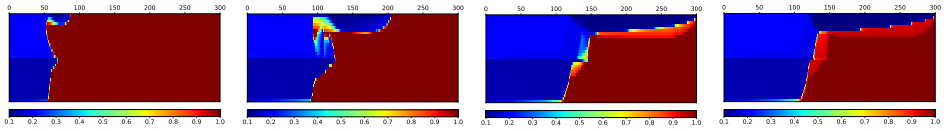

(a) 0.172 PV gas injection (b) 0.344 PV gas injection (c) 0.688 PV gas injection (d) 4.0 PV gas injection

Figure 5.15: Variation of water saturation in transient flow in the case where the low-permeability layer is at the top. The permeability contrast is K_1/K_4 and the thickness is equal in the two layers.

5.5. CONCLUSIONS

In this chapter, we extended the OBL approach to investigate gravity segregation with foam in heterogeneous reservoirs. The following conclusions can be drawn:

- The numerical results show good agreement with analytical solutions in horizontal homogeneous reservoirs in the presence and absence of foam. Through fractional-flow theory, we find that the transition zone during water-gas co-injection is caused by numerical dispersion. The transition zone beneath the override zone with foam injection is not a numerical artefact, but caused by the low gas relative-mobility during the transient displacement process.
- Permeability affects both the mobility reduction of wet foam in the low-quality regime and the limiting capillary pressure at which foam collapses. With a fixed injection rate, the segregation length depends on the combination of vertical permeability and foam apparent viscosity (i.e., total mobility).
- Reservoir heterogeneity plays an important role in gravity segregation. In two-layer models, the thickness of the top layer plays an important role in the ultimate

segregation length. A thin top layer does not affect segregation in the bottom layer, while a thicker top layer dominates the segregation length, with less influence of the bottom layer.

During foam injection, surfactant could lag the gas depending on injected quality and adsorption. In realistic models, heterogeneity is more complex than represented here; that complexity would of cause affect the gravity segregation process. These factors are neglected in this research but remain a future research priority.

6

FOAM-ASSISTED CO_2 STORAGE IN SALINE AQUIFERS

Summary

CO_2-foam injection is a promising technology for reducing gas mobility and increasing trapping within the swept region in deep brine aquifers. In this chapter, a consistent thermodynamic model based on a combination of the Peng-Robinson equation of state (PR EOS) for gas components with an activity model for the aqueous phase is implemented to accurately describe the complex phase-behavior of the CO_2-brine system. The phase-behavior module is combined with the representation of foam by an implicit-texture (IT) model with two flow regimes. This combination can accurately capture the complicated dynamics of miscible CO_2 foam at various stages of the sequestration process. This study evaluates a possible strategy to develop an efficient CO_2 storage technology.

The material presented in this chapter has been published in International Journal of Greenhouse Gas Control, 2021 [9].

6.1. INTRODUCTION

Currently, due to various anthropogenic activities, the concentration of carbon dioxide (CO_2) in the atmosphere is having significant and observable effects on the environment. It's believed to be a major contributor to global climate change, such as rising sea level and ocean acidification [124, 125]. Carbon capture, utilization and storage (CCUS) in subsurface geological formations have been proved to be one viable and promising solution for this environmental issue [17, 126–128]. Deep saline aquifers have been considered as ideal sites for CO_2 injection and long-term storage. Compared to other target geological formations, such as depleted oil and gas reservoirs and coal-bed methane, saline aquifers are ubiquitous worldwide and have the largest potential storage capacity, which makes them feasible for large scale long-term sequestration [129–131].

Typically, the presence of an impermeable seal at the top of a formation can hinder CO_2 from moving upward, trapping CO_2 in aquifers [8, 132, 133]. However, since gas phases generally have higher mobility due to lower viscosity compared to the reservoir fluid, the injected CO_2 will migrate along the top of the reservoir dominated by gravity forces [134]. Along this process, CO_2 may leak into the atmosphere if it reaches faults or abandoned wells [135]. This effect also causes very poor sweep efficiency of CO_2 (i.e., lowering storage capacity).

These potential issues can be overcome or minimized by reducing the gas mobility and increasing trapping within the pore space of the swept region. Simultaneous water and gas (SWAG) injection or water alternating gas (WAG) injection can improve CO_2 sweep efficiency from laboratory studies [136, 137]. Those studies have shown that SWAG and WAG injection reduce CO_2 mobility and improve its sweep efficiency. Streamline-based simulation results show co-injection of water at a volume ratio of 15% increases the storage efficiency around 9.0%, compared to 3.0% when only pure gas is injected, while there is a significant improvement of sweep efficiency [138].

Foam injection is a promising technology for gas-mobility control in the petroleum industry and aquifer remediation [5]. Recently, the foam enhanced oil recovery (EOR) technique is being extended to CO_2 storage, thus reducing greenhouse gas emissions [8, 17, 85]. Foam is an agglomeration of gas bubbles separated from each other by thin liquid films, which can improve the sweep efficiency of injected gases by mitigating or reducing the effect of low gas viscosity and reservoir layers [4, 5, 81]. Currently, foam is used in diversion of acid in well-stimulation treatments, diversion of gas in EOR processes and diversion of treatment fluids in soil remediation processes [83, 84]. Foam-assisted CO_2 injection (i.e., adding surfactant to generate CO_2 foams in situ) provides insights to maximize the potential of CO_2 storage as well.

Fundamentally, capillary effects and the drag on foam films reduce gas mobility considerably (e.g. by $10 \sim 10^4$ times), through trapping of gas bubbles (e.g. 90-99% of gas) and increase of the flow resistance of flowing bubbles [139]. The reduction in gas mobility improves the sweep efficiency remarkably and opens otherwise unswept formation for CO_2 storage. More CO_2 is thus trapped in the pore space rather than migrate upward. The stress on the overburden rock is relaxed, reducing the risk of cracking it. As injection stops, nearly 100% of injected gas in the swept zone is trapped in-situ (as a discontinuous phase) by lamellae [139], as long as foam remains stable. The dispersion of CO_2 in liquid increases the contact area of CO_2 with rock and water and thus affects the storage

process.

Prior to foam deployment, one needs to understand the following key issues. The first one is how to predict the behavior of the injected CO_2 stream. In the post-injection period, the footprint of injected CO_2 plays an important role in the security and permanence of CO_2 storage [131]. The key underlying mechanism is how foam can overcome the instability at the interface between the displacing and displaced phases caused by poor mobility ratio (leading to fingering or channeling) and density contrast (leading to gravity segregation). The second important phenomenon is the residual trapping of CO_2 during the migration through the saline aquifer; then enhanced dissolution starts to play a significant role at longer timescales. We need an accurate model to represent the major physical and chemical processes induced by CO_2 foam injection into potential disposal reservoirs, such as miscible and immiscible displacement, partitioning of CO_2 among different fluid phases and possible thermal effects [126]. Last, but not least, the nonlinearity of this coupled process challenges conventional simulation, which often translates into an extreme computational cost. It is essential to establish a robust and accurate simulation technique which can model these processes in a realistic and quantitative fashion.

Therefore, we study the coupling of CO_2 sequestration with foam injection (co-injecting CO_2 and surfactant solution). For an accurate description of this phase behavior, a recently developed thermodynamic model based on a combination of a cubic Equation of State (EOS) with an activity model has been adopted [52]. This model combines a classic fugacity formulation for the supercritical gas phase and an activity model combined with Henry's law constants for the aqueous brine. This implementation makes the thermodynamic model more accurate than conventional cubic EOS. The implicit-texture (IT) model [65] used in this study assumes that foam generation and destruction reach a local steady-state instantaneously and represents the effect of foam bubbles implicitly by introducing a mobility-reduction factor. This mobility-reduction factor, used to rescale gas mobility with foam, is a function of water saturation, oil saturation, surfactant concentration, capillary number and salinity.

In this chapter, we first validate our simulation capabilities against analytical solutions, mainly focusing on the enhanced CO_2 dissolution. Furthermore, we investigate the behavior of the CO_2 plume with brine-assisted (co-injected CO_2 and brine) and foam-assisted (co-injected CO_2 and surfactant solution) CO_2 injection, including the plume footprint, the amount of CO_2 dissolved and residually trapped, storage capacity and efficiency using an unstructured 3D reservoir with homogeneous properties. We conclude the chapter by summarizing the main conclusions.

6.2. ENHANCED DISSOLUTION

We begin by validating our simulation approach through studying the detailed behavior of gravity induced instabilities and the associated dissolution rate in small domains. Elenius *et al.* [140, 141] investigated the full problem of two-phase flow with gravity currents and convective dissolution in the absence and presence of the capillary transition zone (CTZ), and these results can be used as a benchmark for verification of our simulation approach. In this chapter, we take two small models, as shown in Fig. 6.1. One represents a scenario where the CTZ is negligible, and another one is with a realistic capillary tran-

sition zone. All the parameters which are used in the simulations and the simplifications in these models can be found in Elenius *et al.* [142].

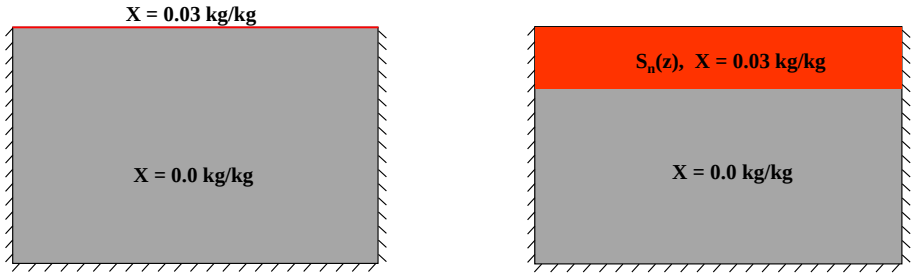

(a) Singe-phase flow (b) Static CTZ

Figure 6.1: Schematic model used in this study. Initial position of region with brine (blue, X = 0 kg/kg) and two-phase conditions (red, X = 0.03 kg/kg, corresponding to x = 0.0125 mol CO_2/mol brine). In (a), now-flow conditions are applied for all boundaries, and the concentration and pressure are fixed at the top of the domain by specifying a large pore volume; in (b), CO_2 is provided by means of the CTZ, but the entire two-phase region has a very large pore volume to maintain the initial saturation profile and the high CO_2 concentration. For further details, see [142].

6

6.2.1. ONSET OF CONVECTION

Here we examine whether our simulation framework can accurately predict the onset of convection and determine how properties of the aquifer and fluid affect the onset time. Based on the linear stability analysis [143], the linear onset time is expressed by:

$$t_{onset} = c_0 \frac{\mu^2 \phi^2 D}{(\Delta \rho g K)^2}. \tag{6.1}$$

Fig. 6.2 obviously demonstrates linear relations between t_{onset} and $1/K^2$, ϕ^2, and D in Eq. 6.1. We point out here that the onset time is defined based on the deviation of the simulated mass flux from a pure diffusive flux [144, 145], i.e., the time at which the mass flux starts to increase. A l_2-fitting is performed based on simulation data to determine the gradient of the line, then to obtain c_0. We found c_0 to be 2873 (K), 1051 (ϕ), and 1027 (D), respectively, which indicates that the fluctuations in ϕ and D cause a shorter onset time. This conclusion is consistent with the results in Pau *et al.* [145]. The magnitude of c_0, reported in the literature, varies in a wide range. The different criteria, which are used to define the onset time, attribute to these discrepancies [143, 146, 147].

The effect of the CTZ on the onset of convection is significant in a two-phase system [148–150]. The presence of a CTZ enhances the instability between the two-phase and brine-saturated region. By direct numerical simulation, we qualitatively evaluate the reduced onset time due to the realistic CTZ, as shown in Fig. 6.2. The onset time with a CTZ is shorter compared to the single-phase flow. The magnitude of reduced onset time depends mainly on the capillary number, which indicates the dominant regime in the instability problem [149].

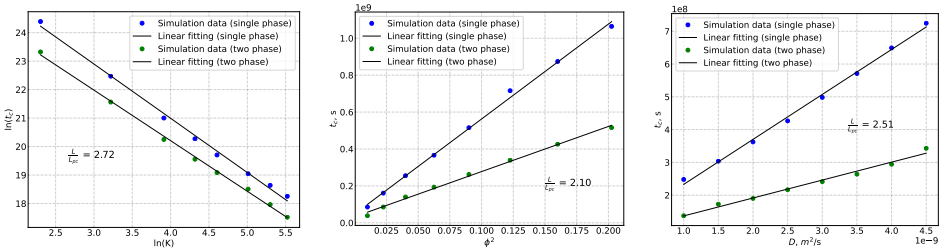

(a) Permeability (b) Porosity (c) Diffusion

Figure 6.2: The relations between the onset of convection and permeability, porosity, and diffusivity. The dots denote the numerical data and the black solid lines represent the best linear-fit.

6.2.2. LONG-TERM ENHANCED DISSOLUTION RATE

After the nonlinear onset time, the mass transfer is mainly dominated by convection: the heavier CO_2-rich brine migrates downward in separate fingers while the lighter fluid among these fingers moves upward. This process substantially augments the dissolution rate, compared to purely diffusive process. Pruess and Zhang [144] found that the CO_2 mass flux stabilizes to a mean value and fluctuates with a ± 15% deviation from the mean. Fig. 6.3 demonstrates the CO_2 concentration for the simulation after 200 years with single-phase brine and the simulation with a stagnant CTZ. Obviously, the stagnant CTZ enhances the concentration of CO_2 in the fingers away from the interface, leading to a faster propagation of the fingers, compared with the no-flux top boundary case. This is consistent with the findings of Elenius *et al.* [140, 141]. Therefore, we can infer that the presence of the stagnant CTZ, to some extent, can improve the storage efficiency by enhancing dissolution rate.

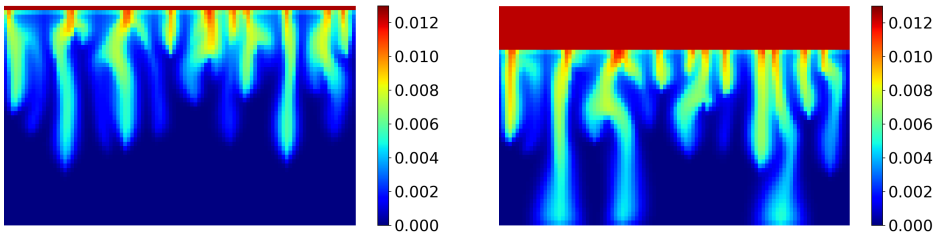

(a) Singe-phase flow (b) Stagnant CTZ

Figure 6.3: Fingers of dissolved CO_2 concentration (mol/mol) at 200 years for the simulations.

Following the definition of dissolution rate in Elenius *et al.* [142], we calculate the rate of CO_2 mass transfer to the (single-phase) brine region across the interface per area (length) of the top interface:

$$F = h\phi\frac{\partial \bar{c}}{\partial t}, \tag{6.2}$$

where h and $\bar{c}$ are the thickness and mean concentration of the single-phase brine region

respectively.

Elenius *et al.* [141] also provided a semi-analytical solution for the dissolution rate with the effect of the capillary transition zone:

$$F = (-0.011 log(d) + 0.016) \frac{K \Delta \rho_w g X_{max} \rho_w(X_{max})}{\mu_w}, \tag{6.3}$$

and at negligible effect of the transition zone:

$$F = 0.021 \frac{K \Delta \rho_w g X_{max} \rho_w(X_{max})}{\mu_w}, \tag{6.4}$$

where K is the permeability, $\Delta \rho_w$ the density difference between brine and brine with dissolved CO_2, g the gravitational acceleration, X_{max} the maximum solubility, μ_w the water viscosity, and d the exponent of the relative-permeability function which is obtained by fitting the water relative permeability.

Fig. 6.4 displays the comparisons between the dissolution rates obtained in simulations (single-phase and CTZ) and by the analytical equation. At the early time, diffusion dominates the mass transfer and the dissolution rate is reduced with time until the nonlinear onset time is reached. It also shows that the presence of CTZ can reduce the onset time. After the nonlinear onset time, fingers start growing and the rate increases due to convection. For both the single-phase and the two-phase with a CTZ simulations, the dissolution rate stabilizes close to the analytical solution.

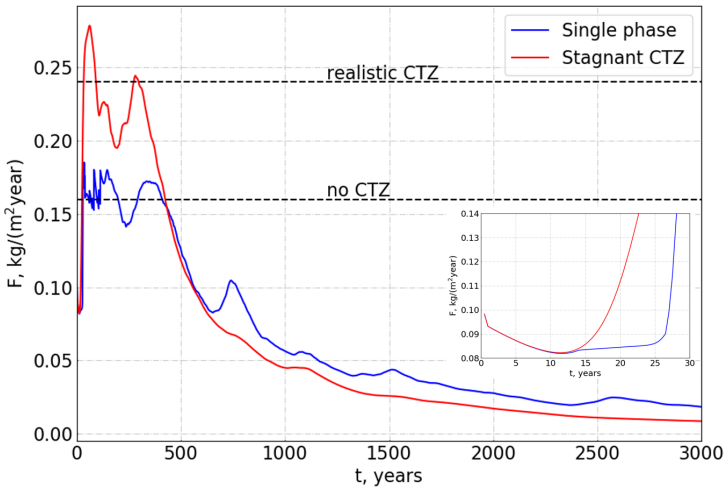

Figure 6.4: Mass flux of CO_2 into the single-phase brine region. The black dashed lines are reported rates obtained by Eq. 6.3 and Eq. 6.4 in the presence and absence of the CTZ. The subfigure inset inside shows the mass flux at early times.

As shown in Fig. 6.4, the dissolution is reduced at late times when CO_2 fingers approach the bottom of the aquifer. Here we use the stagnant CTZ to investigate the behavior of fingers at late times. CO_2 starts to dissolve in brine and fill up the domain gradually (Fig. 6.5a). But the dissolution rate is reduced at late time mainly because of the

merging of fingers and the increase of overall CO_2 concentration. After 3000 years, CO_2 concentration is already rather high, though it is still below the solubility limit anywhere in the single-phase brine region. Our simulation results with the CTZ show a similar t_{peel} = 350 years, i.e., the time at which the dissolution rate starts to decrease, which is consistent with Slim [151]'s findings. After t_{peel}, Slim also found the dissolution decreases from a constant value to a value proportional to $1/(t+g)^2$ without a CTZ ($1/t^2$ in Elenius *et al.* [142]). Here we fit the coefficient g based on our simulation results with the CTZ, and $g \approx -1000$ gives a good match (Fig. 6.5b). These results validate the accuracy of our enhanced dissolution model which will be used in the following study.

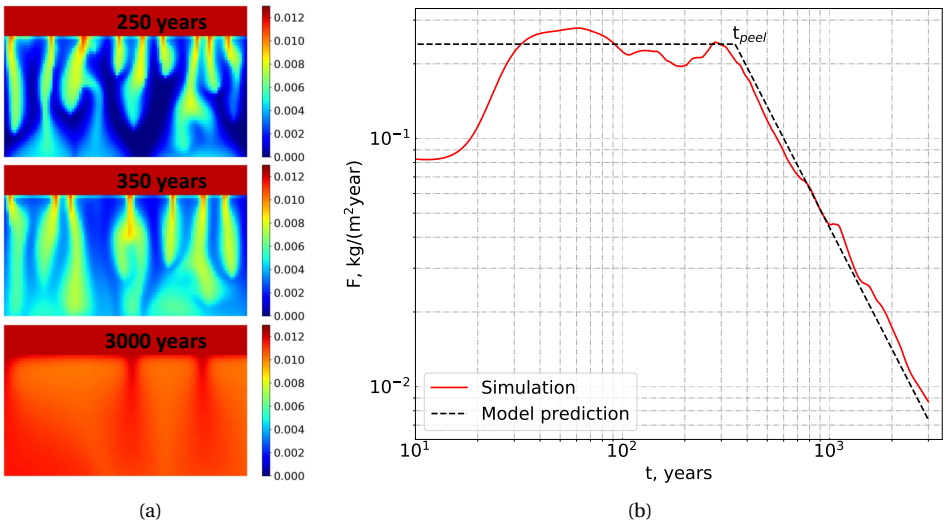

(a) (b)

Figure 6.5: Late-time dissolution with a stagnant CTZ. (a) CO_2 molar concentration (mol/mol) at different time, and (b) dissolution rate. The black dashed lines are dissolution results predicted by Eq. 6.3 for the constant-rate regime and by Slim [151] for the shut-down regime.

6.3. SIMULATION OF FOAM-ASSISTED CO_2 STORAGE

6.3.1. MODEL DESCRIPTION

When CO_2 is injected into a formation saturated with brine, it migrates upwards due to gravity and forms a nearly horizontal layer overlying the brine phase. After a short time, CO_2 starts to dissolve in the brine, as a result of molecular diffusion and density-driven convection and in part is trapped in situ as residual gas. Many researchers have found that foam-assisted CO_2 injection can increase sweep efficiency by mitigating gravity segregation processes [8, 85]. Therefore, it can increase the amount of residual gas. However, most of these studies ignored the effect of foam-assisted injection to enhanced dissolution dominated at later time.

In order to simulate CO_2 sequestration process, we consider a 3D homogeneous horizontal reservoir with unstructured mesh and fine mesh size as shown in Fig. 6.6. The

height and the radius of the model is 30 m and 400 m, respectively. There are 30 layers and the average number of elements in the radial direction is 192. The top and the bottom surfaces of the reservoir are no-flow boundaries. We also assume for simplicity that surfactant is already present in the water phase throughout the porous medium and the adsorption of surfactant is neglected. Other parameters, such as rock and fluid properties, are listed in Table 6.1. Although the scale of this model is just a few hundred meters, it provides an accurate representation of CO_2 sequestration with realistic thermodynamics conditions. As shown in Elenius *et al.* [142], the proposed mesh resolution (around the meter scale) provides a numerically converged solution for enhanced dissolution phenomena, which is studied here in a fully 3D setting.

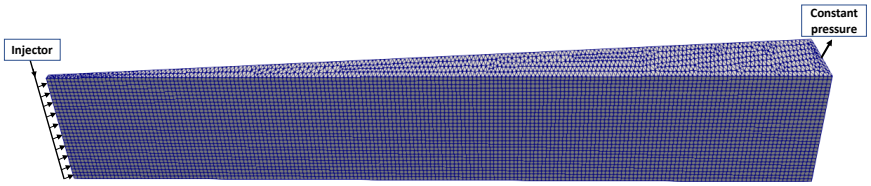

Figure 6.6: Schematic representation of the geometry model used in this study. A very large pore volume is assigned in the right boundary to maintain the initial constant pressure profile.

Table 6.1: Input parameters for the three-dimensional model

Reservoir Properties			
Average mesh size, m^3	1.556	Total number of elements	49320
Permeability, md	100	Porosity	0.3
Initial water saturation	1.0	Initial temperature, ^oC	50
Capillary entry pressure, bar	0.2	Initial pressure, bar	90
Corey gas exponent	2.0	Corey water exponent	4.0
Residual gas saturation	0.2	Connate water saturation	0.2
Endpoint gas relative permeability	0.4	Endpoint relative permeability	1.0
Diffusion coefficient, m^2/day	2×10^{-5}		
Injection condition			
Gas injection rate, rm^3/day	4.0	Water injection rate, rm^3/day	1.0
Foam parameters			
fmdry	0.35	epdry	1000
fmmob	100		

To simplify the problem, we neglect any chemical reactions imposed in the brine by interactions with the CO_2 phase, such as CO_2-rock mineral reactions and CO_2-brine dissociation. The temperature is assumed to be constant during the simulation. The simulation domain, a 5° sector of the cylinder, is initially saturated with formation brine with no dissolved CO_2. The injection well fully perforating the entire vertical interval is located at the left boundary and constant pressure is assumed at right boundary with no-flow conditions along the rest of interfaces. A fixed gas injection rate of 4.0 m^3/day,

corresponds to 0.06 Mt/year normalized to 360°. The injection well is closed after one year of injection to investigate the propagation of CO_2 plume in the closed domain.

Another simplification is the model of gas trapping due to the presence of foam. Gas trapping is an important mechanism in the foam-assisted CO_2 storage process, especially after injection. Friedmann *et al.* [56] measured trapped gas fractions in the range 75% to 90% over a wide range of velocities. Tang and Kovscek [152] found a significant decrease in trapped gas with increasing gas velocity. Jones *et al.* [153] also found in micro-models that as the superficial velocity increases, the fraction of trapped gas decreases. There are no complete models to describe the amount of trapped gas due to the injection of foam. In our study, for simplicity, we assume the residual (i.e., trapped) gas saturation rises by 0.1 in the presence of foam. This assumption is not rigorously correct because, as noted, the trapped gas saturation with foam is larger. Such low value, to some extent, can represent a reduction in gas trapping due to depletion of surfactant in long term. In addition, in the upper layer where foam is collapsed or cannot be generated, the residual saturation does not change. During the simulation, only one set of relative-permeability curve is used. However, gas saturation is much larger than S_{gr} and the only effect of this assumption is a modest reduction in k_{rg}.

Foam-assisted CO_2 storage simulations for a brine aquifer are performed with the Delft Advanced Research Terra Simulator (DARTS) which is capable of modeling complex flow and transport related to various energy applications [40, 43, 44]. A combination of Peng-Robinson [77] and Kritchevsky-Illiinskaya [66] equations of state is deployed in this study because it could provide more reasonable results for the vapor-liquid equilibrium properties as well as the volumetric properties of CO_2 mixtures [154]. The empirical correlation used to determine the brine solution density was developed by Spivey *et al.* [155]. Garcia [156] provided a correlation for the density of brine with dissolved CO_2. The aqueous viscosity is computed by the correlations developed by Mao and Duan [157] (brine solution) and Islam and Carlson [158] (brine with dissolved CO_2). The density and viscosity of non-aqueous phases are determined by Peng and Robinson [77] and Lee *et al.* [159], respectively. The detailed description can be found in Section 2.5.

6.3.2. RESULTS AND DISCUSSION

In this section, we present the results of brine-assisted and foam-assisted CO_2 injection into a homogeneous reservoir, including the behavior of the CO_2 plume in injection and subsequent post-injection processes.

The injected CO_2 exists as supercritical fluid under the selected reservoir conditions. Fig. 6.7 illustrates the saturation of the supercritical CO_2 after 1 year injection. During the brine-assisted CO_2 injection, supercritical CO_2 segregates with water and migrates upwards quickly because of the low density and viscosity of CO_2 compared with the formation brine. In the meantime, it displaces the formation brine and thereby increases the contact area for CO_2 storage. The plume, however, sweeps only the near-well region and then rises to the upper layer. Thus the storage efficiency, especially in the near-well region, is rather low due to the limited swept region.

Foam injection can significantly enlarge the swept area by reducing gas mobility. When CO_2 and surfactant are co-injected into the formation, foam can be generated in the near-well region; then gas mobility is reduced remarkably (max. 100 times in this

study) and much more space will be open for CO_2 storage, see Fig. 6.7(b) for details. The plume front in foam injection moves slowly and uniformly, which reduces the risk of leakage, especially during CO_2 EOR processes where wells distance is limited.

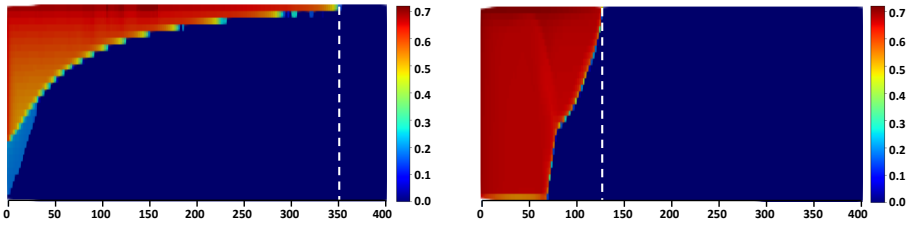

(a) Brine-assisted (b) Foam-assisted

Figure 6.7: Saturation of supercritical CO_2 after 1 year injection. The white dashed line is the CO_2 plume front.

Under steady-state, an analytical model for uniform co-injection of water and gas in homogeneous, horizontal reservoirs can be used to predict the segregation length [108]. In this study, less than 0.1 PV (0.06 PV) gas is injected. No obviously separated regions, therefore, can be distinguished with a sharp boundary compared with the previous research [108, 114]. However, in this transient displacement process, foam exhibits its capacity to hinder gas rising upwards and increase the sweep area. Fig. 6.7(b) shows that the segregation point where water and gas separate completely, is more than 100 m from the injection well. At early time, foam may reduce the dissolution rate due to the reduced contact area between CO_2 and brine in the upper layers. However, in the long run, the dissolution increases because the free gas after segregation as well as collapsed foam still migrates upwards to overlie the brine phase in the upper layer, thus increasing the contact area. With a fixed injection rate, the required injection pressure for foam is much higher, around 125.4 bar; while the injection pressure is only 93.8 bar for co-injecting water and gas.

Fig. 6.8 and Fig. 6.9 display the saturation of the supercritical CO_2 with time. In both cases, mobile CO_2 forms a nearly horizontal layer overlying the brine phase. As shown in Fig. 6.7(a), when injection ceases, the front of CO_2 plume approaches the right boundary. Therefore, the CO_2 plume arrives at the right boundary in a short time in the post-injection process. With the dissolution of CO_2 in the upper part of reservoir, the leading tip retracts and disappears gradually (Fig. 6.8(a) and Fig. 6.9(a)). After foam injection, the gravitational force dominates the flow, and gas migrates upwards and accumulates there. Once gas saturation is high enough (i.e., water saturation is lower than the limiting water saturation) in the upper layer, the foam collapses and gas mobility increases dramatically. Foam cannot be re-generated there, which makes the override zone thin in the foam-assisted post-injection process (Fig. 6.8(b) and Fig. 6.9(b)). Foam-injection retards the late-time dissolution rate. However, the residual trapped CO_2 phase with foam-assisted injection is much greater than that of brine-assisted injection, in terms of the swept area and saturation of immobile gas. Foam increases the swept area and during the post-injection process, the residual gas saturation increases through foam trapping gas bubbles. The enlarged swept area provides higher capacity for residual trapping

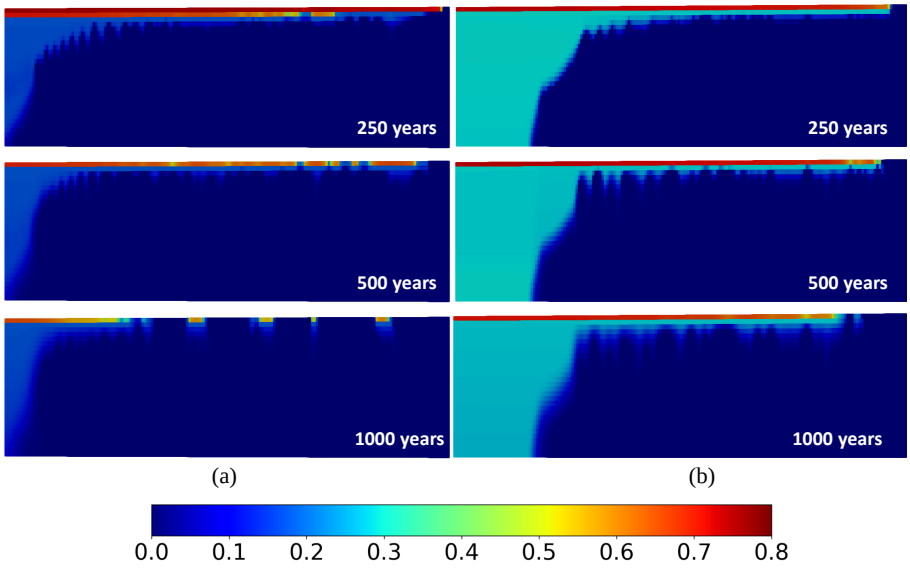

Figure 6.8: Saturation of supercritical CO_2 (front view) after 250, 500 and 1000 years. (a): brine-assisted; (b): foam-assisted.

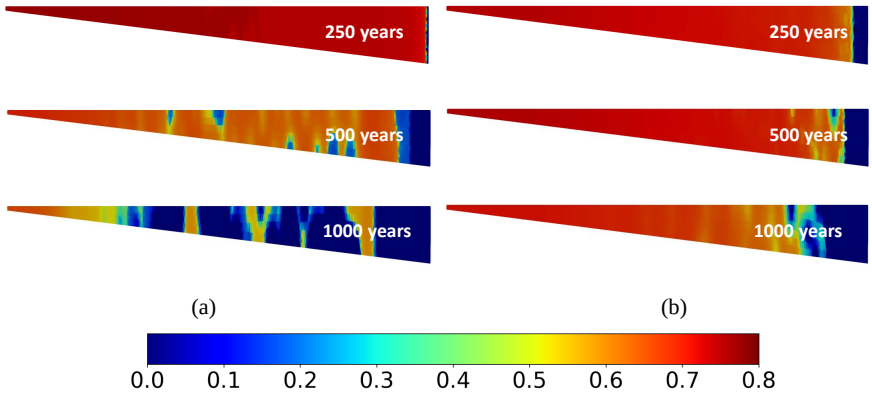

Figure 6.9: Saturation of supercritical CO_2 (top view) after 250, 500 and 1000 years. (a): brine-assisted; (b): foam-assisted.

of CO_2.

In our simulation of one year of injection, there is no override zone ahead of the foam zone until gas injection ceases. At this time, gas migrates upward from the foam zone and forms an override zone that extends radially outward. Over time, as the override zone grows, gas saturation within that zone falls to residual gas saturation. Below the override zone (in dark red in Fig. 6.8(b)), there is a second zone (two grid blocks deep) with residual gas. This zone is created during the advance of the override zone, due to lower mobility of gas at intermediate gas saturations. This effect is magnified by numerical dis-

persion at the displacement front [51]. Later, residual gas in both zones can dissolve into water connected to the top of the aquifer, much as in the capillary transition zone in Section 6.2. Residual CO_2 in both override zones dissolves into brine gradually over time, as shown in Fig. 6.8(a). There is also large zone of trapped residual CO_2 near the well, where the foam remains stable (i.e., at lower water saturation). In practice, one could increase the injection pressure to expand the swept area [114], subject to limitations on injection pressure.

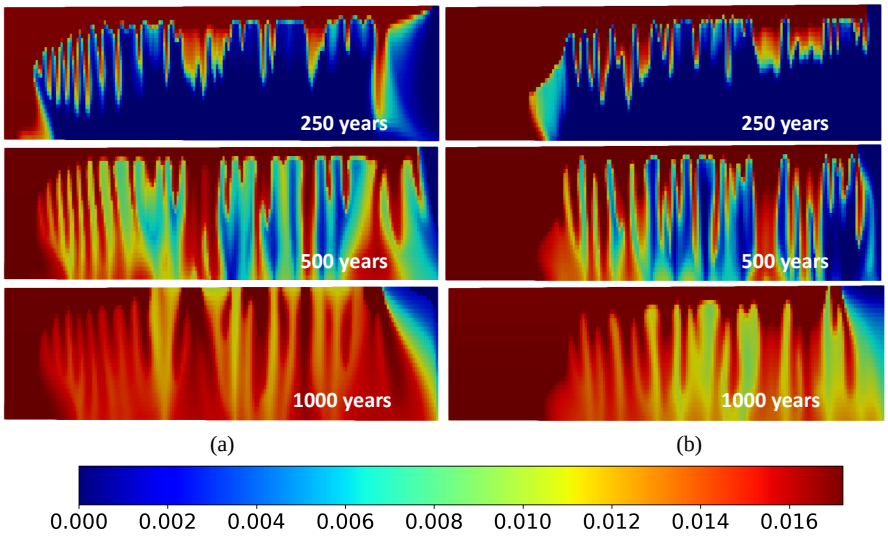

Figure 6.10: CO_2 mole fraction (mol CO_2/mol brine) profile (front view) after 250, 500 and 1000 years. (a) brine-assisted; (b) foam-assisted.

Fig. 6.10 and Fig. 6.11 show the distribution of the dissolved CO_2 mole-fraction with time. CO_2 fingers move downwards and grow gradually in both cases. The fingers between the override zone and bottom brine form earlier in brine-assisted CO_2 injection because override happens rapidly (Fig. 6.10(a) and Fig. 6.11(a)). Finally, the average CO_2 concentration in the whole domain (excluding the residual trapped region) in brine-assisted injection is higher than that with foam-injection. Once the tips of fingers reach the bottom boundary of the domain, CO_2 fingers start to expand in the horizontal direction and merge with others. The number of fingers therefore is reduced, resulting from the mutual interaction between the fingers during the diffusion process. Note that the brine-assisted and foam-assisted CO_2 injection shows similar behavior, including the migration and dissolution of the CO_2 plume. The injection of foam is mainly applied to prevent CO_2 from migrating upwards and reduce the breakthrough time during the injection period: the effects of foam on CO_2 plume migration and dissolution at the upper layers at later time are negligible.

In order to observe how the leading tip propagation changes with time, we show the results in foam-assisted injection (Fig. 6.12) where the leading tip stops before it reaches the right boundary. As mentioned above, foam does not affect the migration of the CO_2

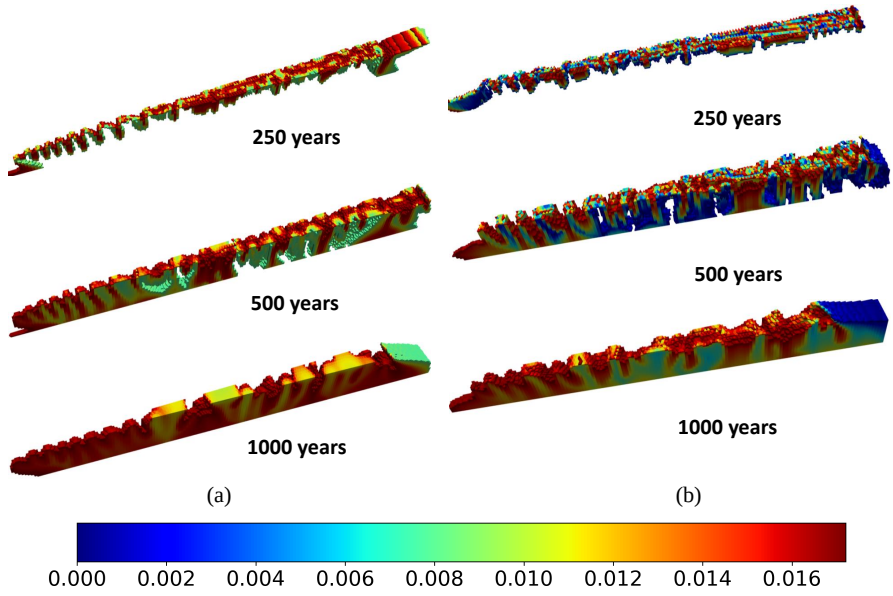

Figure 6.11: CO_2 mole fraction (mol CO_2/mol brine) profile with threshold (3D) view after 250, 500 and 1000 years. (a) brine-assisted; (b) foam-assisted. The concentration of threshold is (0.005, 0.016) in both cases.

override zone, so this result can represent the behavior of the CO_2 plume for either brine-assisted or foam-assisted CO_2 co-injection strategies in the post-injection period as long as the domain is long enough. The plume speed decreases with time until the plume stops and retracts after about approximately 150 years, 370 m away from the injection point. The presence of the CTZ causes a reduction in tip speed. Our results show a similar trend to those of Elenius *et al.* [142]. This interaction between the speed of the leading tip and convective mixing also can be observed from the distribution of dissolved CO_2 under the plume, see Fig. 6.9.

Fig. 6.13 displays the global mass transfer rate into the single-phase brine region, which is defined as the amount of CO_2 entering the single-phase region per unit time: $R = dM_{CO2}/dt$. Both injection strategies show similar results: R increases at early time and later decreases with time. As shown in Elenius *et al.* [142], the global mass-transfer decreases gradually after the t_{peel}, which is different from our simulation results. In our simulation, the thickness of the domain is just 30 m, which causes the fingers reaching the bottom boundary in a very short time (around 150 years). Once the fingers arrive at the bottom, the dissolution rate starts to decrease, also seen in Fig. 6.4. With foam injection, R increases faster at early time and reaches a slightly lower peak. On the one hand, once the injection ceases, foam sweeps much more area, increasing CO_2 trapping, leading to a higher dissolution rate over a short period. On the other hand, the increased residual gas reduces the amount the CO_2 which can dissolve into brine.

In this chapter, all properties are dependent on pressure, temperature and molar composition of each component. Therefore, Eq. 6.3 and Eq. 6.4, are not necessarily valid. However, in the post-injection process, the variation of pressure is slight (~ 3 bar),

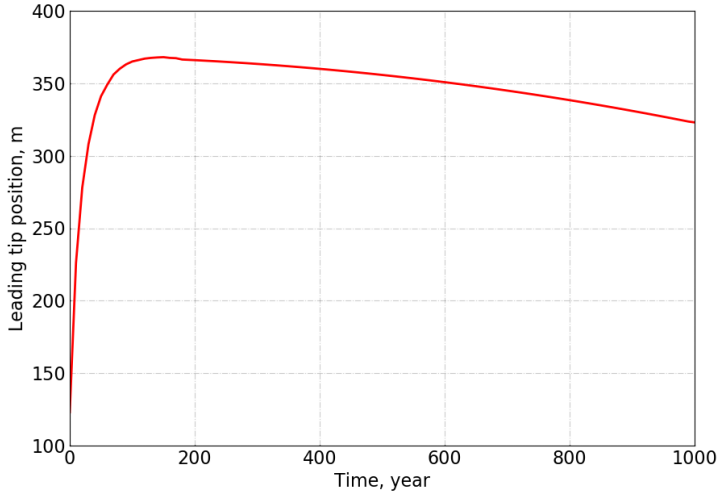

Figure 6.12: Position of the leading tip in foam-assisted injection process.

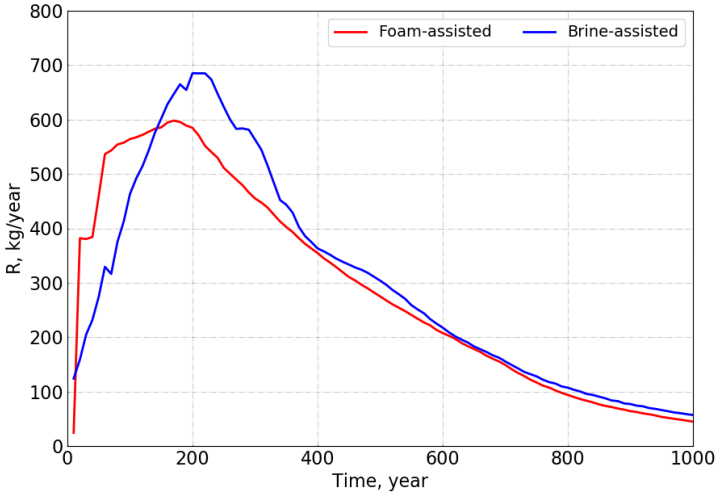

Figure 6.13: Total mass transfer rate R of CO_2 into the single-phase brine region.

and we assume constant temperature. Therefore we still can use Eq. 6.3 to approximate the enhanced dissolution rate due to the presence of the CTZ. Note all the properties in Eq. 6.3 are average: for instance, we calculate all water densities in all elements of the mesh and divide it by the total number of elements to get the corresponding water density. Here, $\Delta\rho_w$ = 5.75 kg/m^3, X_{max} = 0.017 mol/mol (0.0415 kg/kg), $\rho_w(X_{max})$ = 982.6 kg/m^3, and μ_w = 0.86 cp. We then obtain the average dissolution rate with the CTZ, F_{ave} = 0.254 kg/(m^3year) (Eq. 6.3). We compare this analytical dissolution rate with our simulation results. In brine-assisted CO_2 injection, R_{max} = 680 kg/year, corresponding to

F_{max} = 0.325 kg/(m^{3}year) ($F_{max} = R_{max}/(A \times \phi)$). This dissolution rate is 27.9% larger than that of analytical solution.

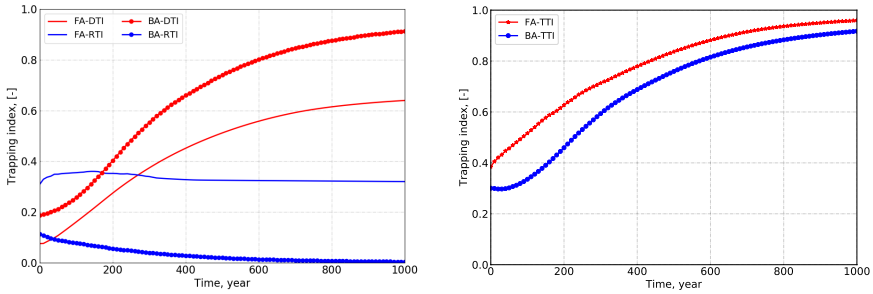

(a) Residual and dissolution trapping

(b) Total trapping

Figure 6.14: Variation of trapping index in different mechanisms. FA: foam-assisted CO_2 injection; BA: brine-assisted CO_2 injection.

Considering the trapping mechanisms and time scale in this research, we estimate the effectiveness of CO_2 geological storage, and three trapping indices are used to represent the contribution of residual trapping and dissolution trapping mechanism,

$$\text{Residual trapping index (RTI)} = \frac{\text{Total mass of residually trapped } CO_2 \text{ (kg)}}{\text{Total mass of injected } CO_2 \text{ (kg)}}, \quad (6.5)$$

$$\text{Dissolution trapping index (DTI)} = \frac{\text{Total mass of dissolved } CO_2 \text{ (kg)}}{\text{Total mass of injected } CO_2 \text{ (kg)}}, \quad (6.6)$$

$$\text{Total trapping index (TTI)} = \text{RTI} + \text{DTI}. \quad (6.7)$$

Fig. 6.14 shows the variation of the trapping indices of different injection strategies over time. The CO_2 plume moves further from the well and enlarges the contact area between the plume and formation brine after shutting off the well. Thus enables much more efficient dissolution of CO_2 into the aqueous phase at the two-phase interface; DTI increases accordingly. The capacity for dissolving CO_2 in brine-assisted CO_2 injection is much greater while the amount of residually trapped CO_2 is lower. The variation of RTI is opposite to that of DTI in both cases and less significant in brine-assisted CO_2 injection. However, residual trapping plays a more important role in foam-assisted injection, with a greater trapping index (0.32). After 1000 years, around 92.5% of CO_2 is dissolved into brine after co-injecting brine and CO_2 compared to 62.3% of dissolved CO_2 with foam-injection. In total, 94.3% of CO_2 is trapped in foam-assisted CO_2 injection, increased by around 1.5% compared to brine-assisted CO_2 injection. The efficiency of CO_2 storage is expressed by the ratio of the volume of CO_2 accessible or occupied by CO_2 in a given pore volume of a porous medium to that volume. Here we only consider the maximum volume swept by mobile CO_2. It is different in these two scenarios, though the total trapping index is close. The storage efficiency of foam-assisted CO_2 injection is about 23.4% which is around 8 times than that of brine-water co-injection (3.0%), due to the enlarged swept area by foam.

As mentioned above, foam can mitigate gravity override during CO_2 injection and reduce the risk of leakage or breakthrough. At early time, foam can improve the amount of trapped CO_2, but in the long run, with the increasing ability of dissolution, the mechanism of residual trapping may play a less-important role. More-accurate modeling is required to predict the foam characteristics in CO_2 storage processes.

In this study, we use a simple foam model to investigate the effect of foam co-injection to CO_2 trapping. This model does not capture all the characteristics, but it still represents some of the most important mechanisms of foam-assisted CO_2 injection. For practical applications, foam generation and coalescence should be included into the physical model, and gas trapping should be represented more completely. There are other essential issues, such as the cost of surfactant, the depletion of surfactant over time, and the foam injectivity, to be considered. These factors will be taken into account in the future research.

6.4. CONCLUSIONS

In this chapter, we applied a realistic phase-behavior model for simulation of CO_2 sequestration in aquifers. The consistent thermodynamic model, based on a combination of a classic cubic equation of state (EOS) for gas components with an activity model for the aqueous phase, can accurately predict the complex phase behavior of the CO_2 plume in brine. An advanced numerical performance provided by the Operator-Based Linearization scheme allows us to perform full-physics simulation in a 3D sector model. The CO_2 sequestration physics is complemented with a foam model which provides us with the ability to investigate the effect of foam co-injection on CO_2 trapping.

The dissolution rate caused by the gravitational instabilities is enhanced further in the presence of a capillary transition zone (CTZ). Our numerical results show good agreement with the analytical solution in the simplified 2D setting.

Foam injection can mitigate gravity override during gas injection by reducing gas mobility. This process increases the amount of residual trapped CO_2 by 32.0% in this study. In addition, the presence of foam reduces the amount of flowing gas, thus reducing the risk of leakage. With a more realistic treatment of enhanced dissolution in 3D model, the predicted average dissolution rate is almost 30% larger than that predicted by the 2D and analytical model.

The final total trapping index in both foam-assisted and brine-assisted injection scenarios are close after 1000 years. It indicates that in the long run (post-injection), with the increasing ability of dissolution, the mechanism of increased residual trapping, due to the presence of foam, may not be significant.

7

RECAPITULATION AND CONCLUDING REMARKS

7.1. MULTIPHASE BENCHMARKS

The Delft Advanced Research Terra Simulator (DARTS), designed based on the Operator-based Linearization (OBL) framework, is capable of modeling complex flow and transport problems related to various energy applications. The main advantage of this approach is a simplified construction of the Jacobian matrix and residuals, since the complex physics-based calculations are translated into generic multi-linear interpolation based on supporting points which are used to store the values of state-dependent operators. As a result, the implementation of fully-implicit simulation code is significantly simplified with the OBL methodology. The discretized PDEs and property evaluations are completely separated from each other. It is combined with high flexibility of the simulation code: direct implementation of all properties in Python has minimal impact on simulation performance. The flexible GMRES with the constrained pressure residual (CPR) preconditioner is implemented to maintain high efficiency for the simulation of large heterogeneous problems. These developments improve the efficiency of DARTS for optimization, data assimilation and uncertainty quantification of large-scale subsurface applications relevant to the energy transition.

In Chapter 3, the capacity of DARTS to handle the highly nonlinear multiphase problem with the presence of capillarity and gravity has been investigated. Capillary pressure is a highly nonlinear function, mainly depending on saturation in a two-phase system if hysteresis effects are not present. With a given capillary-pressure table, the derivatives of capillary pressure with respect to water molar fraction exhibit discontinuity. This discontinuity may cause convergence issues in simulation process, especially in capillary-dominated flow. Due to the flexibility of DARTS code implemented in Python, it is easy to provide a finer-resolution capillary-pressure table or directly implement the analytical model to evaluate p_c and corresponding derivatives, which can improve the accuracy of a simulation.

A one-dimensional black-oil segregation model was designed to validates the OBL approach. Compared to gravity segregation without the capillary force, capillary pressure causes a lower oil saturation in the upper cells, and a higher oil saturation in the lower cells; i.e., the capillary pressure hinders the oil phase moving upwards. With a coarse OBL resolution, there is a big difference between the solutions with conventional linearization of nonlinear physics and the parametrized solutions, especially for pressure. However, if the OBL resolution increases, the difference decreases significantly, corresponding with a minor increase in the nonlinear iterations. The comparison of CPU time shows that the computational cost is reduced significantly by utilizing the OBL approach in DARTS, compared to the conventional simulation. DARTS exhibits both high accuracy and robustness in this case.

Several large-scale petroleum-related black-oil models were then chosen to further verify the efficiency of the code. DARTS can reproduce the results of the legacy simulation with negligible differences. By approximating the reference physics using parameterization, the OBL approach simplifies the assembly of the Jacobian at the linearization stage, leading to a better simulation performance, around 3 times faster than the legacy simulator. Through a dead-oil and compositional kernel, we proved that with increasing degrees of freedom in the simulation problem, DARTS shows its advantages in speeding up the modeling process.

7.2. FOAM APPLICATIONS IN DARTS

In gas enhanced-oil-recovery and carbon dioxide (CO_2) storage processes, one important phenomenon is gravity override due to the lighter density of injected gases. Foam injection is one effective technology for solving these problems. Following the benchmark study, a highly-nonlinear implicit-texture foam model is introduced into DARTS to investigate the foam flow in porous media.

In Chapter 4, we compare our linearization approach to analytical solutions based on fractional-flow theory. The OBL approach shows good agreement with the analytical solutions except in the case where the initial oil saturation is close to $fmoil$. In order to avoid oscillations in saturation profiles, a capillary diffusion term, which eliminates the oscillations, is introduced. This correction is required only for simulations that are nearly free of numerical dispersion. Such models are usually required for an accurate comparison with analytic solutions.

The nonlinear least-squares minimization approach can give a good match with the foam-scan data, but still cannot capture the upward-tilting ∇p contours in the low-quality regime due to a limitation of the current foam model. Given the foam parameters obtained from steady-state experiments, it is still a challenge to match the experimental data. The gradient-optimization technique improves the accuracy of simulation significantly by optimizing the relative-permeability data. However, based on the fitted parameters, the 1D simulation does not show a perfect match with experimental results, due to the limitation of the steady-state foam model. The 3D simulation results improve the accuracy significantly and only misse a very few solution features.

In Chapter 5, the OBL approach is extended to investigate gravity segregation with foam in heterogeneous reservoirs. The numerical results show good agreement with analytical solutions in horizontal homogeneous reservoirs in the presence and absence of

foam. Through fractional-flow theory, we find that the transition zone during water-gas co-injection is caused by numerical dispersion. In contrast, the transition zone beneath the override zone with foam injection is not a numerical artifact, but caused by the low gas relative-mobility during the transient displacement process.

Permeability affects both the mobility reduction of wet foam in the low-quality regime and the limiting capillary pressure at which foam collapses. With a fixed injection rate, the segregation length depends on the combination of vertical permeability and foam apparent viscosity (i.e., total mobility). Reservoir heterogeneity plays an important role in gravity segregation. In two-layer models, the thickness of the top layer plays an important role in the ultimate segregation length. A thin top layer does not affect segregation in the bottom layer, while a thicker top layer dominates the segregation length, with less influence of the bottom layer.

Based on the study in Chapters 4 and 5, foam-assisted CO_2 storage is investigated in Chapter 6. The dissolution rate caused by gravitational instabilities is enhanced further in the presence of a capillary transition zone (CTZ) which is consistent with results reported in the literature. The numerical results of DARTS show good agreement with the analytical solution in the simplified 2D setting.

Foam injection can mitigate gravity override during gas injection by reducing gas mobility. This process increases the amount of residual trapped CO_2 in this study. In addition, the presence of foam reduces the amount of gas flowing to the gas cap, thus reducing the risk of leakage. With a more realistic treatment of enhanced dissolution in 3D domain, the predicted average dissolution rate is almost 30% larger than that predicted by the 2D or analytical model.

The total trapping index of the two cases with brine co-injection and foam co-injection are close to each other in long-term perspective (e.g., after 1000 years). This indicates that in the long run (post-injection) with the enhanced dissolution, the importance of increased residual trapping due to the presence of foam, may not be significant. More researches should be carried out to investigate foam generation and coalescence, gas trapping, and the cost and the depletion of surfactant over time in practical applications.

7.3. FUTURE PERSPECTIVES

7.3.1. NONUNIFORM PARAMETERIZATION AND REDUCTION OF OPERATORS

In this dissertation, all examples are run with the OBL approach using uniform parameterization of physical space. This choice has been proved to be accurate and efficient by comparing with analytic problems and results of legacy simulators. The accuracy of the OBL approach is strongly dependent on the number of supporting points. With highly nonlinear physical properties, the required OBL resolution increases, especially for high-dimension problems, which can affect the generation of supporting points, and the efficiency of the whole simulation. In this work, two typical problems call for non-uniform parameterization. One example is the discontinuity of the capillary-pressure curve in 9th SPE Comparative Solution Project. Another important example is the parameterization of the foam front, where gas-relative permeability is reduced significantly. Both cases require finer parameter space to capture the features. However, the introduction of unstructured non-uniform parametrization can minimize the number of supporting

points in parameter space. Khait *et al.* [41] developed a tie-line-based non-uniform parameterization approach to discretize the parameter space more efficiently based on the thermodynamic behavior of a compositional system. A general non-uniform parameterization approach is still in demand for simulating these specific physical phenomena.

With more physics involved in a simulation, the number of corresponding operators increases as well, which influences the time and cost for the generation of supporting points and operator interpolation. In Chapter 2, we present the treatment of gravity and capillary operators in the current framework. The implementation of PPU within the OBL approach increases the number of flux operators from n_c to $n_c n_p$; thus more time is required to interpolate the values of different operators. A component-potential upwinding approach is proposed in Khait [80] to reduce the number of operators, but an effective coupling with capillary operators is still an open question.

7.3.2. FOAM MODELING

An implicit-texture (IT) model is introduced in DARTS for simulating foam enhanced-oil-recovery (EOR) process. A mobility-reduction factor (MRF), used to rescale gas mobility with foam, is introduced to implicitly represent the effect of gas bubbles. This MRF is a function of multiple factors, such as water saturation, oil saturation, and capillary number. Through this IT model and some numerical techniques, we manage to reproduce the two stages of foam propagation from inlet to outlet as seen in the CT coreflood experiments. However, there are still some details which need to be solved in the future research:

- For the foam model parameter estimation, when we compute all 7 parameters by minimizing the sum of squared errors, it would definitely match the experimental data. However the uniqueness of the parameter values cannot be ensured unless we impose very narrow bounds on those 7 parameters. It is worth investigating an alternative to explore foam-parameter fitting.

- The IT foam model exhibits good performance at the laboratory scale. But the capability of this model to upscale to field scale and accurately predict field-scale observations is one important aspect to demonstrate the advantages of this model and is not explored in our study.

- Some features are missing in the simulation results compared to the experimental data. Population-balance models are indispensable for certain situations: modeling the entrance region to a porous medium where foam is created, the dynamics of the traveling wave at the foam front, and cases where foam generation itself is in doubt. Considering the flexibility and efficiency of DARTS, the population-balance is a good candidate for implementing in DARTS in future research projects.

7.3.3. CO_2 STORAGE IN EOR PROCESS

Carbon capture, utilization and storage (CCUS) is one effective and important technology to reduce greenhouse gas emissions. Depleted oil and gas reservoirs are ideal places for CO_2 storage. The injected CO_2 can improve oil recovery significantly. Meanwhile, it can interact with the underground fluids, and thus be stored in situ and trapped

by a residual or dissolution mechanism. However, CO_2 injection features very poor sweep efficiency; most injected CO_2 rapidly migrates to the top of a reservoir. This issue can be overcome or minimized by reducing gas mobility and increasing trapping within the pore space of the swept region. Foam injection is a promising technology for gas-mobility control in the petroleum industry and aquifer remediation. In Chapter 6, we present a critical analysis of the potentials and challenges in extending foam EOR to large-scale and long-term CO_2 storage. Due to some simplifications and assumptions, not all the characteristics are captured in this work, which should be taken into account in the future research:

- Foam generation and coalescence. For practical applications, foam generation and coalescence should be included into the physical model, and gas trapping should be represented more completely.
- Impact of surfactant depletion over time. The depletion of surfactant, due to chemical degradation over time or dilution by aquifer inflow, may cause foam collapse. The key issue is whether supercritical CO_2 remains trapped sufficiently long for permanent trapping by dissolution or even mineralization in aquifer or injected water.
- Effect of gravity on bubble migration. After injection ceases, gravity is likely the only driving force for bubble migration. It is essential to understand the competition between capillarity and gravity in static foam.

NOMENCLATURE

Physical Symbols

M	accumulation term for mass
F	flux term for mass
q	source/sink term for mass
ρ_p	phase density
n_p	number of fluid phases
n_c	number of components
n_i	exponent for phase relative permeability
z_c	component overall molar fraction
x_{cj}	molar fraction of component c in phase p
s_j	phase saturation
S_{gr}	residual gas saturation
S_{or}	residual oil saturation
S_{wc}	connate water saturation
ϕ	effective rock porosity
ϕ_0	initial rock porosity
c_r	rock compressibility
p_{ref}	reference pressure
$\boldsymbol{u_j}$	phase velocity
$\mathbf{K}$	full permeability tensor
k_{rj}	phase relative permeability
k_{rg}	gas relative permeability in the absence of foam
k_{rg}^f	gas relative permeability in the presence of foam
k_{ro}	oil relative permeability
k_{rw}	water relative permeability
μ_j	phase viscosity
μ_{app}	foam apparent viscosity
p_j	phase pressure
p_c	capillary pressure
p_d	capillary entry pressure
p_n	pressure for non-wetting phase
p_w	pressure for wetting phase
$\boldsymbol{\gamma}_p$	phase specific weight
D	vertical depth vector (up-down oriented)
D_{cj}	diffusive coefficient
ρ_t	total fluid density
r_j	rate for kinetic reaction
v_{cj}	stoichiometric coefficient associated with kinetic reaction j for the component c

$\mathbf{J}_{cj}$	diffusion flux of component c in phase j
CT_a	CT attenuation of air
CT_{air}	CT attenuation of dry core
CT_{brine}	CT attenuation of fully brine-saturated core
CT_{water}	CT attenuation of water
epcap	exponent for shear thinning effect
epdry	parameter controlling the abruptness of foam collapse
epoil	exponent for oil effect
floil	lower-limiting oil saturation
fmcap	reference capillary number
fmdry	limiting water saturation
fmmob	maximum-attainable gas-mobility reduction
fmoil	upper-limiting oil saturation
FM	mobility reduction factor
F_1 *through* F_6	different physical factors on gas mobility reduction
F_2	effect of water saturation
F_3	effect of oil saturation
F_5	effect of shear thinning
N_{ca}	capillary number
σ_{ca}	water/gas surface tension
ψ_c	fugacity coefficient of the gas phase
h_c	Henry's constant
κ_c	activity coefficient
K_c	phase-equilibrium constant of component

7

Linearization Operators

$\alpha(\omega)$	mass accumulation operator
$\beta(\omega)$	mass flux operator
$\gamma(\omega)$	mass diffusion operator
$\delta(\omega)$	reaction operator
$\chi(\omega)$	mass gradient operator
$\zeta_p^{vol}(\omega)$	volumetric well rate operator
$\zeta_p^{vol}(\omega)$	mass well rate operator
$\delta_p(\omega)$	phase density operator
$\xi(\omega)$	capillarity operator

Other Symbols

Γ^l	fluid transmissibility
Γ_T	rock thermal transmissibility
$\Phi_{p,ij}$	potential difference of phase p between block i and j

REFERENCES

[1] H. Ritchie and M. Roser, *Co_2 and greenhouse gas emissions,* Our World in Data (2020), https://ourworldindata.org/co2-and-other-greenhouse-gas-emissions.

[2] IEA, *Ccus in clean energy transitions,* International Energy Agency (2020), https://www.iea.org/reports/ccus-in-clean-energy-transitions.

[3] J. Tang, *The Effect of Oil on Foam for Enhanced Oil Recovery: Theory and Measurements*, Ph.D. thesis, Delft University of Technology (2019).

[4] L. L. Schramm, *Foams: fundamentals and applications in the petroleum industry*, Vol. 242 (American Chemical Society Washington, DC, 1994).

[5] W. R. Rossen, *Foams in enhanced oil recovery,* Foams: Theory, Measurements and Applications **57**, 413 (1996).

[6] Z. F. Dholkawala, H. Sarma, and S. Kam, *Application of fractional flow theory to foams in porous media,* Journal of Petroleum Science and Engineering **57**, 152 (2007).

[7] S. H. Talebian, R. Masoudi, I. M. Tan, and P. L. Zitha, *Foam assisted co2-eor; concepts, challenges and applications,* in *SPE Enhanced Oil Recovery Conference* (Society of Petroleum Engineers, 2013).

[8] S. Vitoonkijvanich, A. M. AlSofi, and M. J. Blunt, *Design of foam-assisted carbon dioxide storage in a north sea aquifer using streamline-based simulation,* International Journal of Greenhouse Gas Control **33**, 113 (2015).

[9] X. Lyu, D. Voskov, and W. R. Rossen, *Numerical investigations of foam-assisted co2 storage in saline aquifers,* International Journal of Greenhouse Gas Control **108**, 103314 (2021).

[10] A. Skauge, J. Solbakken, P. A. Ormehaug, and M. G. Aarra, *Foam generation, propagation and stability in porous medium,* Transport in Porous Media **131**, 5 (2020).

[11] A. Kovscek, T. Patzek, and C. Radke, *A mechanistic population balance model for transient and steady-state foam flow in boise sandstone,* Chemical Engineering Science **50**, 3783 (1995).

[12] S. I. Kam, Q. P. Nguyen, Q. Li, and W. R. Rossen, *Dynamic simulations with an improved model for foam generation,* SPE Journal **12**, 35 (2007).

[13] L. Cheng, A. Reme, D. Shan, D. Coombe, and W. Rossen, *Simulating foam processes at high and low foam qualities,* in *SPE/DOE improved oil recovery symposium* (Society of Petroleum Engineers, 2000).

[14] C. S. Boeije and W. Rossen, *Fitting foam-simulation-model parameters to data: I. coinjection of gas and liquid,* SPE Reservoir Evaluation & Engineering **18**, 264 (2015).

[15] Z. Zhou and W. Rossen, *Applying fractional-flow theory to foam processes at the" limiting capillary pressure"*, SPE Advanced Technology Series **3**, 154 (1995).

[16] A. H. Al Ayesh, R. Salazar, R. Farajzadeh, S. Vincent-Bonnieu, and W. R. Rossen, *Foam diversion in heterogeneous reservoirs: effect of permeability and injection method,* SPE Journal **22**, 1 (2017).

[17] Z. P. Alcorn, S. B. Fredriksen, M. Sharma, A. U. Rognmo, T. L. Føyen, M. A. Fernø, and A. Graue, *An integrated carbon-dioxide-foam enhanced-oil-recovery pilot program with combined carbon capture, utilization, and storage in an onshore texas heterogeneous carbonate field,* SPE Reservoir Evaluation & Engineering **22**, 1449 (2019).

[18] M. Todd, P. O'dell, and G. Hirasaki, *Methods for increased accuracy in numerical reservoir simulators,* Society of Petroleum Engineers Journal **12**, 515 (1972).

[19] A. Spillette, J. Hillestad, and H. Stone, *A high-stability sequential solution approach to reservoir simulation,* in *Fall Meeting of the Society of Petroleum Engineers of AIME* (Society of Petroleum Engineers, 1973).

[20] G. Thomas and D. Thurnau, *Reservoir simulation using an adaptive implicit method,* Society of Petroleum Engineers Journal **23**, 759 (1983).

[21] K. Aziz, *Petroleum reservoir simulation,* Applied Science Publishers **476** (1979).

[22] K. H. Coats, L. Thomas, and R. Pierson, *Compositional and black oil reservoir simulation,* in *SPE Reservoir Simulation Symposium* (Society of Petroleum Engineers, 1995).

[23] M. G. Edwards and C. F. Rogers, *Finite volume discretization with imposed flux continuity for the general tensor pressure equation,* Computational geosciences **2**, 259 (1998).

[24] D. Peaceman, *A nonlinear stability analysis for difference equations using semi-implicit mobility,* Society of Petroleum Engineers Journal **17**, 79 (1977).

[25] R. E. Ewing, *Simulation of multiphase flows in porous media,* Transport in Porous Media **6**, 479 (1991).

[26] L. Young and T. Russell, *Implementation of an adaptive implicit method,* in *SPE Symposium on Reservoir Simulation* (Society of Petroleum Engineers, 1993).

[27] D. W. Peaceman, *Fundamentals of numerical reservoir simulation*, Vol. 6 (Elsevier, 2000).

[28] H. Cao, *Development of techniques for general purpose simulators*, Ph.D. thesis, Stanford University Stanford, CA (2002).

[29] K. Aziz and T. Wong, *Considerations in the development of multipurpose reservoir simulation models,* in *proceedings of the 1st and 2nd International Forum on Reservoir Simulation, Alpbach, Austria* (1989).

[30] D. V. Voskov and H. A. Tchelepi, *Comparison of nonlinear formulations for two-phase multi-component eos based simulation,* Journal of Petroleum Science and Engineering **82**, 101 (2012).

[31] J. Chang and Y. C. Yortsos, *Effect of capillary heterogeneity on buckley-leverett displacement,* SPE reservoir engineering **7**, 285 (1992).

[32] R. M. Younis, *Modern advances in software and solution algorithms for reservoir simulation*, Ph.D. thesis, Stanford University (2011).

[33] R. Zaydullin, D. Voskov, and H. Tchelepi, *Phase-state identification bypass method for three-phase thermal compositional simulation,* Computational Geosciences **20**, 461 (2016).

[34] T. Garipov, P. Tomin, R. Rin, D. Voskov, and H. Tchelepi, *Unified thermo-compositional-mechanical framework for reservoir simulation,* Computational Geosciences **22**, 1039 (2018).

[35] B. Li and H. A. Tchelepi, *Nonlinear analysis of multiphase transport in porous media in the presence of viscous, buoyancy, and capillary forces,* Journal of Computational Physics **297**, 104 (2015).

[36] F. P. Hamon, B. T. Mallison, and H. A. Tchelepi, *Implicit hybrid upwinding for two-phase flow in heterogeneous porous media with buoyancy and capillarity,* Computer Methods in Applied Mechanics and Engineering **331**, 701 (2018).

[37] K. H. Coats, *An equation of state compositional model,* SPE Journal **20**, 363 (1980).

[38] D. V. Voskov, *Operator-based linearization approach for modeling of multiphase multi-component flow in porous media,* Journal of Computational Physics **337**, 275 (2017).

[39] R. Zaydullin, D. Voskov, and H. A. Tchelepi, *Nonlinear formulation based on an equation-of-state free method for compositional flow simulation,* SPE Journal **18**, 264 (2012).

[40] M. Khait and D. V. Voskov, *Operator-based linearization for general purpose reservoir simulation,* Journal of Petroleum Science and Engineering **157**, 990 (2017).

[41] M. Khait, D. Voskov, and G. Konidala, *Tie-simplex parametrization for operator-based linearization for non-isothermal multiphase compositional flow in porous,* in *ECMOR XVI-16th European Conference on the Mathematics of Oil Recovery*, Vol. 2018 (European Association of Geoscientists & Engineers, 2018) pp. 1–16.

[42] M. Khait and D. Voskov, *Adaptive parameterization for solving of thermal/compositional nonlinear flow and transport with buoyancy,* SPE Journal **23**, 522 (2018).

[43] K. Kala and D. Voskov, *Element balance formulation in reactive compositional flow and transport with parameterization technique,* Computational Geosciences **24**, 609 (2020).

[44] Y. Wang, D. Voskov, M. Khait, and D. Bruhn, *An efficient numerical simulator for geothermal simulation: A benchmark study,* Applied Energy **264**, 114693 (2020).

[45] M. Khait, D. Voskov, and R. Zaydullin, *High performance framework for modelling of complex subsurface flow and transport applications,* in *ECMOR XVII*, Vol. 2020 (European Association of Geoscientists & Engineers, 2020) pp. 1–18.

[46] Y. Saad and M. H. Schultz, *Gmres: A generalized minimal residual algorithm for solving nonsymmetric linear systems,* SIAM Journal on scientific and statistical computing **7**, 856 (1986).

[47] Y. Saad, *A flexible inner-outer preconditioned gmres algorithm,* SIAM Journal on Scientific Computing **14**, 461 (1993).

[48] J. R. Wallis, R. Kendall, and T. Little, *Constrained residual acceleration of conjugate residual methods,* in *SPE Reservoir Simulation Symposium* (Society of Petroleum Engineers, 1985).

[49] X. Lyu, M. Khait, and D. Voskov, *Operator-based linearization approach for modeling of multiphase flow with buoyancy and capillarity,* SPE Journal , 1 (2021).

[50] X. Lyu, D. Voskov, J. Tang, and W. R. Rossen, *Simulation of foam enhanced-oil-recovery processes using operator-based linearization approach,* SPE Journal , 1 (2021).

[51] X. Lyu, D. Voskov, and W. Rossen, *Gravity segregation with co2 foam in heterogeneous reservoirs,* in *IOR 2021*, Vol. 2021 (European Association of Geoscientists & Engineers, 2021) pp. 1–16.

[52] Z. Ziabakhsh-Ganji and H. Kooi, *An equation of state for thermodynamic equilibrium of gas mixtures and brines to allow simulation of the effects of impurities in subsurface CO_2 storage,* International Journal of Greenhouse Gas Control **11**, S21 (2012).

[53] M. Khait and D. Voskov, *Operator-based linearization for efficient modeling of geothermal processes,* Geothermics **74**, 7 (2018).

[54] M. Khait, D. Voskov, *et al.*, *Integrated framework for modelling of thermal-compositional multiphase flow in porous media,* in *SPE Reservoir Simulation Conference* (Society of Petroleum Engineers, 2019).

[55] A. Falls, G. Hirasaki, T. e. a. Patzek, D. Gauglitz, D. Miller, and T. Ratulowski, *Development of a mechanistic foam simulator: the population balance and generation by snap-off,* SPE reservoir engineering **3**, 884 (1988).

[56] F. Friedmann, W. Chen, and P. Gauglitz, *Experimental and simulation study of high-temperature foam displacement in porous media,* SPE Reservoir Engineering **6**, 37 (1991).

[57] C. Marfoe, H. Kazemi, and W. Ramirez, *Numerical simulation of foam flow in porous media,* in *SPE Annual Technical Conference and Exhibition* (Society of Petroleum Engineers, 1987).

[58] M. Islam and S. Ali, *Numerical simulation of foam flow in porous media,* in *Annual Technical Meeting* (Petroleum Society of Canada, 1988).

[59] T. Patzek and N. Myhill, *Simulation of the bishop steam foam pilot,* in *SPE California Regional Meeting* (Society of Petroleum Engineers, 1989).

[60] A. Fisher, R. Foulser, and S. Goodyear, *Mathematical modeling of foam flooding,* in *SPE/DOE enhanced oil recovery symposium* (Society of Petroleum Engineers, 1990).

[61] D.-S. Law, Z.-M. Yang, and T. Stone, *Effect of the presence of oil on foam performance: a field simulation study,* SPE reservoir engineering **7**, 228 (1992).

[62] W. Rossen, *Numerical challenges in foam simulation: A review,* in *SPE annual technical conference and exhibition* (Society of Petroleum Engineers, 2013).

[63] W. Osterloh and M. Jante Jr, *Effects of gas and liquid velocity on steady-state foam flow at high temperature,* in *SPE/DOE Enhanced Oil Recovery Symposium* (Society of Petroleum Engineers, 1992).

[64] J. Alverez, H. Rivas, and W. Rossen, *A unified model for steady-state foam behavior at high and low foam qualities,* in *IOR 1999-10th European Symposium on Improved Oil Recovery* (1999).

[65] S. U. Guide, *Computer modeling group ltd,* Calgary, AB, Canada (2012).

[66] I. Kritchevsky and A. Iliinskaya, *Partial molal volumes of gases dissolved in liquids.(a contribution to the thermodynamics of dilute solutions of non-electrolytes),* Acta Physicochim. URSS **20**, 327 (1945).

[67] N. Spycher, K. Pruess, and J. Ennis-King, *CO_2–H_2O mixtures in the geological sequestration of CO_2. i. assessment and calculation of mutual solubilities from 12 to 100 c and up to 600 bar,* Geochimica et cosmochimica acta **67**, 3015 (2003).

[68] A. Iranshahr, D. Voskov, and H. Tchelepi, *Generalized negative-flash method for multiphase multicomponent systems,* Fluid Phase Equilibria **299**, 272 (2010).

[69] N. Morshuis, *An improved carbon dioxide thermodynamic model applied for reservoir simulation: Implementation of an improved thermodynamic model in Delft Advanced Terra Simulator (DARTS) and an investigation into the effects of impurities on gas plume behaviour*, Tech. Rep. (Delft University of Technology, 2019).

[70] A. S. Odeh, *Comparison of solutions to a three-dimensional black-oil reservoir simulation problem (includes associated paper 9741),* Journal of Petroleum Technology **33**, 13 (1981).

[71] J. Killough, *Ninth spe comparative solution project: a reexamination of black-oil simulation,* in *SPE Reservoir Simulation Symposium* (Society of Petroleum Engineers, 1995).

[72] M. A. Christie and M. Blunt, *Tenth spe comparative solution project: A comparison of upscaling techniques,* in *SPE Reservoir Simulation Symposium* (Society of Petroleum Engineers, 2001).

[73] A. T. Gaspar, A. Santos, C. Maschio, G. Avansi, and D. Schiozer, *Unisim-im: study case for management variables optimization of reservoir exploitation strategy,* International Journal of Modeling and Simulation for the Petroleum Industry **9**, 1 (2015).

[74] G. D. Avansi and D. J. Schiozer, *Unisim-i: synthetic model for reservoir development and management applications,* International Journal of Modeling and Simulation for the Petroleum Industry **9**, 21 (2015).

[75] F. M. Orr Jr, B. Dindoruk, and R. T. Johns, *Theory of multicomponent gas/oil displacements,* Industrial & engineering chemistry research **34**, 2661 (1995).

[76] J. Killough, C. Kossack, *et al.*, *Fifth comparative solution project: evaluation of miscible flood simulators,* in *SPE Symposium on Reservoir Simulation* (Society of Petroleum Engineers, 1987).

[77] D.-Y. Peng and D. B. Robinson, *A new two-constant equation of state,* Industrial & Engineering Chemistry Fundamentals **15**, 59 (1976).

[78] J. Lohrenz, B. G. Bray, C. R. Clark, *et al.*, *Calculating viscosities of reservoir fluids from their compositions,* Journal of Petroleum Technology **16**, 1 (1964).

[79] K. M. Pour and D. Voskov, *Adaptive nonlinear solver for a discrete fracture model in operator-based linearization framework,* in *ECMOR XVII-17th European Conference on the Mathematics of Oil Recovery* (2020).

[80] M. Khait, *Delft Advanced Research Terra Simulator: General Purpose Reservoir Simulator with Operator-Based Linearization*, Ph.D. thesis, Delft University of Technology (2019).

[81] J. J. Bikerman, *Foams*, Vol. 10 (Springer Science & Business Media, 1973).

[82] S. Deshpande, B. Shiau, D. Wade, D. Sabatini, and J. Harwell, *Surfactant selection for enhancing ex situ soil washing,* Water Research **33**, 351 (1999).

[83] W. Rossen and M. Wang, *Modeling foams for acid diversion,* SPE Journal **4**, 92 (1999).

[84] L. W. Lake, R. Johns, W. R. Rossen, and G. A. Pope, *Fundamentals of enhanced oil recovery,* (2014).

[85] M. Izadi and S. Kam, *Investigating supercritical co 2 foam propagation distance: Conversion from strong foam to weak foam vs. gravity segregation,* Transport in Porous Media , 1 (2018).

[86] A. Rognmo, S. Heldal, and M. Fernø, *Silica nanoparticles to stabilize co2-foam for improved co2 utilization: Enhanced co2 storage and oil recovery from mature oil reservoirs,* Fuel **216**, 621 (2018).

[87] C. Esene, S. Zendehboudi, A. Aborig, and H. Shiri, *A modeling strategy to investigate carbonated water injection for eor and co2 sequestration,* Fuel **252**, 710 (2019).

[88] R. Farajzadeh, A. Andrianov, R. Krastev, G. Hirasaki, and W. R. Rossen, *Foam-oil interaction in porous media: implications for foam assisted enhanced oil recovery,* Advances in colloid and interface science **183**, 1 (2012).

[89] J. Tang, S. Vincent-Bonnieu, and W. Rossen, *Experimental investigation of the effect of oil on steady-state foam flow in porous media,* SPE Journal **24**, 140 (2018).

[90] H. Chen, A. S. Elhag, Y. Chen, J. A. Noguera, A. M. AlSumaiti, G. J. Hirasaki, Q. P. Nguyen, S. L. Biswal, S. Yang, and K. P. Johnston, *Oil effect on co2 foam stabilized by a switchable amine surfactant at high temperature and high salinity,* Fuel **227**, 247 (2018).

[91] K. Mannhardt, J. Novosad, and L. Schramm, *Foam/oil interations at reservoir conditions,* in *SPE/DOE Improved Oil Recovery Symposium* (Society of Petroleum Engineers, 1998).

[92] M. N. Zanganeh, S. I. Kam, T. LaForce, and W. R. Rossen, *The method of characteristics applied to oil displacement by foam,* SPE journal **16**, 8 (2011).

[93] A. Andrianov, R. Farajzadeh, M. Mahmoodi Nick, M. Talanana, and P. L. Zitha, *Immiscible foam for enhancing oil recovery: bulk and porous media experiments,* Industrial & Engineering Chemistry Research **51**, 2214 (2012).

[94] K. Osei-Bonsu, P. Grassia, and N. Shokri, *Relationship between bulk foam stability, surfactant formulation and oil displacement efficiency in porous media,* Fuel **203**, 403 (2017).

[95] K. Zhang, S. Li, and L. Liu, *Optimized foam-assisted co2 enhanced oil recovery technology in tight oil reservoirs,* Fuel **267**, 117099 (2020).

[96] A. Hussain, A. Amin, S. Vincent-Bonnieu, R. Farajzadeh, A. Andrianov, P. A. Hamid, and W. Rossen, *Effect of oil on gravity segregation in sag foam flooding,* in *IOR 2017-19th European Symposium on Improved Oil Recovery*, Vol. 2017 (European Association of Geoscientists & Engineers, 2017) pp. 1–16.

[97] S. Hosseini-Nasab, F. Douarche, M. Simjoo, L. Nabzar, B. Bourbiaux, P. Zitha, and F. Roggero, *Numerical simulation of foam flooding in porous media in the absence and presence of oleic phase,* Fuel **225**, 655 (2018).

[98] M. Nell, *Oil foam interaction: Simulation of foam displacement with oil,* (2015), http://resolver.tudelft.nl/uuid:c0c5d125-42a9-41df-8393-073dc4ba57bd.

[99] Y. Zeng, A. Muthuswamy, K. Ma, L. Wang, R. Farajzadeh, M. Puerto, S. Vincent-Bonnieu, A. A. Eftekhari, Y. Wang, and C. Da, *Insights on foam transport from a texture-implicit local-equilibrium model with an improved parameter estimation algorithm,* Industrial & Engineering Chemistry Research **55**, 7819 (2016).

[100] L. Kapetas, S. Vincent-Bonnieu, R. Farajzadeh, A. Eftekhari, S. Mohd-Shafian, R. K. Bahrim, and W. Rossen, *Effect of permeability on foam-model parameters-an integrated approach from coreflood experiments through to foam diversion calculations,* in *IOR 2015-18th European Symposium on Improved Oil Recovery* (2015).

[101] J. Tang, M. N. Ansari, and W. R. Rossen, *Quantitative modeling of the effect of oil on foam for enhanced oil recovery,* SPE Journal **24**, 1057 (2019).

[102] J. Kim, Y. Dong, and W. R. Rossen, *Steady-state flow behavior of co2 foam,* SPE Journal **10**, 405 (2005).

[103] B. C. Sharma, W. E. Brigham, L. M. Castanier, and T. Reid, *CT imaging techniques for two-phase and three-phase in situ saturation measurements*, Ph.D. thesis, Stanford University (1997).

[104] A. A. Eftekhari and R. Farajzadeh, *Effect of foam on liquid phase mobility in porous media,* Scientific reports **7**, 43870 (2017).

[105] R. P. Chapuis and M. Aubertin, *Predicting the coefficient of permeability of soils using the kozeny-carman equation,* (2003).

[106] S. Y. Shah, H. As Syukri, K.-H. Wolf, R. M. Pilus, and W. R. Rossen, *Foam generation in flow across a sharp permeability transition: Effect of velocity and fractional flow,* SPE Journal **25**, 451 (2020).

[107] J. Gong, S. Vincent-Bonnieu, R. Z. Kamarul Bahrim, C. A. Che Mamat, R. D. Tewari, M. I. Mahamad Amir, J. Groenenboom, R. Farajzadeh, and W. R. Rossen, *Injectivity of multiple slugs in surfactant alternating gas foam eor: A ct scan study,* SPE Journal **25**, 895 (2020).

[108] H. L. Stone, *Vertical, conformance in an alternating water-miscible gas flood,* in *SPE Annual Technical Conference and Exhibition* (Society of Petroleum Engineers, 1982).

[109] M. Jenkins, *An analytical model for water/gas miscible displacements,* in *SPE enhanced oil recovery symposium* (Society of Petroleum Engineers, 1984).

[110] J. Shi and W. Rossen, *Simulation of gravity override in foam processes in porous media,* SPE Reservoir Evaluation & Engineering **1**, 148 (1998).

[111] W. Rossen and C. Van Duijn, *Gravity segregation in steady-state horizontal flow in homogeneous reservoirs,* Journal of Petroleum Science and Engineering **43**, 99 (2004).

[112] W. R. Rossen and C. Shen, *Gravity segregation in gas-injection ior,* in *EUROPEC/EAGE conference and exhibition* (Society of Petroleum Engineers, 2007).

[113] W. Rossen and G. Stolwijk, *Gravity segregation in gas ior in heterogeneous reservoirs,* in *IOR 2009-15th European Symposium on Improved Oil Recovery* (European Association of Geoscientists & Engineers, 2009) pp. cp–124.

[114] W. R. Rossen, C. Van Duijn, Q. P. Nguyen, C. Shen, and A. K. Vikingstad, *Injection strategies to overcome gravity segregation in simultaneous gas and water injection into homogeneous reservoirs,* SPE Journal **15**, 76 (2010).

[115] M. Jamshidnezhad, *Gravity segregation in gas improved oil recovery of tilted reservoirs,* in *EUROPEC/EAGE Conference and Exhibition* (Society of Petroleum Engineers, 2009).

[116] G. Yu, M. Namani, J. Kleppe, and W. Rossen, *Gravity override and vertical sweep efficiency in dipping reservoirs,* in *IOR 2017-19th European Symposium on Improved Oil Recovery*, Vol. 2017 (European Association of Geoscientists & Engineers, 2017) pp. 1–10.

[117] M. Jamshidnezhad and T. Ghazvian, *Analytical modeling for gravity segregation in gas improved oil recovery of tilted reservoirs,* Transport in porous media **86**, 695 (2011).

[118] M. Namani, J. Kleppe, L. Høier, H. Karimaie, and O. Torsæter, *Analytical model for zones distributions in non-horizontal miscible wag injection,* Energy Environ Res **2**, 159 (2012).

[119] M. Y. Khan and A. Mandal, *Analytical model for gravity segregation in wag displacement recovery of inclined stratified reservoirs,* Journal of Petroleum Science and Engineering **186**, 106722 (2020).

[120] A. T. Turta and A. K. Singhal, *Field foam applications in enhanced oil recovery projects: screening and design aspects,* Journal of Canadian Petroleum Technology **41** (2002), https://doi.org/10.2118/02-10-14.

[121] C. Shen, W. Rossen, and Q. Nguyen, *Gravity segregation in non-newtonian foam ior,* in *IOR 2007-14th European Symposium on Improved Oil Recovery* (European Association of Geoscientists & Engineers, 2007) pp. cp–24.

[122] Z. P. Alcorn, T. Føyen, L. Zhang, M. Karakas, S. L. Biswal, G. Hirasaki, and A. Graue, *Co2 foam field pilot design and initial results,* in *SPE Improved Oil Recovery Conference* (Society of Petroleum Engineers, 2020).

[123] H. L. Stone, *A simultaneous water and gas flood design with extraordinary vertical gas sweep,* in *SPE international petroleum conference in Mexico* (Society of Petroleum Engineers, 2004).

[124] I. P. O. C. IPCC, *Climate Change 2013: The physical science basis: Working group I contribution to the fifth assessment report of the Intergovernmental Panel on Climate Change* (Cambridge University Press, 2014).

[125] NASA, *Long-term warming trend continued in 2017: Nasa, noaa,* (2018).

[126] K. Pruess, J. García, T. Kovscek, C. Oldenburg, J. Rutqvist, C. Steefel, and T. Xu, *Code intercomparison builds confidence in numerical simulation models for geologic disposal of CO_2*, Energy **29**, 1431 (2004).

[127] S. Raziperchikolaee, V. Alvarado, and S. Yin, *Effect of hydraulic fracturing on long-term storage of CO_2 in stimulated saline aquifers,* Applied Energy **102**, 1091 (2013).

[128] E. Ajoma, T. Sungkachart, J. Ge, and F. Le-Hussain, *Water-saturated CO_2 injection to improve oil recovery and CO_2 storage,* Applied Energy **266**, 114853 (2020).

[129] J. Gale, *Geological storage of CO_2: What do we know, where are the gaps and what more needs to be done?* Energy **29**, 1329 (2004).

[130] S. Bachu, D. Bonijoly, J. Bradshaw, R. Burruss, S. Holloway, N. P. Christensen, and O. M. Mathiassen, *CO_2 storage capacity estimation: Methodology and gaps,* International Journal of Greenhouse Gas Control **1**, 430 (2007).

[131] D. Li, H. Zhang, Y. Li, W. Xu, and X. Jiang, *Effects of n2 and h2s binary impurities on CO_2 geological storage in stratified formation–a sensitivity study,* Applied Energy **229**, 482 (2018).

[132] Q. M. Malik and M. Islam, *CO_2 injection in the weyburn field of canada: optimization of enhanced oil recovery and greenhouse gas storage with horizontal wells,* in *SPE/DOE Improved Oil Recovery Symposium* (Society of Petroleum Engineers, 2000).

[133] K. Jessen, A. R. Kovscek, and F. M. Orr Jr, *Increasing CO_2 storage in oil recovery,* Energy Conversion and Management **46**, 293 (2005).

[134] M. A. Hesse, F. M. Orr, and H. Tchelepi, *Gravity currents with residual trapping,* Journal of Fluid Mechanics **611**, 35 (2008).

[135] M. A. Celia and J. M. Nordbotten, *Practical modeling approaches for geological storage of carbon dioxide,* Groundwater **47**, 627 (2009).

[136] B. Caudle and A. Dyes, *Improving miscible displacement by gas-water injection,* Transactions of the AIME **213**, 281 (1958).

[137] P. Bedrikovetsky, *Wag displacements of oil-condensates accounting for hydrocarbon ganglia,* Transport in Porous Media **52**, 229 (2003).

[138] R. Qi, T. C. LaForce, and M. J. Blunt, *Design of carbon dioxide storage in aquifers,* International Journal of Greenhouse Gas Control **3**, 195 (2009).

[139] R. A. Kil, Q. P. Nguyen, and W. R. Rossen, *Determining trapped gas in foam from computed-tomography images,* SPE Journal **16**, 24 (2011).

[140] M. T. Elenius, J. M. Nordbotten, and H. Kalisch, *Effects of a capillary transition zone on the stability of a diffusive boundary layer,* The IMA Journal of Applied Mathematics **77**, 771 (2012).

[141] M. T. Elenius, J. M. Nordbotten, and H. Kalisch, *Convective mixing influenced by the capillary transition zone,* Computational Geosciences **18**, 417 (2014).

[142] M. Elenius, D. Voskov, and H. Tchelepi, *Interactions between gravity currents and convective dissolution,* Advances in Water Resources **83**, 77 (2015).

[143] J. P. Ennis-King, L. Paterson, *et al., Role of convective mixing in the long-term storage of carbon dioxide in deep saline formations,* SPE Journal **10**, 349 (2005).

[144] K. Pruess and K. Zhang, *Numerical modeling studies of the dissolution-diffusion-convection processduring CO_2 storage in saline aquifers*, Tech. Rep. (Lawrence Berkeley National Lab.(LBNL), Berkeley, CA (United States), 2008).

[145] G. S. Pau, J. B. Bell, K. Pruess, A. S. Almgren, M. J. Lijewski, and K. Zhang, *High-resolution simulation and characterization of density-driven flow in CO_2 storage in saline aquifers,* Advances in Water Resources **33**, 443 (2010).

[146] J. Ennis-King, I. Preston, and L. Paterson, *Onset of convection in anisotropic porous media subject to a rapid change in boundary conditions,* Physics of Fluids **17**, 084107 (2005).

[147] X. Xu, S. Chen, and D. Zhang, *Convective stability analysis of the long-term storage of carbon dioxide in deep saline aquifers,* Advances in water resources **29**, 397 (2006).

[148] A. Riaz and H. Tchelepi, *Stability of two-phase vertical flow in homogeneous porous media,* Physics of Fluids **19**, 072103 (2007).

[149] H. E. Meybodi and H. Hassanzadeh, *Stability analysis of two-phase buoyancy-driven flow in the presence of a capillary transition zone,* Physical Review E **87**, 033009 (2013).

[150] H. Emami-Meybodi and H. Hassanzadeh, *Two-phase convective mixing under a buoyant plume of CO_2 in deep saline aquifers,* Advances in water resources **76**, 55 (2015).

[151] A. C. Slim, *Solutal-convection regimes in a two-dimensional porous medium,* Journal of Fluid Mechanics **741**, 461 (2014).

[152] G.-Q. Tang and A. Kovscek, *Trapped gas fraction during steady-state foam flow,* Transport in Porous Media **65**, 287 (2006).

[153] S. Jones, N. Getrouw, and S. Vincent-Bonnieu, *Foam flow in a model porous medium: Ii. the effect of trapped gas,* Soft Matter **14**, 3497 (2018).

[154] H. Li and J. Yan, *Impacts of equations of state (eos) and impurities on the volume calculation of CO_2 mixtures in the applications of CO_2 capture and storage (ccs) processes,* Applied Energy **86**, 2760 (2009).

[155] J. P. Spivey, W. McCain Jr, and R. North, *Estimating density, formation volume factor, compressibility, methane solubility, and viscosity for oilfield brines at temperatures from 0 to 275 c, pressures to 200 mpa, and salinities to 5.7 mole/kg,* Journal of Canadian Petroleum Technology **43** (2004), https://doi.org/10.2118/04-07-05.

[156] J. E. Garcia, *Density of aqueous solutions of CO_2*, Tech. Rep. (Lawrence Berkeley National Lab.(LBNL), Berkeley, CA (United States), 2001).

[157] S. Mao and Z. Duan, *The viscosity of aqueous alkali-chloride solutions up to 623 k, 1,000 bar, and high ionic strength,* International Journal of Thermophysics **30**, 1510 (2009).

[158] A. W. Islam and E. S. Carlson, *Viscosity models and effects of dissolved CO_2,* Energy & Fuels **26**, 5330 (2012).

[159] A. L. Lee, M. H. Gonzalez, and B. E. Eakin, *The viscosity of natural gases,* Journal of Petroleum Technology **18**, 997 (1966).

[160] M. Namdar-Zanganeh, T. La Force, S. Kam, T. van der Heijden, and W. Rossen, *Fractional-flow theory of foam displacements with oil,* in *ECMOR XI-11th European Conference on the Mathematics of Oil Recovery* (2008).

[161] A. Dharma, *Simulation studies of foam for enhanced oil recovery,* (2013), http://resolver.tudelft.nl/uuid:8276c89d-97ce-4d6f-a149-cdb04b71078c.

[162] J. Van der Meer, J. Kraaijevanger, M. Möller, and J. Jansen, *Temporal oscillations in the simulation of foam enhanced oil recovery,* in *ECMOR XV-15th European Conference on the Mathematics of Oil Recovery* (2016).

[163] M. T. Van Genuchten, *A closed-form equation for predicting the hydraulic conductivity of unsaturated soils.* Soil science society of America journal **44**, 892 (1980).

[164] R. Brooks and T. Corey, *Hydraulic properties of porous media,* Hydrology Papers, Colorado State University **24**, 37 (1964).

[165] A. Moradi-Araghi, E. Johnston, D. Zornes, and K. Harpole, *Laboratory evaluation of surfactants for co2-foam applications at the south cowden unit,* in *International Symposium on Oilfield Chemistry* (Society of Petroleum Engineers, 1997).

[166] O. Redlich and J. N. Kwong, *On the thermodynamics of solutions. v. an equation of state. fugacities of gaseous solutions.* Chemical reviews **44**, 233 (1949).

A

APPENDIX

A.1. MULTIPHASE FLOW WITH THE EFFECT OF CAPILLARITY

Case 1 in Scenario 2 in Chapter 4 presents a big challenge to our simulator: the simulator shows oscillations (Fig. A.1). The oscillations cannot be eliminated by using extremely small timestep and grid size [92, 98, 160, 161]. The reason for the failure of the numerical simulation is that the constant-state point is very close to the critical oil saturation (fmoil), and a small variation of saturation may cause the solution to jump across the foam/no-foam boundary, where k_{rg} changes dramatically. Due to the discretization scheme (upwinding), we see this problem in Case 1 of Scenario 2 (Fig. A.1(a)). In principle, it should be possible to reduce the amplitude of these oscillations by sufficiently reducing the timestep and grid size [92], adding a capillary diffusion coefficient [98, 101], implementing global/local chops to limit the composition changes during the Newton iterations [35], and changing discretization schemes [162]. In our work, we do not test all possibilities to avoid these oscillations. Instead, we eliminate the oscillations by adding a small capillary diffusion term (Fig. A.1(c)). The details about simulating the effects of capillarity using the OBL approach are shown in Chapter 2.

Capillary pressure is a function of saturation, often expressed as $p_c(s_w)$:

$$p_c = p_n - p_w, \tag{A.1}$$

where n and w indicate the non-wetting phase and wetting phase, respectively. The phase-potential-upwinding (PPU) strategy, where phase mobilities are selected based on the phase potential difference, is applied to compute the numerical flux in DARTS. The phase potential difference p in the absence of gravity between block i and j can be written as

$$\Phi_{p,ij} = p_j - p_{c,j} - (p_i - p_{c,i}), \tag{A.2}$$

Capillary pressure is treated as one stand-alone operator which depends only on the physical state. For a n_p-phase system, only n_p - 1 capillary pressures are needed for the calculation of phase pressure. To keep the whole system coordinated, the capillary

A

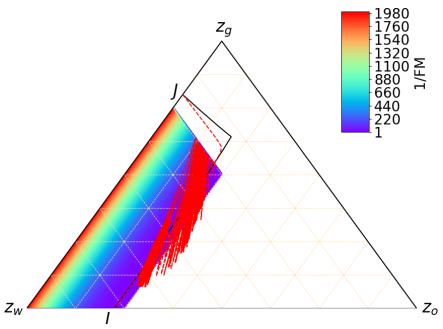

(a) Composition path

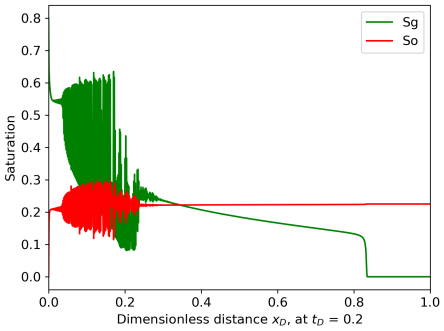

(b) Gas-saturation and oil-saturation profiles

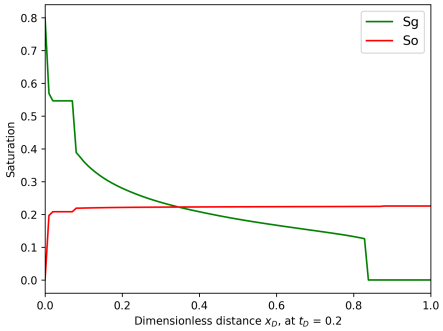

(c) Gas-saturation and oil-saturation profiles with capillary diffusion

Figure A.1: Illustrations of numerical instability for Case 1 in Scenario 2 in the simulation with 1000 gridblocks. (a) Composition path from injection condition (J) to initial condition (I). The black solid line is the analytical solution, and the red dashed line is the OBL solution. (b) Gas-saturation and oil-saturation profiles as a function of dimensionless position x_D at time $t_D = 0.20$ PVI. (c) Gas-saturation and oil-saturation profiles with capillary diffusion introduced to eliminate the oscillations.

pressure operator of the reference phase is defined as 0. Therefore, n_p capillary-pressure operators are introduced in this system. Typically, the capillary-pressure curve is either S-shaped (e.g., van Genuchten model) [163] or convex (e.g., Brooks-Corey model) [164]. Here the Brooks-Corey-type model is applied for calculation of capillary pressure operator:

$$p_c(\omega) = p_d \left(\frac{S_w(\omega) - S_{wc}}{1 - S_{wc} - S_{or}} \right)^{-1/\lambda}, \tag{A.3}$$

where p_d is the capillary entry pressure. The corresponding capillary pressure curves are shown in Fig. A.2.

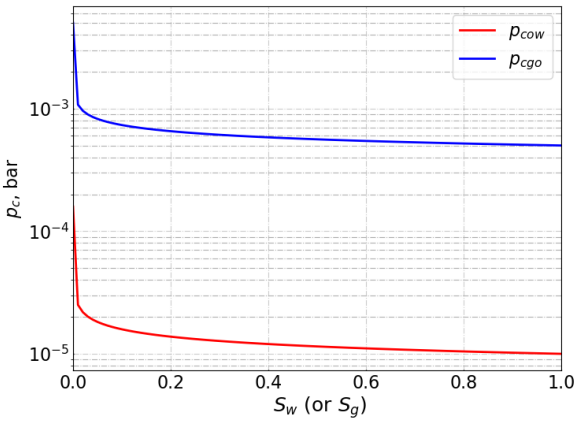

Figure A.2: Capillary-pressure curves used in this study to suppress oscillations. p_{cow} is a function of water saturation (S_w), while p_{cgo} is a function of water saturation (S_g).

A.2. MODEL REGRESSION TO THE DATA BY GRADIENT-OPTIMIZATION TECHNIQUE

The relative-permeability model implemented in Chapter 4 is the Brooks-Corey model [164]. The relative permeability of each phase only depends on its own saturation:

$$k_{r,i} = k_{re,i}\left(\frac{S_i - S_{ir}}{1 - S_{wc} - S_{or} - S_{gr}}\right)^{n_i}, \tag{A.4}$$

where subscript $i \in \{g, o, w\}$ denotes phases present in the simulation. $k_{r,i}$ and $k_{re,i}$ are the phase relative permeabilities at the a certain saturation and at the end point, respectively. S_{wc}, S_{or} and S_{gr} are residual phase saturations.

The modifiers implanted are Brooks-Corey parameters, and there are 9 parameters which need to be optimized during the simulation. The objective function tested in the simulation is shown as:

$$J(x)_{min} = \sqrt{\sum_{k=1}^{n_p}\sum_{i=1}^{N}(y_k^i(x) - y^{obs})^2}, \tag{A.5}$$

where $y_k^i(x)$ and y^{obs} are phases saturation obtained from simulation and experiment. The final optimal parameters are shown in Table A.1.

Table A.1: Optimal parameter values for Brooks-Corey relative-permeability model

Parameters	Value	Parameters	Value	Parameters	Value
k_{rwe}	0.247	S_{wc}	0.197	n_w	3.86
k_{roe}	0.584	S_{or}	0.103	n_o	2.54
k_{rge}	0.830	S_{gr}	0.013	n_g	1.62

A

A.3. FOAM PARAMETER-FITTING

In Chapter 5, we represent the effect of heterogeneity on foam using foam parameters by fitting the foam-quality scans from Moradi-Araghi *et al.* [165]. They tested the effect of rock permeability on CO_2-foam strength. The permeability of the reservoir formations they tested ranges from 32.8 to 551.5 mD. In order to extract foam model parameters from their experimental data, we assume that the permeability does not change the rock wetting behaviour: Corey exponents and residual saturations in water-gas relative-permeabilities are the same in the different formations. We neglect shear-thinning in the low-quality regime. Based on these assumptions, we fit the foam parameters for the STARS model.

The relative-permeability data and foam parameters are listed in Table A.2. Fig. A.3 presents the gas apparent viscosity as a function of foam quality for rocks with different permeabilities. As is shown, two regimes can be observed for all permeabilities: the apparent viscosity of foam increases and reaches a maximum value with increasing foam quality (low-quality regime) and thereafter decreases with further increase in foam quality (high-quality regime). Moreover, the foam apparent viscosity increases with increasing permeability, i.e., foam appears to be stronger in a rock with higher permeability.

Table A.2: Corey relative-permeability parameters and foam parameters fit to coreflood data for formations with different permeability.

	Permeability, mD	k^0_{rw}	n_w	k^0_{rg}	n_g	S_{wc}	S_{gr}	$fmmob$	$epdry$	$fmdry$
K_1	32.8	0.2	2.0	1.0	1.8	0.1	0.05	1.02×10^3	2.50×10^4	0.185
K_2	56.8							1.58×10^3	9.40×10^3	0.171
K_3	169.8							3.14×10^3	6.96×10^3	0.155
K_4	551.5							9.74×10^3	4.76×10^3	0.136

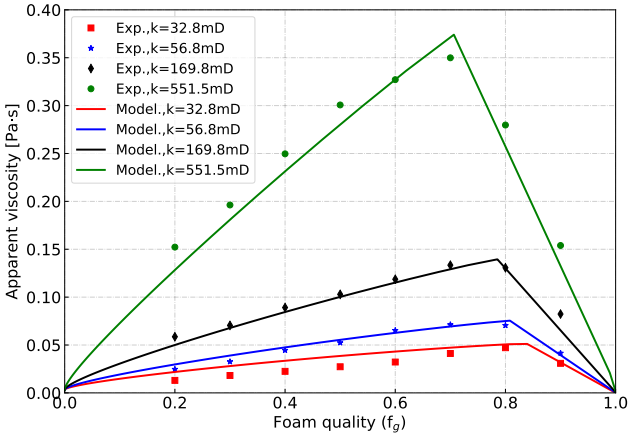

Figure A.3: Fit of the model to experimental data.

The following values are assumed for physical properties in Eq. 5.1 or Eq. 5.2: μ_w = 0.65 mPa·s and μ_g = 0.05 mPa·s; ρ_w = 1000 kg/m^3, and ρ_g = 166 kg/m^3 which correspond to the values computed by Redlich-Kwong's equation of state (EOS) [166].

A.4. RELATION BETWEEN INJECTION PRESSURE AND SEGREGATION LENGTH

Rossen *et al.* [114] explicitly showed the relation between injection pressure and gravity segregation in cylindrical flow and found that the only way to control gravity segregation with steady-state injection into a given reservoir is to increase injection-well pressure. In Chapter 5, we extend this relation to a rectangular coordinate system by assuming that the bottom hole pressure of the injector is equal to the pressure of the reservoir block with which the well is connected with. Fig. A.4 illustrates two shapes of mixed, override, and underride zones. Fig. A.4(a) shows that the amount of water and gas left in the mixed zone is proportional to ratio between the position x and the segregation point L_g, suggesting that the height of the mixed zone depends on the total flow rate of the mixed zone. While in Fig. A.4(b), all gas and water are remained in the mixed zone until they separate out of the mixed zone, i.e., the height of the mixed zone decreases little with increasing distance from the injection well until shortly before the segregation point. These two cases represent two limits of injection pressure in water and gas co-injection process.

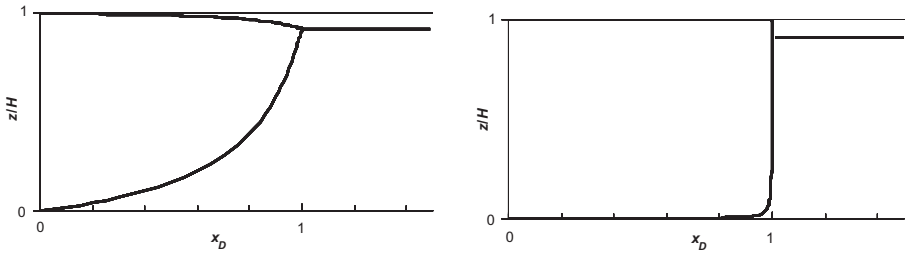

Figure A.4: Two asymptotic cases of mixed, override, and underride zones from [114]. (a) The height of the mixed zone shrinks nearly proportionately to distance from the injection well. (b) The height of the mixed zone is almost uniform with increasing x until the segregation point is approached.

In the first case, the total flow rate in the mixed zone decreases linearly with x/L_g, which suggests the total horizontal superficial velocity U_t in the mixed zone in the linear flow is given by

$$U_t = \frac{Q}{A}(1 - \frac{x}{L_g}) = -K_h \lambda_{rt}^m \frac{dP}{dL} \tag{A.6}$$

where x is position, K_h is the horizontal permeability. By integrating from the well to the point of segregation, the injection pressure is given by

$$p(inj) - p(L_g) = \frac{QL_g}{2AK_h\lambda_{rt}^m} \tag{A.7}$$

where $p(inj)$ and $p(L_g)$ are the injection pressure and the pressure at segregation point, respectively. Then rearranging Eq. 5.1 into an expression for Q, and plugging in for Q in

A

Eq. A.7, gives

$$p(inj) - p(L_g) = \frac{L_g^2 K_z (\rho_w - \rho_g) g W}{2AK_h} \tag{A.8}$$

In the second case, where the total flow rate is uniform in the mixed zone, Eqs. A.6, A.7 and A.8 become

$$U_t = \frac{Q}{A} = -K_h \lambda_{rt}^m \frac{dP}{dL} \tag{A.9}$$

$$p(inj) - p(L_g) = \frac{QL_g}{AK_h \lambda_{rt}^m} \tag{A.10}$$

and

$$p(inj) - p(L_g) = \frac{L_g^2 K_z (\rho_w - \rho_g) g W}{AK_h} \tag{A.11}$$

Note that neither Q nor λ_{rt}^m is involved into Eqs. A.8 or A.11.

CURRICULUM VITÆ

Xiaocong LYU

20-11-1989 Born in Shandong, China.

EDUCATION

2010–2014 Bachelor Degree, Petroleum Engineering
China University of Petroleum (East China)

2014–2017 Master Degree, Petroleum Engineering
China University of Petroleum (Beijing)

2017–2021 Doctor of Philosophy, Petroleum Engineering
Delft University of Technology
Thesis: Simulation of Foam in Enhanced Oil Recovery (EOR) and Carbon Capture and Storage (CCS) Applications
Promotors: Dr. D.V. Voskov
Prof. dr. W.R. Rossen

LIST OF PUBLICATIONS

JOURNAL ARTICLES

5. **X. Lyu, D.V. Voskov, W.R. Rossen**, *Mitigation of Gravity Segregation by Foam during Supercritical CO_2 Injection in Heterogeneous Reservoirs*, in preparation.

4. **X. Lyu, D.V. Voskov, J. Tang, W.R. Rossen**, *Simulation of Foam Enhanced-Oil-Recovery Processes Using Operator-Based Linearization Approach*, SPE Journal (2021): **1-18**.

3. **X. Lyu, M. Khait, D.V. Voskov**, *Operator-Based Linearization Approach for Modeling of Multiphase Flow with Buoyancy and Capillarity*, SPE Journal (2021): **1-18**.

2. **X. Lyu, D.V. Voskov, W.R. Rossen**, *Numerical investigations of foam-assisted CO_2 storage in saline aquifers*, International Journal of Greenhouse Gas Control (2021): **103314**.

1. **X. Lyu, H. Liu, Z. Pang, Z. Sun**, *Visualized study of thermochemistry assisted steam flooding to improve oil recovery in heavy oil reservoir with glass micromodels*, Fuel (2018): **118-126**.

CONFERENCE PROCEEDINGS AND TALKS

5. **X. Lyu, D.V. Voskov, W.R. Rossen**, *Gravity Segregation with CO_2 Foam in Heterogeneous Reservoirs*, presented at 21^{st} European Symposium on Improved Oil Recovery (online).

4. **X. Lyu, D.V. Voskov, W.R. Rossen**, *Gravity Segregation in Foam Mobility Control in Heterogeneous Reservoirs*, presented at 12^{th} International Conference on Porous Media & Annual Meeting (online).

3. **X. Lyu, D.V. Voskov, W.R. Rossen**, *Efficiency of CO_2 storage in saline aquifers using foam co-injection*, presented at GeoUtrecht 2020, Utrecht, The Netherlands (online).

2. **X. Lyu, D.V. Voskov, W.R. Rossen**, *Simulation of Foam-Assisted CO_2 Storage in Saline Aquifers*, presented at 17^{th} European Conference on the Mathematics of Oil Recovery (online).

1. **X. Lyu, M. Khait, D.V. Voskov**, *Operator-based linearization method for modelling of multiphase flow with buoyancy and capillarity*, presented at 11^{th} International Conference on Porous Media & Annual Meeting, Valencia, Spain.

ACKNOWLEDGEMENTS

Ph.D. life is a long journey with numerous unforgettable memories. This journey would never be possible and accomplished without the support and help from many individuals. I would like to express my sincere gratitude for their involvement during my challenging Ph.D. study.

First and foremost, I would like to express my deepest gratitude to my promotor and daily supervisor, Dr. **Denis Voskov**. It is my great honor to have this opportunity to work with you. I feel proud to be your second PhD student at Delft University of Technology. The experience from experiment to simulation with programming is full of challenges but amazing. With your guidance, I jumped into a new fantasy world. Thank you for your endless patience and help during these four years even though I always made mistakes and brought troubles to you in the beginning. Outside of the campus, you are one best friend who always shares your valuable experience in absolutely everything you know, including academic topics. Thank you and Kate for warmly organizing the wonderful group parties in your house. The most impressive memory was to share your Scotch whiskey and introduce the interesting story to us. I really enjoyed every moment of working with you. Thank you, Denis.

Next, I would like thank my second promotor Prof. **William R. Rossen** for giving me an opportunity to join the foam group. It is an amazing journey working with you because you are always enthusiastic about the problems and ideas we discussed in our weekly meetings. You are full of knowledge in physics and numerical simulations and can always share your inspiring and valuable suggestions. Thank you for your help with coaching me in academic writing. Your rigorous attitude towards academic life and research is one of the most important spirits which helped me grow professionally over the past four years. Thank you for your support and patience.

I would like to thank Prof. **Pacelli Zitha**, Prof. **David Bruhn**, Dr. **Sarah Eileen Gasda**, Dr. **Yves Méheust** and Dr. **Rouhi Farajzadeh** for being my committee members and sharing your valuable comments on my dissertation.

Prof. **Hans Bruining**, I am really impressed by your energy and passion for research. Our discussion in your course 'Introduction of transport in porous media' was quite useful for my research. Thanks for sharing your interesting stories in our Faculty Christmas Evening. Dr. **Janice Rossen**, you are so kind to care about my progress in every group dinner and parties. Thank you for inviting me to attend your piano show and sharing your CDs with me. I would also thank you and **Bill** for your blessing to my wife and me. **Mark**, thank you for your endless help and essential contributions to my work. I would not have been able to finish my project without you. You are always patient to answer my technical or non-technical questions when I was lost in C++ programming. These limited words cannot convey my gratitude for your support. I also would like to thank Dr. **Sian Jones** for your guidance in steam foam simulation. Sian, you are always patient to share your knowledge in experiments and give me advice on how to carry out the cor-

responding physical simulations. More importantly, thank you for sharing the cakes you made, and to be honest, these cakes are one of my favorite cakes.

Many thanks to other colleagues in DARTS group, and thank you all for creating this great working atmosphere and providing valuable suggestions and assistance in my work. **Yang**, for being a helpful friend who always shares your experience in geothermal simulations. Thank you for your help with answering all my questions related to DARTS. **Stephan**, I really appreciate your selfless discussions about our discretizer and Gmesh. **Kiarash**, for being a nice friend who invites me to be involved in many parties. Thank you, **Xiaoming**, for your time to explain some questions about adjoint method. **Aleks**, you are an expert in mathematics and I learned a lot from you. I would also like to thank you all for express your kind blessing in my wedding ceremony. That was a wonderful gift to me.

To all foam group members, your involvement in my PhD study made this journey more pleasant. **Jiakun**, my elder brother, thank you for helping me become involved in the foam group quickly and sharing your experience when I asked for help. Thanks for your gifts when you left the Netherlands. **Jinyu**, I really appreciate your support in my research. Thank you for the long discussions about academic or personal problems. You were always generous when we went outside for dinners, and I hope to be your brother forever. The presence of you and your beloved **Xuhong** made my wedding ceremony successful. Thank you, my Bro! **Swej**, one of my best friends in Delft, we had too many unforgettable memories, basketball games, parties with beers, and 'sumptuous banquets' with Chinese/Indian food. You always encouraged me when I felt stuck in my research and helped me to be a 'native' PhD. I am thankful for your contribution to my enjoyable life at TUD. **Guanqun**, my new desk mate, for giving me so many useful suggestions on my research and for your delicious food you prepared for our parties every time. **Kai**, for organizing the foam group meetings and for sharing your working experience.

I would also like to thank several other colleagues in my office for their contributions. **Martijn**, **Siamak**, and **Mohsen** for creating a fun atmosphere in the office. **Nikita**, for organizing weekly basketball games in TUD sports center. **Matei**, for your invitation to your birthday party and for organizing one of the greatest dinner during Chinese New Year evening. I really liked your gift, a delicate coffee cup from Romania. **Shahrzad**, for your invitation to bike trips, big parties at your place and gifts from Iran. The cake you made is delicious as well. **Longlong**, for your constructive talks both in academic questions and in future plans. I also want to express my gratitude to some Chinese friends (please don't mind if I miss your name): **Mingyan (Max)**, **Xiangcou**, **Xiaodong**, **Rui**, **Fanxiang**, **Wenqiang**, **Biyue**, **Xinyue**, **Zixia**, **Meiqi**, **Lihua**, **Wenting**, **Yan**, **Shan**, **Kailun**, who made the journey a truly memorable experience.

Marlijn, **Lydia**, **Ralf**, **Margot**, **Marja**, **Nancy** and the rest of the **GSE support staff**, many thanks for your continuous help and prompt response with my requests during the past four years. Thank you all for creating this productive environment for us to work in.

Fengzhu, my dearest beloved. Thanks for your selfless support. The distance between China and Netherlands is quite long, but our hearts are always together. You always encouraged me to move forward whenever I had personal or academic problems. We had a hard time in the past 3 years during my PhD study, but we managed to over-

come all the challenges. I am so happy and lucky to marry you and I hope to enjoy our lovely and warm story in the following journey.

Finally, I would like to thank my elder **brother** and **sister** for their kind help during my PhD study. They always cared about me and gave me financial support. Thanks to my **parents (in law)** for understanding and trusting me. I will cherish every moment with your daughter, now my wife. Last but not least, my deepest gratitude to my **parents**. Your unconditional love is the basis of my wonderful journey in Delft. No words can express my appreciation. Thank you and love you, Mom and Dad!

Xiaocong Lyu
Delft, June 2021